YSOVAR: Mid-Infrared Variability in NGC 1333

L. M. Rebull[1,2], J. R. Stauffer[2], A. M. Cody[2,3], H. M. Günther[4,5] L. A. Hillenbrand[6] , K. Poppenhaeger[7,4]
S. J. Wolk[4], J. Hora[4], J. Hernandez[8], A. Bayo[9,10], K. Covey[11,12], J. Forbrich[13,4], R. Gutermuth[14],
M. Morales-Calderón[15], P. Plavchan[16], I. Song[17], H. Bouy[15], S. Terebey[18] J. C. Cuillandre[19], L. E. Allen[20]

ABSTRACT

As part of the Young Stellar Object VARiability (YSOVAR) program, we monitored NGC 1333 for $\sim$35 days at 3.6 and 4.5 μm using the Spitzer Space Telescope. We report here on the mid-infrared variability of the point sources in the $\sim 10' \times \sim 20'$ area centered on 03:29:06, +31:19:30 (J2000). Out of 701 light curves in either channel, we find 78 variables over the YSOVAR campaign. About half of the members are variable. The variable fraction for the most

[1]Infrared Science Archive (IRSA), Infrared Processing and Analysis Center (IPAC), 1200 E. California Blvd., California Institute of Technology, Pasadena, CA 91125; rebull@ipac.caltech.edu

[2]Spitzer Science Center (SSC), 1200 E. California Blvd., California Institute of Technology, Pasadena, CA 91125

[3]NASA Ames Research Center, Moffett Field, CA 94035

[4]Harvard-Smithsonian Center for Astrophysics, 60 Garden St., Cambridge, 02138 MA, USA

[5]Massachusetts Institute of Technology, Kavli Institute for Astrophysics and Space Research, 77 Massachusetts Avenue, NE83-557 Cambridge, MA 02139, USA

[6]Department of Astronomy, California Institute of Technology, Pasadena, CA 91125

[7]NASA Sagan Fellow

[8]Centro de Investigaciones de Astronomía, Apdo. Postal 264, Mérida 5101-A, Venezuela

[9]Max Planck Institut für Astronomie, Königstuhl 17, 69117, Heidelberg, Germany

[10]Departamento de Física y Astronomía, Facultad de Ciencias, Universidad de Valparaíso, Av. Gran Bretaña 1111, 5030 Casilla, Valparaíso, Chile

[11]Lowell Observatory, 1400 West Mars Hill Road, Flagstaff, AZ 86001 USA

[12]Department of Physics and Astronomy, Western Washington University, 516 High Street, Bellingham WA 98225 USA

[13]University of Vienna, Department of Astrophysics, Türkenschanzstr. 17, 1180 Vienna, Austria

[14]Dept. of Astronomy, University of Massachusetts, Amherst, MA 01003 USA

[15]Depto. Astrofísica, Centro de Astrobiología (INTA-CSIC), ESAC campus, P.O. Box 78, E-28691 Villanueva de la Cañada, Spain

[16]NASA Exoplanet Science Institute (NExScI), Infrared Processing and Analysis Center (IPAC), 1200 E. California Blvd., California Institute of Technology, Pasadena, CA 91125 USA, and Missouri State University, 901 S National Ave, Springfield, MO 65897 USA

[17]Physics and Astronomy Department, University of Georgia, Athens, GA 30602-2451 USA

[18]Department of Physics and Astronomy, 5151 State University Drive, California State University at Los Angeles, Los Angeles, CA 90032 USA

[19]Canada-France-Hawaii Telescope Corporation, 65-1238 Mamalahoa Highway, Kamuela, HI96743, USA

[20]NOAO, 950 N. Cherry Ave., Tucson, AZ USA

embedded SEDs (Class I, flat) is higher than that for less embedded SEDs (Class II), which is in turn higher than the star-like SEDs (Class III). A few objects have amplitudes (10-90th percentile brightness) in [3.6] or [4.5]>0.2 mag; a more typical amplitude is 0.1-0.15 mag. The largest color change is >0.2 mag. There are 24 periodic objects, with 40% of them being flat SED class. This may mean that the periodic signal is primarily from the disk, not the photosphere, in those cases. We find 9 variables likely to be 'dippers', where texture in the disk occults the central star, and 11 likely to be 'bursters', where accretion instabilities create brightness bursts. There are 39 objects that have significant trends in [3.6]−[4.5] color over the campaign, about evenly divided between redder-when-fainter (consistent with extinction variations) and bluer-when-fainter. About a third of the 17 Class 0 and/or jet-driving sources from the literature are variable over the YSOVAR campaign, and a larger fraction (∼half) are variable between the YSOVAR campaign and the cryogenic-era Spitzer observations (6-7 years), perhaps because it takes time for the envelope to respond to changes in the central source. The NGC 1333 brown dwarfs do not stand out from the stellar light curves in any way except there is a much larger fraction of periodic objects (∼60% of variable brown dwarfs are periodic, compared to ∼30% of the variables overall).

Subject headings: circumstellar matter – stars: pre-main sequence – stars:protostars – stars: variables: general

1. Introduction

Located on the western edge of the Perseus molecular cloud, NGC 1333 is only ∼235 pc (Hirota et al. 2008, 2011) away from us. Its stars are thought to have an average age of 1-2 Myr (e.g., Bally et al. 2008), but there are also several Class 0 objects, which are objects in the earliest stages of star formation (see, e.g., Sadavoy et al. 2014 or Sandell & Knee 2001). The average extinction towards NGC 1333 could be as high as A_V∼6-7 mag (Ridge et al. 2006), with condensations of higher extinction. Few of the cluster members are easily visible in optical bands.

NGC 1333 was first mapped in the infrared (IR) in 1976 by Strom, Vrba, & Strom, who found 25 candidate young members. The region is host to numerous Herbig-Haro (HH) objects (see, e.g., Strom et al. 1974); in fact, protostellar outflows may be important in the evolution of this cluster (see, e.g., Walawender et al. 2008). The Spitzer Space Telescope (Werner et al. 2004) 4.5 μm image of this region is riddled with outflows from young stars (e.g., Plunkett et al. 2013).

Because NGC 1333 is very young and relatively nearby, and because the extinction towards this region is high enough that optical monitoring of cluster members is very difficult, we selected NGC 1333 for inclusion in the YSOVAR project. YSOVAR (Young Stellar Object VARiability) is the name of a coordinated effort to probe the mid-IR variability of young stars. This project monitored a dozen star-forming regions with the Spitzer Infrared Array Camera (IRAC; Fazio et al. 2004) in the post-cryogen era, at 3.6 and 4.5 μm. At these wavelengths, we can penetrate high extinction, and detect both photospheres and dust. Since Spitzer is space-based, there is no day-night aliasing, and monitoring campaigns can be conducted over weeks to months. Rebull et al. (2014; hereafter R14) provided an overall introduction to the YSOVAR project, including the project's goals and data reduction. One of the project's primary goals is to understand the mid-IR variability characteristics of the most embedded young stars. IR variability in young stars can contain within it signatures of a variety of processes including accretion, structure in the disk rotating into and out of view, disk scale height structure or changes, and geometric effects of companions (or protoplanets). NGC

1333 has many very embedded young stars, making it an ideal laboratory for studying the IR variability of such objects.

Walawender et al. (2008) provide a recent review of star formation in NGC 1333. Rebull (2015; hereafter R15) collects more than 25 studies and catalogs into a point source catalog of objects in the direction of NGC 1333; this catalog forms the basis on which we proceed in this paper. There are a few papers specifically reporting on variability of specific objects in NGC 1333, which we now summarize.

SVS 13, sometimes called SSV 13[1], is one of the objects discovered by Strom et al. (1976); it is very bright in the IR. Liseau, Lorenzetti, & Molinari (1992) reported that SVS 13 brightened by about a magnitude at K sometime between 1989 January and 1990 February. They postulated that the variations originated from thermal instabilities in the disk caused by variable accretion. Aspin & Sandell (1994) monitored this object over three years and found additional significant variability in the near-IR. Harvey et al. (1998) observed this object in the far-IR with the Kuiper Airborne Observatory, finding that the object brightened by a factor of 1.5-2 between the 1980s and the early 1990s, and concluding that the changes were a result of a true change in the YSO's luminosity, as opposed to changes in the foreground and/or the YSO's intrinsic extinction. (See also Hodapp 2015 and references therein.) Although this famous object is in the region we monitored as part of YSOVAR, it is very bright. It is certainly saturated in our 4.5 μm data, and just above saturation in 3.6 μm. Because this source is of particular interest, we manually extracted photometry for it, assuming it has not quite saturated. Its light curve was not included in the rest of the analysis here, but it appears in the Appendix, and it has faded by $\sim$0.15 mag in [3.6] from 2004 to 2011 (cryo-to-YSOVAR), which appears consistent with the K-band trend in Hodapp (2015).

Herbst et al. (2006) monitored this region in the optical, but report on variations from only a single object, HBC 338. They find evidence for differential rotation in this star, based on the large changes in the measured period. Unfortunately, this object is well away from the region we monitored as part of YSOVAR.

More recently, Forbrich et al. (2011) monitored this region simultaneously in X-rays and in radio. Very few YSOs were detected in both bands, and the authors did not find a close correlation between X-rays and radio luminosities, which was surprising because such a correlation is found in older active stars.

Scholz (2012) placed constraints on the frequency of large variations in the near-IR for a variety of young clusters, including NGC 1333, on timescales up to $\sim$2000 d. Of the clusters studied, the largest amplitudes of near-IR variability were found in NGC 1333, and are attributed to this cluster's youth. Scholz identifies three objects (LAL 166, LAL 189, LAL 296) as NIR variables, all of which are in our monitored fields (SSTYSV J032858.41+312217.6, J032903.13+312238.1, and J032920.04+312407.6, respectively). All are independently identified by us as variable, but not with particularly large amplitudes at 3.6 and 4.5 μm, and only one source is recovered as variable over a 6-7 year timescale.

There is also literature specifically on the variability found in the jets and clumps in NGC 1333 (see, e.g., Choi et al. 2006, Khanzadyan et al. 2003, and references therein). Changes in the outflows seen in Spitzer data are beyond the scope of this paper; Raga et al. (2013) report on proper motions of the outflows in this region using the YSOVAR data. We will discuss in this paper the mid-IR variability properties of the sources thought to be driving jets (see R15 for details on how the jet-drivers were identified).

We report here on the mid-IR variability identified in NGC 1333 during the YSOVAR (R14) campaign. Section 2 covers the observations and data reduction, and Section 3 the archival data sets included in our

---

[1]SVS 13 is known by a wide variety of synonyms, including V512 Per; in R15 it is R15-NGC1333 J032903.75+311603.9.

analysis. Section 4 defines members, variables, and other terms, and Section 5 calculates mid-IR variability fractions for various subsets of the data. Section 6 examines the amplitudes of brightness and color changes, and Section 7 analyzes the distributions of timescales in NGC 1333, including the periodic objects. Section 8 describes dippers and bursters, objects in our data that have light curve structure similar to objects identified in Spitzer monitoring of NGC 2264 (e.g., Cody et al. 2014) and Orion (e.g., Morales-Calderón et al. 2011). Section 9 identifies objects that have significant trends in the color-magnitude diagrams over the YSOVAR campaign. Finally, Section 10 calls out some special sources in NGC 1333, and Section 11 summarizes the paper.

2. Observations and Data Reduction

All YSOVAR Spitzer light curve tabular data are available via the YSOVAR data delivery to the Infrared Science Archive (IRSA). Plots of all the light curves are provided as part of that delivery; only certain light curves are shown in the present paper.

2.1. YSOVAR Spitzer Data

The observation design, operational considerations, cadence, and data reduction procedure for YSOVAR Spitzer monitoring data are discussed in detail in R14. We summarize here briefly the most salient points, but refer the reader to R14 for more details.

Figure 1 shows the sky coverage of the YSOVAR monitoring observations of NGC 1333. The observations were 2×2 IRAC FOVs in a mapping mode Astronomical Observation Request (AOR), with a 5-point small Gaussian dither pattern of 12-s high-dynamic-range (HDR) frames at each map position, resulting in a median depth of 54 s per epoch. The sky observed by the two IRAC channels (3.6 and 4.5 μm, or IRAC-1 and -2) fields of view (FOVs) is slightly offset with the central $\sim 10' \times 10'$ region, centered on 03:29:06 +31:19:30, covered by both channels. Although the observations in the central region were not obtained at exactly the same time in both bands, they were obtained within minutes, and we take them to be functionally simultaneous. These observations were obtained under program ID 61026, between 2011 Oct 10 and 2011 Nov 14. This campaign was conducted entirely in the fast cadence mode described in R14 (8 observations made every 3.5 days with non-uniform spacing ranging from 4 to 16 hrs to reduce aliasing). NGC 1333's location near the ecliptic provides for minimal field rotation during the Spitzer monitoring program, such that the majority of objects detected in this region were able to be monitored for the full campaign, producing light curves with 72 epochs over 35 days for most of the standard set of members (selected as described in R14 and below in Sec. 4.5).

Because NGC 1333 is not exactly on the ecliptic, there was some field rotation, and because of the very IR-bright objects in the middle of the field, the rotation of the diffraction spikes was enough to affect some photometry of some nearby faint objects in the region surrounding the bright sources. All individual objects identified as variable in the rest of this paper were specifically investigated for this effect, and bad points were removed.

We note that our photometry (regardless of the nature of the source) becomes noisy and incomplete fainter than [3.6]∼[4.5]∼16 mags (Fig. 2 below); sources this faint receive special scrutiny before being identified as variable.
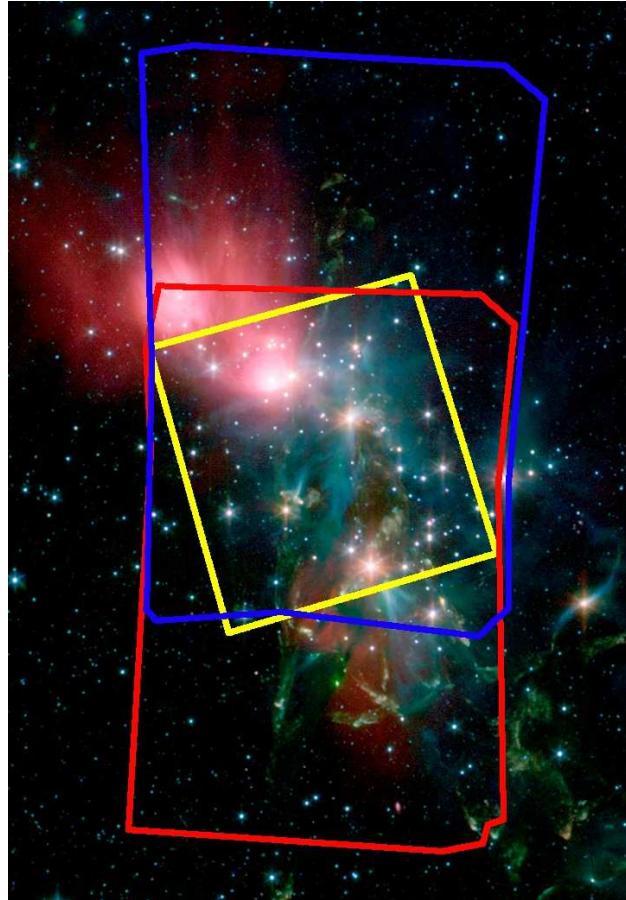
Fig. 1.— Solid red and blue lines indicate the approximate sky coverage (footprint) for a summed image of of YSOVAR NGC 1333 observations, superimposed on a 3-color image of NGC 1333 obtained during the cryogenic mission (image: SSC press release 2005-24a, NASA/JPL-Caltech/R. A. Gutermuth, Harvard-Smithsonian CfA). The blue line is 3.6 μm, the red line is 4.5 μm (the region where they overlap is where we have 2-band light curves). The yellow square indicates archival Chandra data coverage. The image is about 25′ top-to-bottom; the center of the YSOVAR coverage is 3h29m05.75s,+31d19m30.0s (J2000).
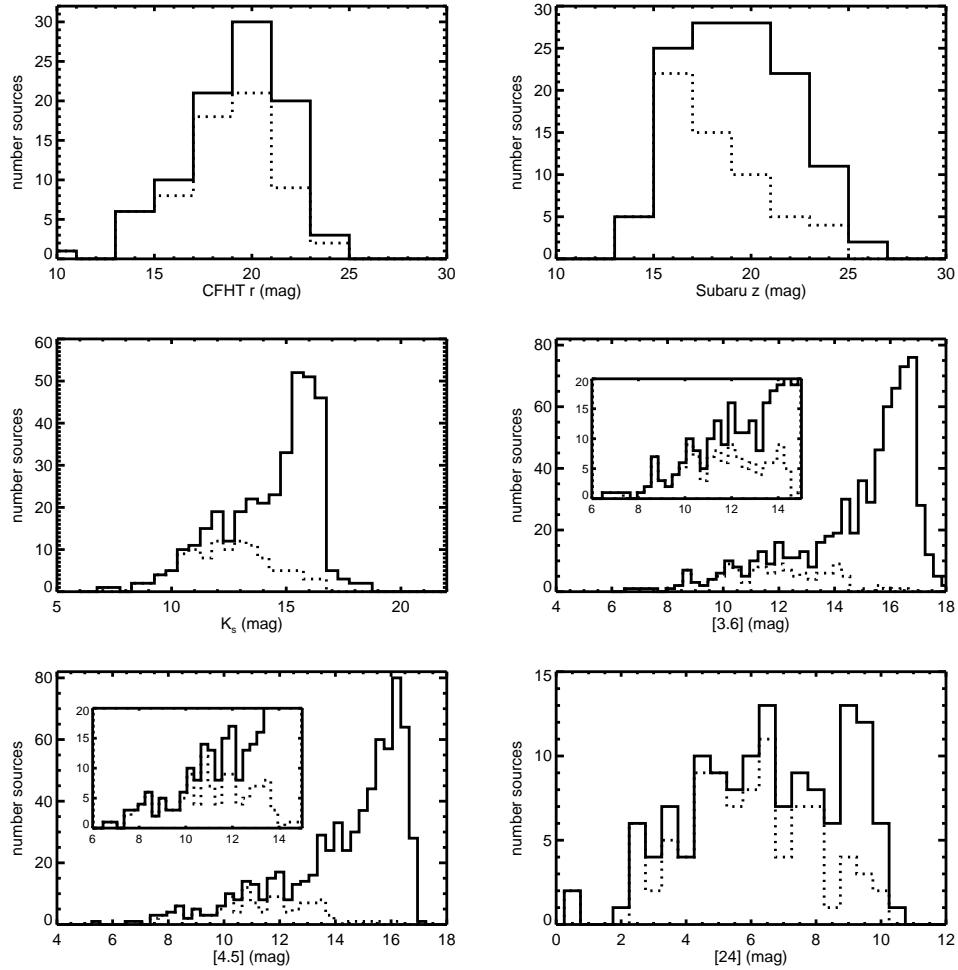
Fig. 2.— Histograms of some of the single-epoch optical, NIR, and MIR measurements used to assemble SEDs in NGC 1333, just for objects with light curves. Solid line is everything in the database (with a light curve); dotted line is standard set of cluster members (selected as described in R14 and below in Sec. 4.5). The CFHT r and Subaru z bands are representative of the optical bands; the set of objects with optical counterparts is strongly biased towards members (the standard set) and variables because a complete catalog over the whole NGC 1333 field was not obtained. K_s is representative of the NIR bands; the available data reach far deeper than the standard set of members, and the standard set of members represent most if not all of the brightest objects. The [3.6] and [4.5] histograms show the range over which there are YSOVAR light curves (down to [3.6]$\sim$[4.5]$\sim$16), and the relatively small, bright fraction that are members. (The inset plots for both of these channels enlarge the transition where the fraction of members is falling off.) By [24], typically, only the members are bright enough to be detected, and the sample of all detections is again dominated by members. The dataset spans very different brightnesses as a function of wavelength, but the standard set of members always dominates the bright end of the distribution.

Table 1. Contents of Single-Value Object Catalog[a]

Number	Format	Units	Label	Explanations
1	A18	—	cat	SSTYSV catalog name (HHMMSS.ss+DDMMSS.s; J2000)
2	F10.6	deg	RA	RA in decimal degrees, J2000
3	F10.6	deg	Dec	Dec in decimal degrees, J2000
4	F7.2	AB mag	cfht_umag	u-band AB magnitude from CFHT
5	F7.2	AB mag	e_cfht_umag	error on u-band AB magnitude from CFHT
6	F7.2	AB mag	cfht_gmag	g-band AB magnitude from CFHT
7	F7.2	AB mag	e_cfht_gmag	error on g-band AB magnitude from CFHT
8	F7.2	AB mag	cfht_rmag	r-band AB magnitude from CFHT
9	F7.2	AB mag	e_cfht_rmag	error on r-band AB magnitude from CFHT
10	F7.2	AB mag	cfht_imag	i-band AB magnitude from CFHT
11	F7.2	AB mag	e_cfht_imag	error on i-band AB magnitude from CFHT
12	F7.2	AB mag	subaru_imag	i'-band AB magnitude from Subaru
13	F7.2	AB mag	e_subaru_imag	error on i'-band AB magnitude from Subaru
14	F7.2	AB mag	subaru_zmag	z'-band AB magnitude from Subaru
15	F7.2	AB mag	e_subaru_zmag	error on z'-band AB magnitude from Subaru
16	A4	—	l_J	Limit flag on J
17	F6.2	mag	J	J band magnitude
18	F6.2	mag	e_J	Uncertainty in J
19	A4	—	l_H	Limit flag on H
20	F6.2	mag	H	H band magnitude
21	F6.2	mag	e_H	Uncertainty in H
22	A4	—	l_Ks	Limit flag on Ks
23	F6.2	mag	Ks	Ks band magnitude
24	F6.2	mag	e_Ks	Uncertainty in Ks
25	A4	—	l_[3.6]	Limit flag on [3.6]
26	F6.2	mag	[3.6]	Spitzer/IRAC 3.6 μm band magnitude
27	F6.2	mag	e_[3.6]	Uncertainty in [3.6]
28	A4	—	l_[4.5]	Limit flag on [4.5]
29	F6.2	mag	[4.5]	Spitzer/IRAC 4.5 μm band magnitude
30	F6.2	mag	e_[4.5]	Uncertainty in [4.5]
31	A4	—	l_[5.8]	Limit flag on [5.8]
32	F6.2	mag	[5.8]	Spitzer/IRAC 5.8 μm band magnitude
33	F6.2	mag	e_[5.8]	Uncertainty in [5.8]
34	A4	—	l_[8.0]	Limit flag on [8.0]
35	F6.2	mag	[8.0]	Spitzer/IRAC 8.0 μm band magnitude
36	F6.2	mag	e_[8.0]	Uncertainty in [8]
37	A4	—	l_[24]	Limit flag on [24]
38	F6.2	mag	[24]	Spitzer/MIPS 24 μm band magnitude
39	F6.2	mag	e_[24]	Uncertainty in [24]
40	A4	—	l_[70]	Limit flag on [70]
41	F6.2	mag	[70]	Spitzer/MIPS 70 μm band magnitude
42	F6.2	mag	e_[70]	Uncertainty in [70]
43	F6.2	—	logfx	log of F_x, where F_x is in units of ergs cm^{-2} s^{-1}
44	F6.2	—	logfxerr	error on log of F_x, where F_x is in units of ergs cm^{-2} s^{-1}
45	F6.2	—	loglx	log L_x, where L_x is in units of ergs s^{-1}
46	I3		glvary_index	Gregory-Loredo index (see R14); the larger the number, the greater the X-ray variability
47	A12	—	SpTy	Spectral type
48	A10	—	SpTySrc	Origin of spectral type (literature)
49	I4	K	Teff	$T_{\rm eff}$ from Foster et al. (2015)
50	F6.2	—	oursedslope24	SED slope (from 2 to 24 μm; see text)
51	A5	—	oursedclass24	SED class (from 2 to 24 μm; see text)
52	I2	—	YSOlit	Is this a literature YSO (see text)? 1=yes, 0=no
53	I2	—	YSOstd	Is this a part of the standard set of YSOs (see text)? 1=yes, 0=no
54	I2	—	YSOx	Was this selected for the standard set of YSOs based on X-rays (see text)? 1=yes, 0=no
55	I2	—	YSOaug	Is this a part of the augmented set of YSOs (see text)? 1=yes, 0=no

Table 1—Continued

Number	Format	Units	Label	Explanations
56	I2	—	CYvar	Is this CY variable (see text)? 1=yes, 0=no
57	I2	—	Var	Is this variable over the YSOVAR campaign? 1=yes, 0=no
58	I2	—	VarMem	Is this a newly identified member based on variability? 1=yes, 0=no
59	I4	—	Npts_i1	Number of points in [3.6] for YSOVAR campaign
60	F6.2	mag	Mean_i1	Mean [3.6]
61	F6.2	mag	Median_i1	Median [3.6]
62	F6.2	mag	Sdev_i1	Standard deviation [3.6]
63	F6.2	mag	Max_i1	Maximium [3.6]
64	F6.2	mag	Min_i1	Minimum [3.6]
65	F6.2	days	Range_JD_i1	Length of [3.6] light curve
66	F6.2	mag	Ampl1090_i1	Amplitude of [3.6] light curve, defined as 10-90% range.
67	F6.2	—	Chisq_i1	$\chi^2([3.6])$
68	F6.2	days	Timescale_i1	Timescale for [3.6]
69	F6.2	days	Period_i1	Period for [3.6], if applicable
70	F6.2	—	M_i1	M metric for [3.6] as per Cody et al. (2014)
71	F6.2	—	Ms_i1	M metric for smoothed [3.6] as per Cody et al. (2014)
72	F6.2	—	Q_i1	Q metric for [3.6] as per Cody et al. (2014)
73	F6.2	—	Qlt_i1	Q metric for long-term-trend-subtracted [3.6] as per Cody et al. (2014)
74	I4	—	Npts_i2	Number of points in [4.5] for YSOVAR campaign
75	F6.2	mag	Mean_i2	Mean [4.5]
76	F6.2	mag	Median_i2	Median [4.5]
77	F6.2	mag	Sdev_i2	Standard deviation [4.5]
78	F6.2	mag	Max_i2	Maximium [4.5]
79	F6.2	mag	Min_i2	Minimum [4.5]
80	F6.2	days	Range_JD_i2	Length of [4.5] light curve
81	F6.2	mag	Ampl1090_i2	Amplitude of [4.5] light curve, defined as 10-90% range.
82	F6.2	—	Chisq_i2	$\chi^2([4.5])$
83	F6.2	days	Timescale_i2	Timescale for [4.5]
84	F6.2	days	Period_i2	Period for [4.5], if applicable
85	F6.2	—	M_i2	M metric for [4.5] as per Cody et al. (2014)
86	F6.2	—	Ms_i2	M metric for smoothed [4.5] as per Cody et al. (2014)
87	F6.2	—	Q_i2	Q metric for [4.5] as per Cody et al. (2014)
88	F6.2	—	Qlt_i2	Q metric for long-term-trend-subtracted [4.5] as per Cody et al. (2014)
89	F6.2	mag	Mean_i1i2	Mean [3.6]−[4.5]
90	F6.2	mag	Sdev_i1i2	Standard deviation [3.6]−[4.5]
91	F6.2	days	Period_i1i2	Period for [3.6]−[4.5], if applicable
92	F6.2	—	Stetson_i1i2	Stetson index for [3.6], [4.5]
93	F6.2	—	Correl_i1i1i2	Correlation coefficient for [3.6] vs. [3.6]−[4.5] CMD.
94	F6.2	—	CorrelProb_i1i1i2	Probability that correlation is real in [3.6] vs. [3.6]−[4.5] CMD.
95	F6.2	—	Correl_i2i1i2	Correlation coefficient for [4.5] vs. [3.6]−[4.5] CMD.
96	F6.2	—	CorrelProb_i2i1i2	Probability that correlation is real in [4.5] vs. [3.6]−[4.5] CMD.

[a]Entire data table available online at the journal. This table provided as a guide to the contents of the table.

2.2. YSOVAR Data from PAIRITEL

Near-IR observations were obtained using the Peters Automated Infrared Imaging Telescope (PAIRI-TEL; Bloom et al. 2006), which is an automated 1.3 m telescope. PAIRITEL was located at the Whipple Observatory at Mt. Hopkins, Arizona; the same telescope and camera used for the northern part of 2MASS, PAIRITEL acquired simultaneous $J, H,$ and K_s images. The observations of NGC 1333 were obtained over 24 epochs from 7 October 2010 to 19 November 2012. The PAIRITEL pipeline version 3 was used, which linearizes the data and combines individual exposures to produce mosaics and "weight" map products for each epoch and filter. The mosaic products from this pipeline have a scale of $1''0$ pixel^{-1} and the world coordinate system (WCS) has a typical pointing error of less than an arcsec.

Photometry from the PAIRITEL images was extracted using a data reduction pipeline developed at SAO. We examined each epoch's mosaics to exclude data with insufficient coadds due to poor weather and other artifacts in the data. We then checked each weight frame to find an appropriate cutoff level (in terms of numbers of coadds) for the epoch, then masked the unreliable data so that it would not impact the derived photometry. The SAO pipeline uses the IRAF[2] package *daofind* to detect all point sources 4σ above the background noise level with a full-width half-maximum of $2.2''$. Photometry was performed with the IRAF *phot* task, using an aperture radius of 5 pixels and a sky annulus radius of 10 pixels. We combined the data from the three bands into a common catalog using a script to match objects by position. This process is iterated, applying small shifts to the individual catalogs, to correct their relative offsets and minimize the mean position error between the bands. After obtaining the 3-band catalog, another script matches the objects to 2MASS positions, refines the PAIRITEL astrometry, generates object IDs and associates the PAIRITEL detections with their corresponding 2MASS objects where possible. The photometry is then calibrated using an iterative routine that minimizes the offset between the 2MASS and PAIRITEL photometry measurements, using all objects with a signal to noise >30. This process was repeated for each epoch, and the photometry combined into a master catalog that contains the photometric measurements of all bands and sources. The typical standard deviation of sources not detected as variable is on the order of 0.05 mag for J and H band, and 0.08 mag for K_s band.

The PAIRITEL data were taken over a span of $\sim$2.5 years, far longer than the YSOVAR campaign. Due largely to bad weather, there are at most 5-8 epochs during the YSOVAR campaign, and two immediately following it. We can find PAIRITEL counterpart light curves for 122 objects with YSOVAR light curves (out of about 300 in the region that was monitored in both JHK_s and IRAC). Out of the $\sim$65 light curves determined below to be *variable* over the YSOVAR campaign, there are 53 with a J, H, and/or K_s light curve. For about 30% of these light curves, the JHK_s data light curves have very similar structure (and often amplitude) as for the IRAC light curves. Morales-Calderón et al. (2011) found many such cases in Orion; similar light curve structure from 1 to 5 μm is expected for stars without disks (arising in stellar phenomena such as rotation of surface inhomogeneities) and can also occur for some physical mechanisms for stars with disks (such as accretion bursts, particularly when our view angle is from well above the disk). However, many NGC 1333 members (standard or augmented set of members) show near and mid-IR light curves with quite disparate structure, indicative of different physical mechanisms at work.

---

[2]IRAF is distributed by the National Optical Astronomy Observatory, which is operated by the Association of Universities for Research in Astronomy (AURA) under cooperative agreement with the National Science Foundation.

3. Large Archival Datasets

We compiled additional photometry from several different sources in order to assemble spectral energy distributions (SEDs) for our targets and to identify members; this process is reported in R15. While many of our targets vary significantly, single-epoch archival data can help define the SED such that, in some cases, the assembled SED can reveal the underlying nature of the source, or at least help narrow the possibilities for the nature of the source. We also use the slope of the SED between 2 and 24 μm to define SED classes into which our objects fall; see R14 and R15.

To summarize the most salient points from R15, all of the catalogs described here were merged by position with a catalog-dependent search radius (usually $\sim 1''$). Many sources, especially those in regions where many sources are close together on the sky, or those that had particularly strange SEDs, were also inspected and matched by hand. Data from the Widefield Infrared Survey Explorer (WISE; Wright et al. 2010) at 3.4, 4.5, 12, and 22 μm were included in a few specific cases after inspection of the WISE images.

In order to give a sense of the brightness, faintness, and completeness limits of these data sets, representative histograms of these single-epoch measurements for the objects with light curves appear in Figure 2. The baseline catalog from R15 was assembled initially without regard to membership, variability, or the existence of light curves; however, in this paper, we restrict ourselves to those objects with light curves. The histograms in Fig. 2 are shown for both the entire set of objects with light curves, and for those in the standard set of members (selected as described in R14 and below in Sec. 4.5, where issues of contamination are also raised).

Single-valued measurements (such as the single-epoch optical photometry) or metrics (such as the SED slope and class, or mean from the light curve, etc.) for all of the objects with light curves are collected in Table 1. The JHK and cryo-era Spitzer data (as well as the SED slopes and classes) are reported in R15, but are repeated in Table 1 for convenience. The multi-epoch data tables will appear in the delivery of these data to IRSA.

3.1. Cryogenic-era Spitzer Archival Data

Early in the Spitzer mission, NGC 1333 was observed by both the guaranteed time observations (GTO) and the Cores-to-Disks (c2d) Legacy program (Evans et al. 2003, 2009), with both IRAC and the Multiband Imaging Photometer for Spitzer (MIPS; Rieke et al. 2004). Gutermuth et al. (2008, 2009, 2010) present methodology for identifying YSOs from the cryogenic catalog. The details of the selection process appear in those papers, but in summary, multiple cuts in multiple color-color and color-magnitude diagrams are used to identify YSO candidates, as distinct from, e.g., extragalactic and nebular contamination. We compute this classification as part of the YSOVAR processing, and we have adopted this YSO selection mechanism as part of one of the primary YSOVAR sample definitions (R14), which we apply here to the NGC 1333 data set.

Spitzer data are also available from the c2d program data deliveries, served by IRSA. The data used for these deliveries are typically the same BCDs as were used in the cryogenic data that we re-reduced above. As such, then, they are not independent measurements, and these data were only used to supplement our cryogenic-era catalog if a band was missing (which may happen due to low signal-to-noise). The c2d

catalog includes measurements at 70 μm and band-filled upper limits[3] between 3.6 and 24 μm, which we incorporated.

Histograms of some of these cryo-era measurements for objects with YSOVAR light curves appear in Figure 2. For the objects with light curves, there are 3.6 μm (IRAC-1) measurements complete down to about 16.5 mags, and there are 4.5 μm (IRAC-2) measurements complete down to about 16 mags. The histograms are not shown, but there are 5.8 μm (IRAC-3) measurements complete down to about 15 mags, and there are 8 μm (IRAC-4) measurements complete down to about 14 mags. Completeness is harder to assess for the MIPS bands. There are 24 μm (MIPS-1) measurements as faint as 10th mag (Fig. 2). There are just five objects with light curves and 70 μm (MIPS-2) measurements; they range from -3.7 to 1.1 mags. Overall, the objects identified as part of the standard set of members (defined in R14 and below in Sec.4.5) in Figure 2 are distinctly brighter than the rest of the sources. While the overall peak [3.6] in Fig. 2 is fainter than 16th mag, the histogram of the standard set of members is much flatter, and peaks at 14th mag. Similar behavior can be seen in the other three IRAC bands. The sources bright enough to be seen at 24 μm, however, are strongly biased towards those sources that are also in the standard set of members, though these members are on average brighter.

Cryogenic data between 3.6 and 8 μm are available for typically 90-100% of all the objects with light curves, and essentially all of the members (standard or augmented) or variables. Data at 24 μm are rarer, with 62% of all the light curves having a counterpart at [24], though 80-90% of the members (standard or augmented) or variables have counterparts. Less than 1% of the light curves have a match at [70], and $\sim$4% of the standard members or variables have a match at [70].

3.2. 2MASS and 2MASS 6×

NGC 1333 was covered in the Two-Micron All Sky Survey (2MASS; Skrutskie et al. 2006) and was also located in a field targeted by the long exposure 6× 2MASS program. As described in R15, we included these main 2MASS catalog and deeper 6× catalog NIR JHK_s data into our database. We also include the $\sim$30 deep JH space-based measurements from Greissl et al. (2007) for the targets discussed there. These data were merged into the rest of the catalog by position with a 1″ search radius.

Histograms of the K_s measurements for those objects with light curves appear in Figure 2, and the JHK_s values themselves appear in R15 but are repeated in Table 1 for reference. The J histogram (not shown) peaks at about 17.5 mag, the H histogram (not shown) peaks at about 17th mag, and the K_s histogram (Fig. 2) peaks at about 16th mag. As at IRAC wavelengths, the NGC 1333 standard set of members is distinctly brighter in JHK_s than the rest of the catalog. In the K_s histogram, the distribution of standard members peaks at $\sim$13, 3 magnitudes brighter than the peak of the rest of the catalog. Similar behavior can be seen at J and H.

About half of all the objects with light curves have a counterpart at JHK_s, and $\sim$90% of the the members (standard or augmented) and variables have such counterparts.

---

[3]That is, if a source was known to be at a given location because of information from other bands, but it was not detected independently in a given band, then an aperture was placed at the location expected for the source and an upper limit determined for that band.

3.3. Chandra ACIS

Chandra X-ray Observatory Advanced CCD Imaging Spectrometer for wide-field imaging (ACIS-I) observations of NGC 1333 were first reported in Getman (2002) and then Winston et al. (2009, 2010). There are three pointings in NGC 1333, with obsids 642, 6436, and 6437, with a total exposure time of 119.3 ks.

As we described in R14, we re-reduced the Chandra data in a self-consistent way across most of the YSOVAR clusters. Source detection was performed using CIAO (Chandra Interactive Analysis of Observations; Fruscione et al. 2006). Sources, even faint ones, were retained if they had a counterpart in the cryogenic IRAC catalog. We also tested the X-ray light curves for variability using the Gregory-Loredo method (GL-vary; Gregory & Loredo 1992). This method uses maximum-likelihood statistics and evaluates a large number of possible break points from the prediction of constancy. This method assigns an index to each lightcurve – the higher the value of the index, the greater the variability. Index values greater than 7 indicate $> 99\%$ variability probability. Values of the GL-vary index >9 usually indicate flares. The GL-vary index is not reliable, however, for sources with less than about 30 raw counts. Values for F_x, L_x, and GL-vary for sources in our region with X-ray detections appear in Table 1. Sources from Chandra were matched to the rest of the catalog with a position-dependent search radius. There are no new sources that do not already have an X-ray detection (from ROSAT, XMM, and/or Chandra) in the literature (R15). Just 13% of objects with light curves have an X-ray counterpart. However, half the standard set of members (and $\sim 40\%$ of the augmented set of members) have L_x.

It is well-known that YSOs are often bright in X-rays, and thus we can use X-ray data to identify YSOs that do not have IR excesses. As discussed in R14, we improved our inventory of YSOs in NGC 1333 by identifying objects with X-ray detections, IRAC counterparts, and SEDs that are consistent with those of stars. We have adopted this YSO selection mechanism as the other main component of the primary YSOVAR sample definition; see R14, R15, and Sec. 4.5 below.

3.4. Subaru *Suprime-Cam* and CFHT *MegaCam*

NGC 1333 was observed in several optical bands from Subaru and the Canada-France-Hawaii Telescope (CFHT), and we obtained these data from the public archives. Optical data from both telescopes cover the full extent of the region monitored for YSOVAR. As noted in R15, broadband optical imaging over this region has not been reported for many sources, so its addition can contribute substantially to identification of the object nature.

NGC 1333 was observed in the i' and z' bands with the *Suprime-Cam* wide-field camera (Miyazaki et al. 2002) on Subaru on 2006-11-18. A total of 1 short exposure (10 s) and 60 dithered long exposures (60 s) were obtained in each filter as part of the SONYC project (Scholz et al. 2009, 2012ab). The raw data and corresponding calibrations were retrieved from the public archive (Baba et al. 2002).

The individual raw Subaru images were processed using an updated version of *Alambic* (Vandame 2002), a software suite developed and optimized for the processing of large multi-CCD imagers, and adapted for *Suprime-Cam*. *Alambic* includes standard processing procedures such as overscan and bias subtraction for each individual readout ports of each CCD, flat-field correction, bad pixel masking, CCD-to-CCD gain harmonization, and fringing correction, registration of the individual images (using 2MASS as a reference) and stacking. Point-spread-function (PSF) photometry was extracted from the final mosaics using *SExtractor* (Bertin & Arnouts 1996) and *PSFEx* (Bertin 2011). The photometric zero-points (Vega-based zero points)

were derived using standard fields obtained the same night.

NGC 1333 was observed in the *ugri* filters at several epochs (see Table 2) with the *MegaCam* wide-field camera (Boulade et al. 2003) mounted on the Canada France Hawai'i Telescope (CFHT) as part of the DANCE survey (Bouy et al. 2013). The individual CFHT images were retrieved from the public archives maintained at the Canadian Astronomy Data Centre.

The raw CFHT images were processed and calibrated with the recommended *Elixir* system (Magnier & Cuillandre 2004), which includes detrending (darks, biases, flats and fringe frames). Nightly magnitude zero-points (Vega-based zero points) were derived by the CFHT team using Sloan Digital Sky Survey (SDSS) observations of standard star fields (Smith et al. 2002, Landolt 1992). A precise astrometric and photometric registration of all the individual images was obtained by first extracting PSF photometry from the individual images using *SExtractor* and *PSFEx*, and then registering and aligning the individual catalogs on the same photometric scale using *Scamp* (Bertin 2006). The final deep mosaics were produced using *SWarp* (Bertin et al. 2002), and the sources astrometry and PSF photometry were measured using *SExtractor*.

The resultant photometry from the CFHT and Subaru telescopes is well-matched to each other (where there is overlap), and on average well-matched to the rest of the assembled SEDs. The data appear in Table 1. Note that these are AB magnitudes, consistent with SDSS convention, whereas the other magnitudes reported here are Vega magnitudes. The reported errors on these data are purely statistical, not systematic, and thus the errors are likely underestimated.

Histograms of the CFHT r and the Subaru z measurements for those objects with light curves appear in Figure 2. The distributions for all the optical bands peak at $\sim$20th mag and reach as faint as $\sim$25th mag. Unlike the cryo-era Spitzer or JHK_s catalogs, the optical measurements were only obtained for those sources we thought might be 'interesting', so they are strongly biased towards members and/or variable objects. This can be seen in the histograms in Figs. 2, where the histograms for all the CFHT r or Subaru z measurements are very similar to just the members (selected in Sec. 4.5). Similar results are obtained for the other optical bands.

Just 5-20% of all the objects with light curves have an optical measurement from Subaru or CFHT. About half of the standard set of members (and $\sim$45% of the augmented set of members) have a Subaru or CFHT counterpart at any one band. About half of the variables have a Subaru or CFHT counterpart at any one band.

3.5. Literature Data

R15 assembled literature data from more than 25 published sources, from 1994 to 2014, including cross-identifications and wavelengths ranging from X-rays to 3 and 6 cm VLA data, but focusing on J (1.25 μm) to 24 μm. For many of the older studies, the cross-IDs (nomenclature) is the most important thing to retain, since the data have since been reprocessed or superceded by later observations; see R15. The catalog presented in R15 provides the literature basis on which we build now. The coordinates in this catalog are all linked to 2MASS, so they are well-matched to the YSOVAR coordinates.

We note here that most of the spectral types in the literature come from searches for brown dwarfs, so the distribution is highly skewed to mid-M and later. There are about 100 objects with light curves that have an estimate of spectral type in the literature, including coarse ones (e.g., "<M0"). Foster et al. (2015), in an analysis of near-IR spectra obtained with the Apache Point Observatory Galactic Evolution

Experiment (APOGEE; Zasowski et al. 2013), obtain $T_{\rm eff}$ values for many of their targets based on spectral model fitting. Target selection for that project included considerations based on the variability of objects in the YSOVAR data, so many of the objects in which we are interested in the context of YSOVAR also have measurements in Foster et al. from APOGEE. The $T_{\rm eff}$ values from Foster et al. (2015) can be used to constrain the spectral type, even though the $T_{\rm eff}$ are much more uncertain. Spectral types and $T_{\rm eff}$ values appear in R15 and are repeated in Table 1 for reference.

4.   Subsets of the Data and Sample Properties

In this section, we define the scope of the dataset – numbers of sources and categories (members/non-members, variables, etc.). Table 3 collects many of the relevant numbers and fractions.

4.1.   IRAC Light Curves: Spatial and Temporal Distribution

There are 701 objects in our NGC 1333 fields for which we have an IRAC light curve with at least five viable[4] points in 3.6 and/or 4.5 μm, 194 just in 3.6 μm, 265 just in 4.5 μm, and 242 with light curves in both IRAC channels. Their locations on the sky are shown in Figure 3. Objects with a light curve in only one band in the region where there is 2-band coverage are for the most part faint, where one band is below the detection threshhold and the other is not, and the remaining cases are where one band is compromised by instrumental effects whereas the other is not.

As described in R14, all YSOVAR clusters have at least one sequence of fast cadence observations, used to compute the 'standard set for statistics' to enable fair comparisons between clusters. In NGC 1333, all of the YSOVAR observations are fast cadence. We select variables following R14; the approach is summarized below in Sec. 4.2. Figure 4 shows cumulative distribution functions of the lengths of the light curves for both channels. Most ($>80\%$) of the light curves overall, and most ($>90\%$) of the light curves tagged variable, are longer than 30 days, with a strong peak at $\sim$35 days. There are only five light curves tagged variable with length <30 days in either channel; they are often objects with light curves in both bands, though tagged variable based on the characteristics of the longer light curve.

---

[4]'Viable', meaning obtained with sufficient redundancy on the sky as described in R14, and not obviously compromised in the images due to artifacts or cosmic rays; see discussion in R14.

Table 2.   Overview of CFHT *MegaCam* observations

Date YYYY-MM-DD	Filters	Exp. time sec
2005-09-27	g	4×40
2008-12-21	i	9×560
2009-03-24	i	1×56
2009-03-26	i	1×56
2009-09-21	i	2×10 & 2×160
2005-09-27	r	4×40
2005-09-27	u	3×150
2005-12-23	u	2×150
2006-02-28	u	3×150
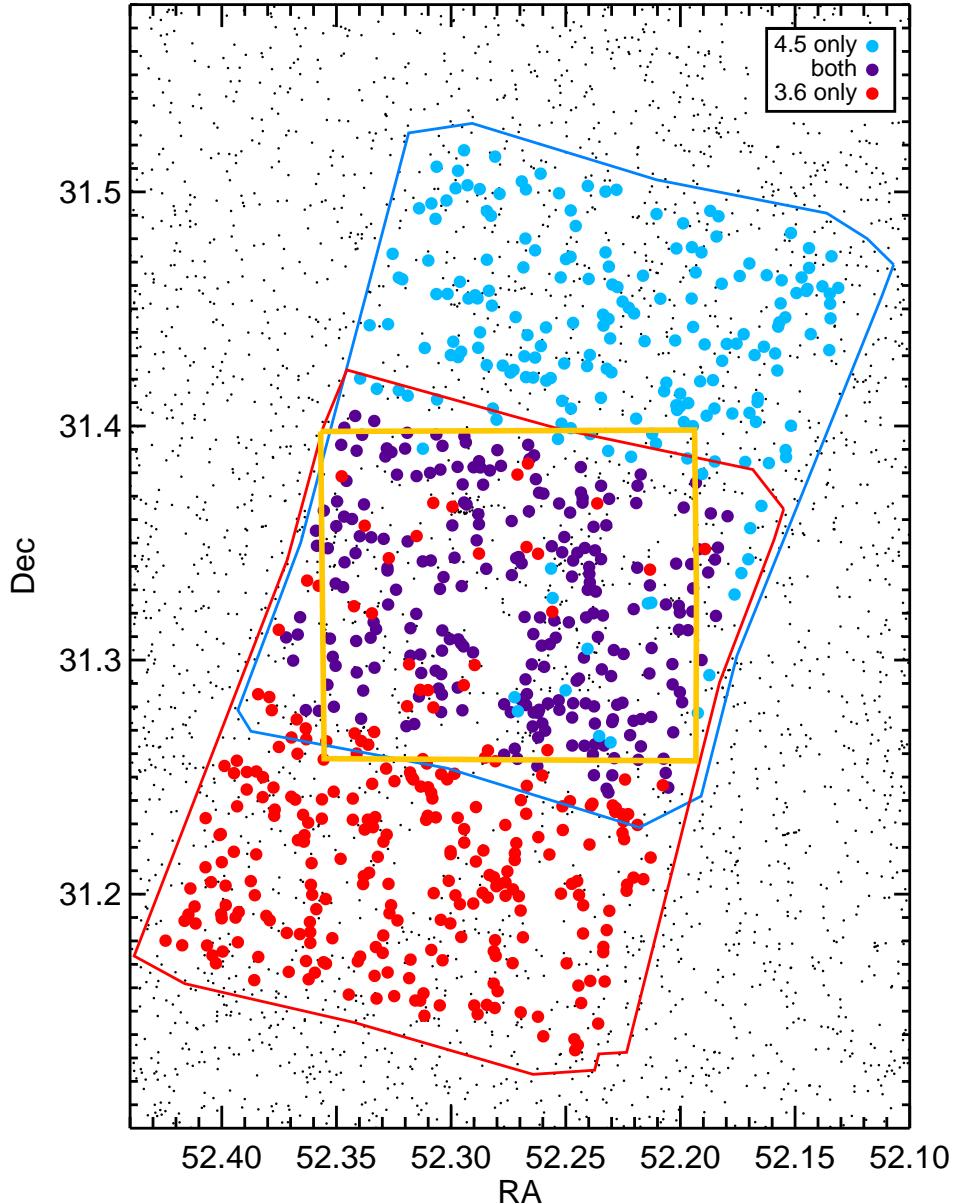
Fig. 3.— Sky locations of objects with YSOVAR light curves. Small black dots throughout region are objects on the sky in our literature catalog (from R15). Large blue dots are objects with light curve only in [3.6]. Large red dots are objects with light curve only in [4.5]. Large purple-black dots are objects with light curves in both [3.6] and [4.5]. Objects with a light curve in only one band in the region where there is 2-band coverage are for the most part faint, where one band is below the detection threshhold and the other is not, or one band is compromised by instrumental effects whereas the other is not. Blue polygon is the [3.6] footprint; red polygon is the [4.5] footprint; yellow square is the Chandra coverage.
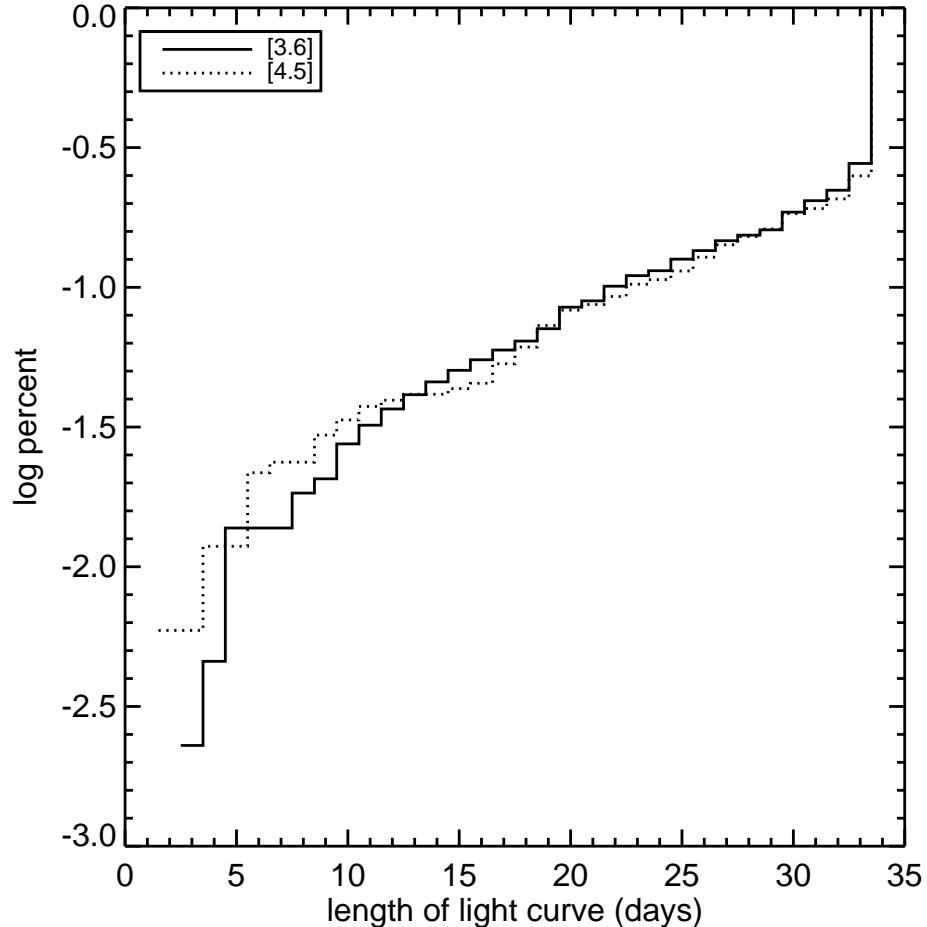
Fig. 4.— Cumulative distribution functions of the length of the light curves, in days, for the [3.6] (solid) and [4.5] (dotted). The y-axis is the log of the sample fraction. The peaks (at 35 days) of the histograms reach a total number of 315 for [3.6] and at 379 for [4.5]. Most (>80%) of the light curves overall, and most (>90%) of the light curves tagged variable, are longer than 30 days, with strong peaks at 35 days.

4.2.   Identifying Variables in the YSOVAR Campaign

As described in detail in R14, we use three different methods of finding variables in our light curves: Stetson index, χ^2 relative to a flat nonvariable lightcurve, and periodicity tests. We now briefly summarize this approach.

For those objects where there are both [3.6] and [4.5] data, we can calculate the Stetson index, given by:

$$S = \frac{\sum\limits_{i=1}^{p} g_i sgn(P_i) \sqrt{|P_i|}}{\sum\limits_{i=1}^{N} g_i} \tag{1}$$

where p is the number of pairs of observations for a star taken at the same time, P_i is the product of the normalized residuals of two observations, g_i is the weight assigned to each normalized residual, and sgn means 'the sign of'. In our case the weights are all equal to one. As established in R14, if the Stetson index is >0.9, the object is variable. The values of the Stetson index for our objects are given in Table 1. Fifty-six objects in our field of view are identified as variable using the Stetson index.

For those objects where only one band of data exists at all (or where one band may be corrupted by instrumental effects), we can identify variables from the chi-squared test (χ^2), which, for a given band, is given by

$$\chi^2 = \frac{1}{N-1} \sum_{i=1}^{N} \frac{(mag_i - \overline{mag})^2}{\sigma_i^2} \tag{2}$$

where σ_i is the estimated photometric uncertainty. Again, as established in R14, we take objects with $\chi^2 > 5$ as variable. The χ^2 values for our objects are given in Table 1, and the total counts of objects are in Table 3. For [3.6], 54 objects have $\chi^2 > 5$, and for [4.5], 57 objects have $\chi^2 > 5$. Of these χ^2 variable objects, however, 45 have light curves in both IRAC channels, and were selected as variable via their Stetson indices. As a result, a total of 16 objects were newly identified as variable by one-band χ^2 calculations.

Finally, as described in R14, we searched independently for periodic behavior in the [3.6], [4.5], and [3.6]−[4.5] light curves, between 0.05 and 15 d (from the sampling to ∼half the length of the campaign). We adopt the period obtained from [3.6] as the most reliable, then [4.5], and then [3.6]−[4.5] as the least reliable. Periods measured for our objects are given in Table 1. Any periodic objects not identified as variable using the Stetson index or the χ^2 test are added to the set of variable objects. There are 23 objects for which we can derive a period in NGC 1333; 6 of them are identified as variable solely on the basis of the periodic signal.

For each of the variable objects, we manually inspected the light curves and the images to make sure that the photometry was not significantly compromised due to residual instrumental effects not corrected by the processing described above (and more extensively in R14). As mentioned above and in R14, IRAC light curves for objects fainter than ∼16 mag in either band are particularly noisy, and were given special scrutiny. None of the objects in NGC 1333 that we identify as variable have $[3.6]\sim[4.5]\gtrsim16$. One (SSTYSV 032912.05+311305.8) has, from the cryo era, $[3.6]>16$ and $[4.5]<16$, but a YSOVAR light curve only in [4.5].

In the end, there are 78 objects in the NGC 1333 YSOVAR campaign data that we have identified as mid-IR variable from the YSOVAR fast-cadence monitoring. These mid-IR variable objects are shown on the sky in the left panel of Figure 5. Although the variable objects were selected without regard to membership

status, the variable objects are clustered on the sky in a manner similar to the members, e.g., there is a visible clumping of the variables in the central region, and far fewer in the regions of single-band coverage.

Additional information about, e.g., fraction of the standard members (selected in §4.5 below) that are variable (67/130=52%), is provided in Table 3.

We note here explicitly that the remaining 701-78=623 objects are not detected as variable (NDAV) in the YSOVAR campaign. Monitoring at a different wavelength or cadence may find variability in these objects.

4.3. Identifying Cryo-to-YSOVAR (CY) Variables

Separately from searching for variability *within* the YSOVAR campaign data, R14 looked for objects whose brightnesses at [3.6] and/or [4.5] had changed significantly ($>3\sigma$ based on the ensemble distribution) between the cryo-era observation and the mean of the YSOVAR light curves. Out of the entire set of 701 IRAC light curves in the NGC 1333 field, 92 can be identified as long-term mid-IR variable in this approach. In R14, those were referred to as "long-term variables" or "variable on the longest timescales". To limit nomenclature confusion within the YSOVAR suite of papers, we hereafter refer to these objects as "Cryo-to-YSOVAR" variables, or CY variables. The fraction of CY variables (13% over everything in the field; see Table 3) represents a higher fraction of variables than was found in the YSOVAR campaign alone, which is closer to 11% (again, over everything in the field). Just 32 of the 92 CY variables are also shorter-term variables, which emphasizes that the mechanism for selecting variables (and likely the underlying nature of the variability) is entirely different between the two approaches. There is some expectation based on numerous reports in the literature that larger amplitude variations are found when analyzing data spanning longer temporal baselines, which might explain these different fractions. However, it is important to note that the fraction of variables out of all objects in the field is physically very different than the fraction of members (defined in Sec. 4.5 below). Out of the standard set of members, 35/130 (∼30%; see Table 3) are CY variables, 28 of which are also found as variable over the YSOVAR campaign. The fact that there is a much higher fraction of member CY variables, combined with the expectation that more YSOs will be variable over a longer time baseline, gives us some hope that the CY variables are not extensively contaminated, despite the fact that the identification of variability relys upon a single epoch from the cryo era.

The distribution of these CY variables on the sky is shown in the right panel of Figure 5. It can be seen to be clustered in basically the same fashion as the members, which suggests limited contamination. However, it can be seen by eye that it is also somewhat less clustered than the standard set of members, particularly in the south, suggesting that there may be a higher contamination rate of non-cluster sources in this sample. On the other hand, the distribution of literature-identified members not selected as standard members (see §4.5) also extends towards the south.

4.4. SED Classification

After assembling all of the YSOVAR and literature photometry, including the mean [3.6] and [4.5] measurement from our YSOVAR campaign, we constructed each object's SED using all available data as collected above and in R15. Some objects have well-defined SEDs, with data from u to 8, 24, or even 70 μm; others have far less-well-defined SEDs, for example, only one point that is the mean from our YSOVAR
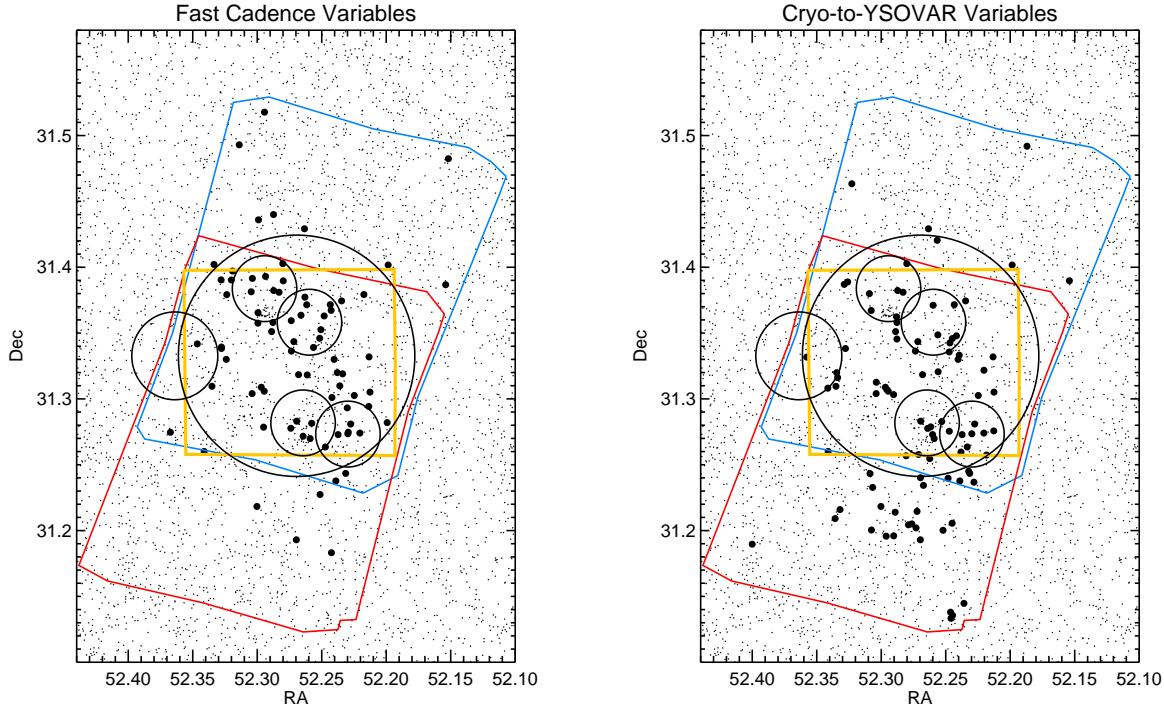
Fig. 5.— Locations of objects identified as variable in the mid-IR. Notation is similar to Figure 6, but large black dots indicate objects identified as variable (see text) – left panel has objects identified as variable from the fast cadence (YSOVAR) data (timescales of day to month); the right panel has objects identified as cryo-to-YSOVAR (CY) variable via a comparison between the cryo-era and YSOVAR data (timescales of years). Despite having been selected without reference to membership status, variable objects are clustered in a manner very similar to NGC 1333 members. The CY variable objects are not quite as tightly clustered, particularly in the south, suggesting that there may be a higher rate of non-cluster-member contamination.

campaign.

As discussed in R14 and R15, we defined an internally consistent SED classification for the YSOVAR sources. In the spirit of Wilking et al. (2001), we define the near- to mid-IR (2 to 24 μm) slope of the SED, $\alpha = d \log \lambda F_\lambda / d \log \lambda$, classifying sources with $\alpha > 0.3$ as Class I objects, 0.3 to -0.3 as flat-spectrum sources, -0.3 to -1.6 as Class II sources, and $\alpha < -1.6$ for Class III sources. For each of the YSOs and candidate YSOs in our sample, we performed a simple ordinary least squares linear fit to all available photometry (just detections, not including upper or lower limits) as observed between 2 and 24 μm, inclusive. Note that formal errors on the infrared points are so small as to not affect the fitted SED slope. Note also that the fit is performed on the observed SED, e.g., no reddening corrections are applied to the observed photometry before fitting. Classification via this method is provided specifically to enable comparison within this paper (and to other YSOVAR papers) via internally consistent means; see discussion in R14. We can perform this calculation only for those objects with points at more than one wavelength in their SED between 2 and 24 μm.

We adopt the SED slopes and classes determined by R15 between 2 and 24 μm. R15 explicitly compares these 2-24 μm SED classifications to those determined between a restricted wavelength range (2-8 μm) and

those SED classes reported in the literature. The 2 to 24 μm slopes and classes are repeated in Table 1 for reference.

4.5. Standard Members

As discussed in R14, we took a two-pronged approach to identify a 'standard set of members' selected in the same fashion across all YSOVAR clusters. We identify members for the standard set based on their IR colors using the Gutermuth et al. (2008, 2010) and G09 selection algorithm, and with X-ray observations – if they are detected in X-rays and have a star-like SED (Class III), we add them to the standard set of members. Very few of these IR- and X-ray-selected members have spectroscopic follow-up (or pre-existing spectra in the literature), and thus, most should be considered YSO candidates, though we include them all provisionally in the standard set of members.

Out of 701 objects in NGC 1333 with light curves, 130 are identified as part of the standard set of members. Most, 102, are identified using the G09 IR selection method; the remainder are identified via the X-ray+Class III SED approach (individual objects so identified are indicated in Table 1). There are just four objects with light curves that are part of the standard set of members that are not already identified in the literature as YSO candidates; SSTYSV J032913.16+311949.4 and J032848.83+311753.7 are identified from IR colors, and SSTYSV J032913.47+312440.7 and J032837.85+312525.3 are identified via this X-ray+Class III identification. None of these four are variable, and they are faint. Figure 6 shows that the identified members are clustered towards the central region of our observations. Since the X-ray data do not cover the entire cluster, Class III objects can only be identified in the central region. Even without these members selected via X-rays, however, the IR-selected members are still clearly clumped towards the central region. Gutermuth et al. (2008) identified a main cluster with subclusters within it; these are indicated in Figure 6. Note that our formal definition of standard members does not require a light curve, and as such there are members indicated in Fig. 6 outside of the region with light curves. However, because the purpose of our present analysis is the time series data, we consider only those members with light curves for the rest of this paper.

There are 72 objects with YSOVAR light curves that are identified in the literature as confirmed or candidate YSOs (see R15), but that are not selected as candidate YSOs by our approach (see Fig. 6). Some of these objects are not selected by our approach because the object is undetected in X-rays and has no IR excess. It is more often the case, however, that the object is not identified from IR excess because it is missing at least one band; the G09 YSO selection mechanism requires a minimum signal-to-noise and a minimum number of bands for classification, and objects missing bands thus show up as 'unclassifiable' in the G09 approach. These literature members are not predominantly bright nor faint; they are scattered through the distribution of brightnesses in [3.6], though because of the overall shape of the distribution of sources (see Fig. 2), they represent a higher fraction of the brighter sources than the fainter sources. They are, however, often near bright sources such that measurements in some bands are difficult (or even impossible) to obtain, which is almost certainly why the bands are missing in the first place. These literature-only members are also clustered, but there are more of them (than the standard members) slightly towards the south. These candidate members that are not part of the standard set of members (but that have light curves) are included in the 'augmented set of members' (Sec. 4.6).

4.6.   Augmented Members

As discussed in R14, we have made provisions for establishing an "augmented set of members" to encompass objects not selected via the standard membership approach, but identified as variable and/or as members in the literature. For NGC 1333, we believe that all the objects that we identify as variable over the YSOVAR campaign are likely members.

The 72 additional literature members are thus included in our augmented members, as well as the 12 objects identified as variable, but not part of the standard set of members. Seven of those are literature-identified members not in the standard set, and five are newly identified candidate members. Our augmented set of members is, at 207 objects, significantly larger than the standard set of members (130 objects).

The five newly identified candidate members do not stand out in properties; they have comparable ranges of brightness, light curve shapes, etc., to the set of more established members. However, as with a significant fraction of the sample, spectroscopy is required to establish membership.

4.7.   Contamination and Completeness

Ideally, we would like to be able to quantify the degree of contamination and completeness in our member sample. To do this authoritatively requires a substantial number of spectra of the objects identified as standard members to understand contamination, and spectra of other objects with similar colors to estimate completeness. This is beyond the scope of this work. However, we try to estimate the level of contamination (and completeness) in the membership.

Our standard set of members uses IR excess and X-rays to identify members, and nearly all the standard set of members are already identified in the literature as YSOs. However, the standard members, even those that have been previously identified as YSOs, are not necessarily spectroscopically confirmed members or even confirmed to be stellar. Since NGC 1333 is relatively close, the chances of foreground contamination are low, and NGC 1333's own cloud helps limit background contamination. However, likely sources of contamination include (but are not limited to) RSCVn or other variable binaries, and background asymptotic giant branch (AGB) stars that appear faint and dusty (IR-bright). Active galactic nuclei (AGN) are another possible contaminant, but most of these should have been removed by our member selection approach. Additionally, the X-ray data are limited to the central region, so there is no way of finding X-ray detected Class III objects in the outer reaches of the cluster (specifically in the YSOVAR single-band coverage region). This is an obvious incompleteness that could be remedied by additional X-ray observations over the larger region.

Unlike other YSOVAR clusters, there is copious literature identifying candidate members in NGC 1333, which is why we defined the standard set of members, so as to enable comparisons across clusters. However, our standard set of members in NGC 1333 has missed a substantial number of literature-identified sources. The literature has used X-rays and IR excess, but also color-color and color-magnitude diagrams with follow-up spectroscopy (for brown dwarfs), and clustering to find members; in the present paper, we can use variability to find still more members. This inhomogeneous selection can, at its best, achieve a complete inventory of members, but at its worst, introduce complicated biases into the sample.

The literature-identified members not in our standard set of members probably do not represent a large source of contamination per se, given the reasons why they are missing (§4.5). But the sheer numbers of literature-identified members not in our standard set of members suggests that our standard set of members is highly incomplete.

Because NGC 1333 is relatively close to us, we expect that the known members will be among the brighter sources in the region, and this is borne out by Fig. 2 – the standard members indeed dominate the bright sides of the histograms. The fainter sources are where we expect more contamination to be introduced, but this is greatly complicated by the high (and clumpy) extinction towards NGC 1333, making sources appear fainter than they are. There are no obvious indications of contamination in Fig. 2, such as large numbers of faint member candidates. This could, however, be a circular argument – the known members are bright because the cluster is close, but it is also the case that previous investigators identify the bright members first. New members are more likely to be fainter if the known objects are also the bright objects.

We also expect that the members will be clustered on the sky (e.g., Gutermuth et al. 2008), and Fig. 6 reflects that – both the standard members and the literature members are clustered on the sky in the same region identified by Gutermuth et al. (2008) as the main portion of the cluster. The variables follow the same overall clustering pattern; the variables from the fast cadence YSOVAR campaign are more tightly clustered than the CY variables. It is hard to assess the degree to which the variable selection approach affects the clustering of the selected variables; there are more variables in the region with 2-band coverage, but there are also more bonafide cluster members in that region. The YSOVAR campaign variables use many epochs of observation; in contrast, the CY variables depend on the reliability of the cryo-epoch point, so they seem more likely to be contaminated. There are more CY variables to the south of the main cluster than the fast cadence selection. However, the standard set of members and the literature members both also identify objects to the south of the main cluster region.

We can attempt to assess the degree of contamination by looking at color-color and color-magnitude diagrams (CMD). The optical catalog is strongly biased towards 'interesting' objects, as well as strongly biased towards the less embedded objects and affected by spatially variable A_V. Without spectral types to individually deredden the photometry, an optical CMD is not the best for this purpose. Figure 7 shows a NIR CMD for our sample compared to Pleiades members (Stauffer et al. 2007) (moved from 133 pc to 235 pc). The members and variables are generally bright and red, as expected. The objects with light curves that are unlikely members are generally faint, consistent with background stars or galaxies. There are no blue objects below the main sequence (MS), which would be foreground stars. This plot does not indicate that contamination is a substantial problem. There is likely strong reddening affecting many of the members, which we knew would be an issue. (The A_V vector as shown corresponds to A_V=6 mags, which is the value for the heart of the cluster in the large map shown in Ridge et al. 2006.) The variables not in the standard set of members are all between $J \sim 12$ and 20, and $J - K_s \sim 1$ and 4. They are well-integrated with the standard member distribution, consistent with those objects being likely members.

Figure 8 is a NIR color-color diagram with the standard set of members and variables (over the YSOVAR campaign) indicated. The standard members (and variables) are located in the expected location for YSOs. There are few sources below or even on the MS relation, suggesting at minimum that there is little foreground contamination. There are large numbers of objects but, somewhat surprisingly, relatively few variables or standard members near the classical T Tauri locus from Meyer et al. (1997); reddening is evidently pushing objects off the locus. There are many objects in a location consistent with substantial reddening of the MS. This could be suggestive of contamination. The most likely objects in the standard set of members to be reddened MS non-members would be the X-ray selected Class III SED objects, but the X-ray selected objects are reasonably well-distributed through the plot. There are very few standard members or variables in the upper left corner of the plot, which would also be suggestive of contamination. We conclude that this plot, as Fig. 7, suggests both that there is not substantial contamination, but also that there is substantial

reddening affecting some sources.

Figure 9 is an IRAC color-magnitude diagram for the sample with [3.6] and [8] detections from the cryo era. Nearly all the variables and standard members are bright, and most are red, consistent with the locations expected for YSOs. This plot, as for the NIR, does not suggest that contamination is a major issue. As a result of our mechanism for selection of standard members, the members with $[3.6]-[8]\sim0$ mag are nearly all selected on the basis of X-ray detection. Many – but not all – of the variables that are not also standard members are also faint in [3.6]. This is consistent with expectations that most of the members that are bright are already identified. Most of these new objects are brighter than $[3.6]\sim15.5$ mag; light curves fainter than ~16 mag are difficult to identify as variable. The one object fainter than $[3.6]\sim17$ mag is SSTYSV J032912.05+311305.8, and it has a SED such that $[4.5]\sim12$ mag, and it is identified as variable from the [4.5] light curve. It is identified in the literature as a YSO only by c2d. (We note that the object at this location has sometimes been matched to IRAS4b and SK3, but that identification is uncertain; we have matched IRAS4b and SK3 more securely to another source; see R15). The remaining variables that are not also standard members are in the photospheric locus near $[3.6]-[8]\sim0$ mag, but are not detected in X-rays.

The newly identified variable members will require spectroscopic observation to confirm (or refute) their membership. However, their properties suggest that they are well-integrated with the rest of the members (standard or augmented sets). Their light curves do not generally distinguish them from the other members; they blend in with the other likely members. (We note that SSTYSV J032911.86+312155.7 may be an exception – it is variable, and not a literature or standard member, but its light curve and for that matter SED are different from other objects; see discussion below in Sec. 6.1.)

Summarizing the major issues addressed in this section, to the degree that we can tell, contamination is not obviously a factor, though completeness is an issue. There are substantial numbers of YSOs identified in the literature not selected via our approach, but this is for the most part because at least 1 band that is needed for identification is missing. Contamination is most likely to be background sources, possibly AGN or AGB stars. The standard members are significantly brighter on average than the rest of the sample. The objects newly identified as members through variability share properties with the previously-identified members in every diagnostic we have used. Spectroscopy and possibly X-ray observations over a larger region will contribute to our understanding of contamination and completeness in this region. Many of the objects are subject to large and spatially variable A_V, which complicates such followup.
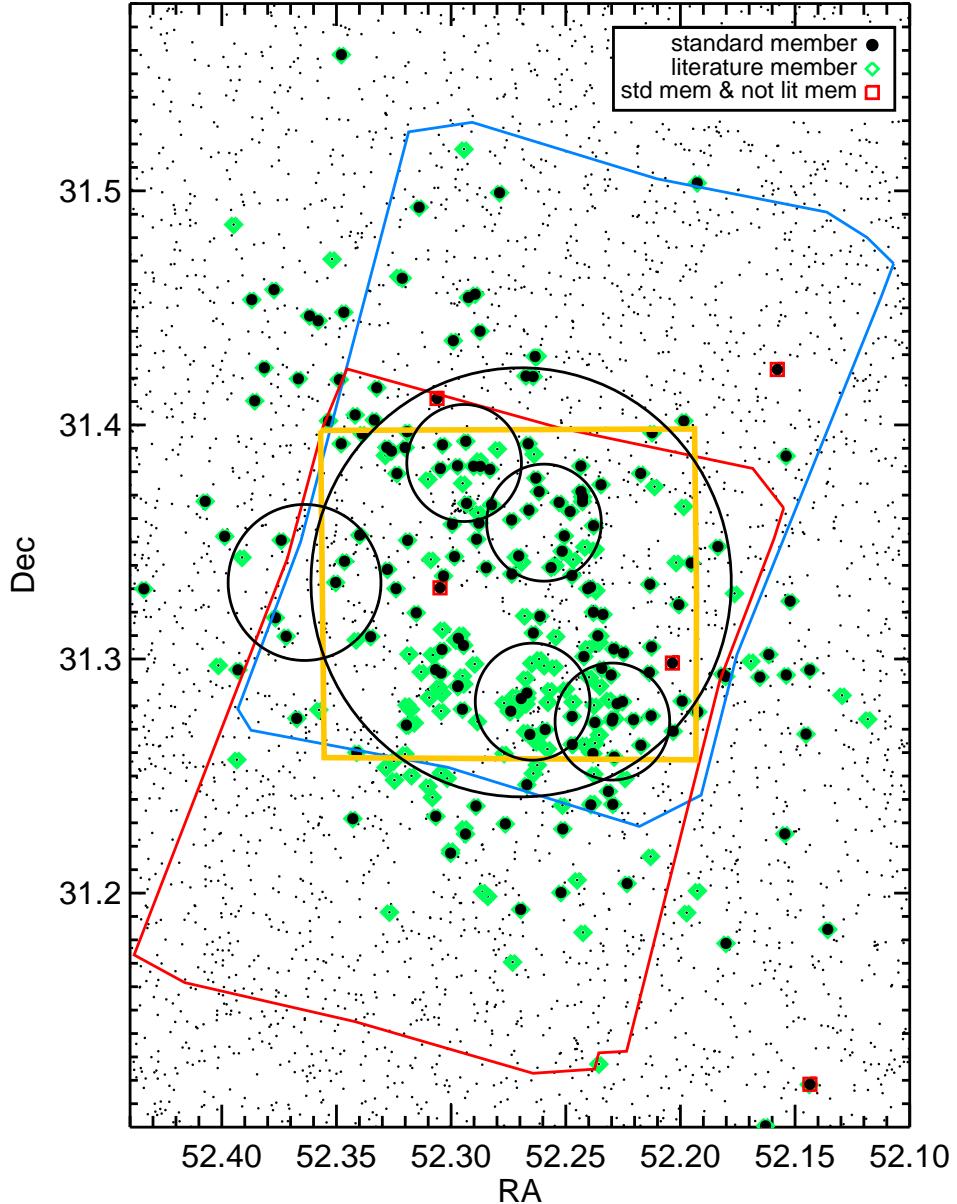
Fig. 6.— Locations of objects identified as members. Notation is similar to Figure 3, except now large black dots are objects identified as part of our 'standard set of members'; see text. Green diamonds are objects identified in the literature as confirmed or candidate NGC 1333 members. The five objects shown here as part of the standard set of members but not already identified in the literature as members have an additional red square (only four of them are in the region with light curves). The large black circles are the clusters identified in Gutermuth et al. (2009). Nearly all of the standard members are identified in the literature; there is a significant number of literature member objects not selected for the standard set of members. The literature-selected members are included in the augmented set of members. Member objects (of either type) are clustered towards the center of the observed region.
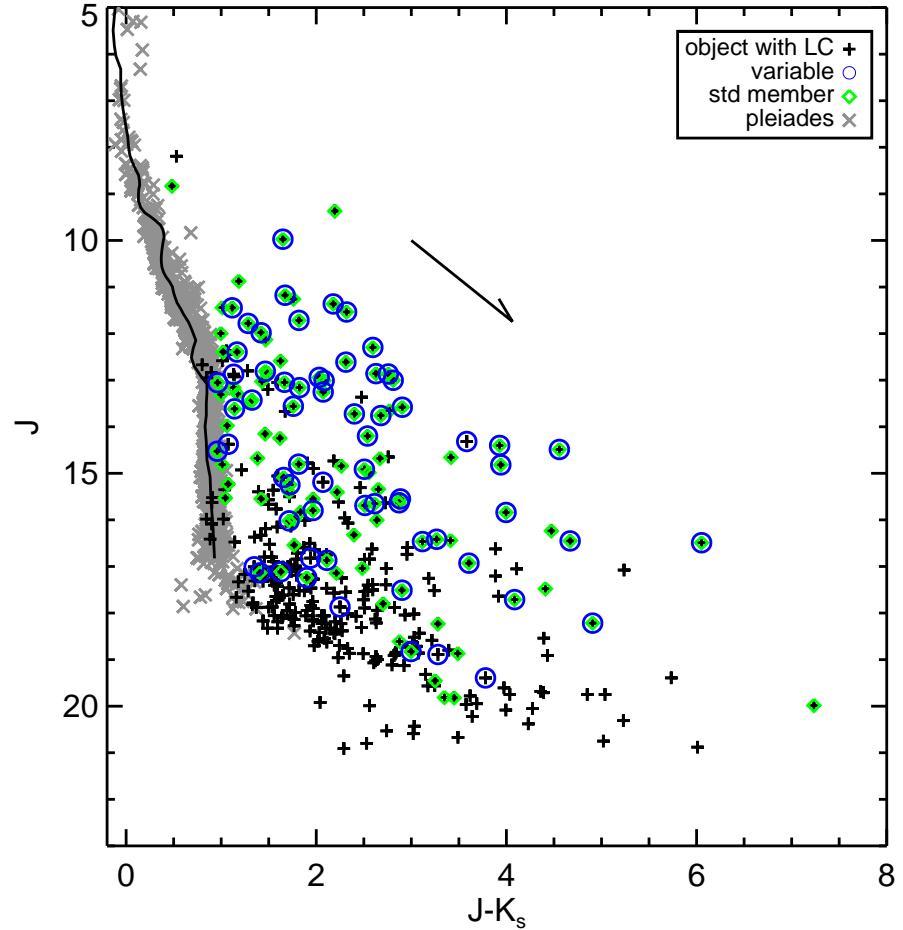
Fig. 7.— J vs. $J - K_s$ for the sample. Crosses are objects that have light curves; an additional blue circle indicates that it was identified as a variable over the YSOVAR campaign, and an additional green diamond indicates that it is in the standard set of members. Grey $\times$ symbols are Pleiades members (moved from 133 pc to 235 pc), and the black line is the expected main sequence (at 235 pc). The arrow corresponds to A_V=6 mag. This plot does not suggest substantial contamination of the members or variables by non-members. The variables that are not a priori selected as members are well- integrated with the distribution of the rest of the members.
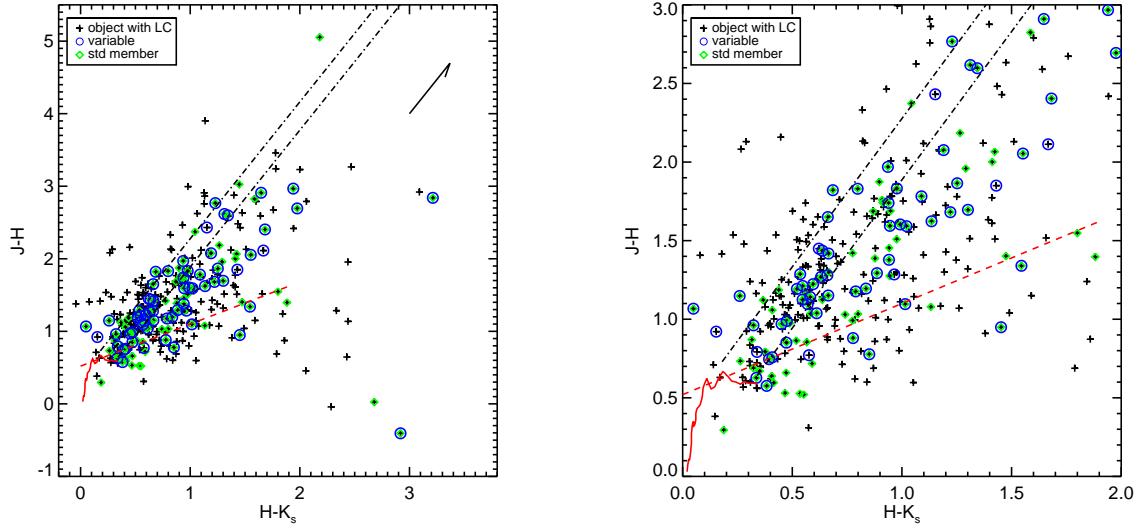
Fig. 8.— $J - H$, $H - K_s$ for objects with light curves in the catalog, with variables and the standard set of members indicated as shown. (The right panel is a zoom-in on the densest region from the left.) The red solid line is the expected ZAMS location; the red dashed line is the classical T Tauri locus from Meyer et al. (1997). A reddening vector for A_V=6 is shown; the black dot-dash line are extensions of the ZAMS according to this reddening law. This plot suggests that there is not a large contamination rate from foreground/background sources; see text.
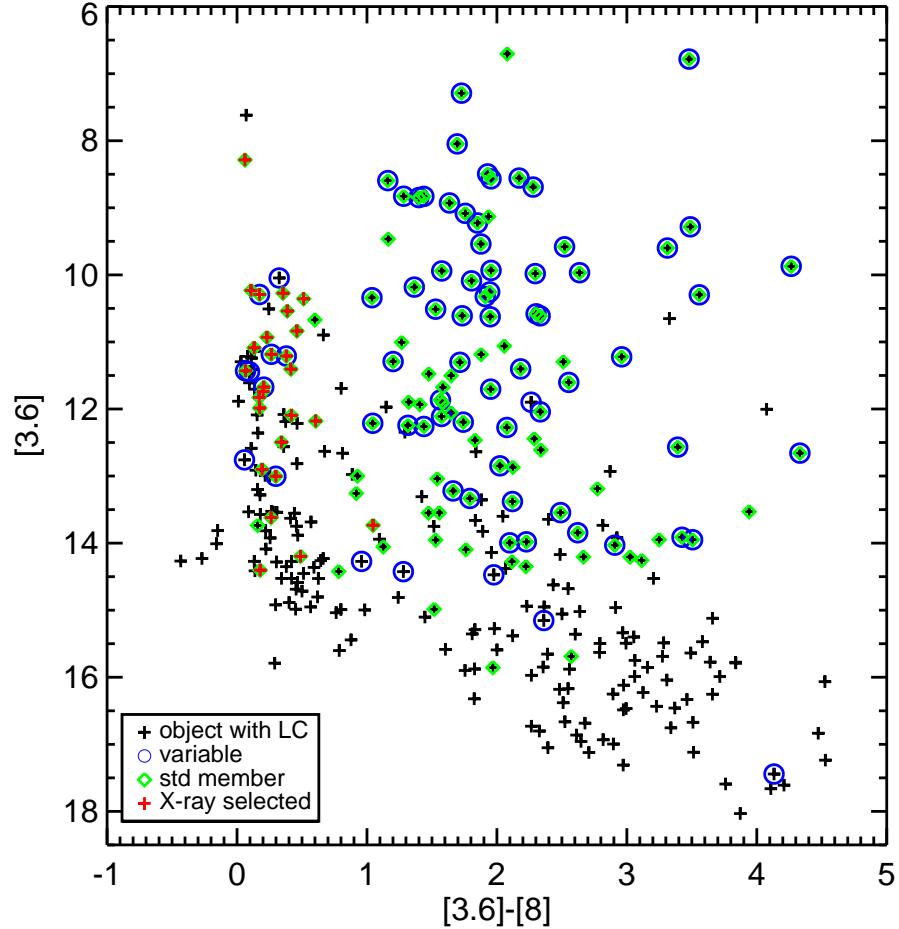
Fig. 9.— [3.6] vs. [3.6]−[8] for objects with light curves in the catalog, with variables and the standard set of members indicated as shown. An overplotted red cross is a standard member selected from X-ray detection and Class III SED shape. A reddening vector corresponding to $A_V \sim 6$ is comparable to the symbol size here, so is not shown. This plot also suggests that contamination is not a major issue.

5. Variable Fractions and Other Fractions of Note

5.1. NGC 1333

Table 3 collects variability fractions, among other things, for NGC 1333. Errors in the table are calculated using the larger of either Poisson or the binomial statistics from the appendix in Burgasser et al. (2003).

We expect that the bonafide cluster members are more likely to be variable in the YSOVAR campaign than field stars, and that is borne out by the data. The standard set of members is about 20% of the entire set of objects for which we have light curves. While ∼11% of all the light curves are variable, we find that about half, ∼52%, of the standard set of members are variable over the YSOVAR campaign. We also expect that a higher fraction of the disked YSOs with disks will be variable (compared to all YSOs), and we find this; ∼62% of the disked standard members are variable in the MIR.

In Sec. 4.7 above, we argued that contamination in the standard set of members is likely not substantial, but we should also consider the 'missing' members that appear in the literature but not in our standard set of members. Among the augmented member sample (including the literature-identified members and new variable members), the variable fraction is lower than that for the standard members, just ∼38%. Only ∼10% of these literature-identified members not included in our standard set of members are variable in the YSOVAR campaign. A higher fraction, 47%, of the disked augmented members are variable, but it is still lower than the analogous number for the standard members. Since we have a baseline expectation that YSOs will be variable, this is surprising, and is perhaps suggestive of a high contamination rate among these literature-identified members.

We considered whether we have properly identified all of the variables. R14 discussed the variability detection limits, so we do not repeat it here. In R14, we set conservative bounds on the χ^2 limits for variablity in the hopes that we would only include high-confidence variables (at the expense of likely missing some lower-level legitimate variables). In cases where we have light curves in 2 bands, and the Stetson index identifies a variable, the likelihood that it is really a variable is higher than if we have only one band and can only identify the object as variable based on the χ^2. In NGC 1333, we have some hope that the use of the χ^2 metric for selecting variables is indeed not unduly polluting the variables. Over the entire set of light curves, the variable fraction using the Stetson metric is larger by about a factor of two than the fraction based on χ^2. Among the standard set of members, the fractions are all reasonably comparable. This suggests that we are not adding many false variables by relying on χ^2 to find some variables. However, we have no easy way of assessing how many variables we may be missing.

Another possible influence on our standard set of members is the use of X-rays to identify members. We do not have complete X-ray coverage; only 13% of the objects with light curves have aX-ray counterparts. However, in part because of our mechanism for defining variables, but also in part because young stars are brighter in X-rays than older stars, 54% of the standard set of members have an X-ray counterpart. Of the 70 with a calculated log L_x, almost 60% are variable over the YSOVAR campaign. As discussed above, we also checked for variability in X-rays using the GL-vary metric; just 18% of standard members with light curves are variable in YSOVAR and also variable in X-rays. The length of the monitoring campaigns is very different between the IR and X-ray observations, admittedly. But the different variability fractions are consistent with the origin of IR variability being very different from the origin of X-ray variability (see, e.g., Flaherty et al. 2014).

Table 3. Variable fractions and other fractions of note

Category	All objects[a]	Std. members[a]	Aug. members[a]
Detections and Members			
Light curve exists at [3.6]	$436/701 = 0.62 \pm 0.04$	$116/130 = 0.89 \pm 0.11$	$168/207 = 0.81 \pm 0.08$
Light curve exists at [4.5]	$507/701 = 0.72 \pm 0.04$	$112/130 = 0.86 \pm 0.11$	$179/207 = 0.86 \pm 0.09$
Light curve exists at [3.6] & [4.5]	$242/701 = 0.35 \pm 0.03$	$98/130 = 0.75 \pm 0.10$	$140/207 = 0.68 \pm 0.07$
Standard members	$130/701 = 0.19 \pm 0.02$	$\cdots$	$130/207 = 0.63 \pm 0.07$
SED classes			
Object with Class I SED slope	$100/690 = 0.14 \pm 0.02$	$21/130 = 0.16^{+0.04}_{-0.03}$	$38/207 = 0.18 \pm 0.03$
Object with Flat SED slope	$82/690 = 0.12 \pm 0.01$	$22/130 = 0.17^{+0.04}_{-0.03}$	$30/207 = 0.14 \pm 0.03$
Object with Class II SED slope	$197/690 = 0.29 \pm 0.02$	$56/130 = 0.43 \pm 0.04$	$82/207 = 0.40 \pm 0.05$
Object with Class III SED slope	$311/690 = 0.45 \pm 0.03$	$31/130 = 0.24^{+0.04}_{-0.03}$	$57/207 = 0.28 \pm 0.04$
YSOVAR Variability			
Variable via Stetson	$56/236 = 0.24 \pm 0.04$	$51/98 = 0.52 \pm 0.09$	$56/138 = 0.41 \pm 0.06$
Variable via χ^2 at [3.6]	$53/436 = 0.12 \pm 0.02$	$50/116 = 0.43^{+0.05}_{-0.04}$	$54/168 = 0.32^{+0.04}_{-0.03}$
Variable via χ^2 at [4.5]	$57/507 = 0.11 \pm 0.02$	$52/112 = 0.46 \pm 0.05$	$57/179 = 0.32 \pm 0.05$
Periodic	$23/701 = 0.033 \pm 0.007$	$19/130 = 0.15^{+0.04}_{-0.03}$	$23/207 = 0.11 \pm 0.02$
Variable over YSOVAR campaign	$\mathbf{78/701 = 0.11 \pm 0.01}$	$\mathbf{66/130 = 0.51 \pm 0.08}$	$\mathbf{78/207 = 0.38 \pm 0.05}$
YSOVAR Variability and SED classes			
Variable (YSOVAR) object with Class I SED slope	$17/100 = 0.17^{+0.04}_{-0.03}$	$13/21 = 0.62^{+0.09}_{-0.11}$	$17/38 = 0.45 \pm 0.08$
Variable (YSOVAR) object with Flat SED slope	$19/82 = 0.23^{+0.05}_{-0.04}$	$16/22 = 0.73^{+0.07}_{-0.11}$	$19/30 = 0.63^{+0.08}_{-0.09}$
Variable (YSOVAR) object with Class II SED slope	$34/197 = 0.17 \pm 0.03$	$32/56 = 0.57^{+0.06}_{-0.07}$	$34/82 = 0.41^{+0.06}_{-0.05}$
Variable (YSOVAR) object with Class III SED slope	$8/311 = 0.026 \pm 0.009$	$5/31 = 0.16^{+0.07}_{-0.05}$	$8/57 = 0.14^{+0.06}_{-0.04}$
Variable (YSOVAR) Disked objects (I+F+II)	$\mathbf{70/379 = 0.18 \pm 0.02}$	$\mathbf{61/99 = 0.62 \pm 0.05}$	$\mathbf{70/150 = 0.47 \pm 0.04}$
Cryo-to-YSOVAR (CY) Variability			
CY variable	$92/701 = 0.13 \pm 0.01$	$35/130 = 0.27 \pm 0.04$	$48/207 = 0.23 \pm 0.04$
Variable over CY and YSOVAR campaign	$32/701 = 0.045 \pm 0.008$	$28/130 = 0.22^{+0.04}_{-0.03}$	$32/207 = 0.15 \pm 0.03$
YSOVAR and X-rays			
L_x and IR light curve exists	$89/701 = 0.13 \pm 0.01$	$70/130 = 0.54 \pm 0.04$	$79/207 = 0.38 \pm 0.05$
L_x and variable (YSOVAR)	$41/89 = 0.46 \pm 0.05$	$40/70 = 0.57 \pm 0.06$	$41/79 = 0.52 \pm 0.05$
GL-vary>7 and IR light curve exists[b]	$17/90 = 0.19^{+0.05}_{-0.04}$	$16/71 = 0.23^{+0.06}_{-0.04}$	$17/80 = 0.21^{+0.05}_{-0.04}$
GL-vary>7 and variable (YSOVAR)	$13/41 = 0.32^{+0.07}_{-0.06}$	$13/71 = 0.18^{+0.05}_{-0.03}$	$13/80 = 0.16^{+0.05}_{-0.03}$

[a]The last three columns consist of the numbers and fractions of objects in that category. Ex: 436 objects have a light curve at [3.6] out of 701 that have a light curve at any band, which is 62%; 116 objects out of 130 standard members have a light curve at [3.6], or 89%; 168 objects out of 207 augmented members (81%) have a light curve at [3.6].

[b]GL-vary can be calculated for 90 objects, but L_x can only be calculated for 89 objects.

As mentioned above and in R15, only some of the NGC 1333 members (standard or augmented) have spectroscopic follow-up, but perhaps we can gain insight into the variability fraction by considering a limited number of members. The most recent spectroscopic study is Foster et al. (2015), who observed in the NIR. Out of their sample, there are 150 members for which we also have light curves, and 67 (44±7%) are variable, an even lower fraction than among our standard members. However, the Foster et al. (2015) target selection was influenced by our variability work; perhaps it is biased. Arnold et al. (2012) reported on MIR spectroscopy from Spitzer, with targets selected based on MIR excess from Spitzer (Gutermuth et al. 2008; Winston et al. 2009, 2010), and is necessarily biased towards targets bright enough to be observed spectroscopically. There are 61 members identified in Arnold et al. (2012) for which we have light curves, and 45 (74±14%) are variable. This significantly higher fraction of variables could be a result of the bias towards brighter objects, and/or suggests that there very well could be contamination among our standard and augmented members. On the other hand, there is only one non-member identified in Arnold et al. (2012); we have a light curve for it, and it is not variable. None of the analysis above suggests a clear and obvious population of contaminants.

We note that there are substantial numbers of objects with light curves that are neither standard nor augmented members. For example, there are 98 objects with a Stetson index not suggestive of variability that are also not identified as members (standard or augmented). Eighteen of those objects also have an SED slope consistent with Class I objects. Especially if there is limited foreground/background contamination, what are these objects? Spectroscopy is warranted to identify these objects.

Perhaps a variability fraction between 50 and 75% is within expectations for young clusters. We now compare NGC 1333 to the other clusters that have been examined in detail in the context of YSOVAR.

5.2. NGC 1333 and Other YSOVAR Clusters

About half (52±8%) of the NGC 1333 standard set of members is variable in the MIR, and we want to compare this to other clusters. Morales-Calderón et al. (2011) found that ∼70% of Orion members are variable in the IR; Cody et al. (2014) find that 90% of NGC 2264 members (with disks) are variable. In both of these cases, these clusters are well-studied, with well-established sets of members, so the set of members (and even variables) is not selected in the same fashion as it is in NGC 1333.

For the smaller-field YSOVAR clusters, where we have defined the 'standard set of members' in the same way across clusters, four clusters besides NGC 1333 have been investigated in detail. Table 4 compares the same numbers for NGC 1333 and GGD 12-15 (Wolk et al. 2015), L1688 (Günther et al. 2014), IRAS 20050+2720 (Poppenhaeger et al. 2015), and Mon R2 (Hillenbrand et al. in prep). Fig. 10 presents some of the information from Table 4 in graphical form.

NGC 1333 has the lowest fraction of standard member variables among all 5 of these clusters. The mean across all clusters is within ∼1σ of the values for all of the other clusters; NGC 1333 is >1σ below this line. (We note, however, to the extent that NGC 1333 may be low, perhaps GGD 12-15 is high.) It is not clear why NGC 1333 should be different than the other clusters. NGC 1333 is considerably closer than all of those clusters except L1688, which affects the mass range to which we are sensitive; using the distances as reported in R14, NGC 1333 is at 235 pc, to be compared with Mon R2 at 830 pc, GGD 12-15 at 830 pc, IRAS 20050+2720 at 700 pc, and L1688 at 120 pc. In NGC 1333, we should be sensitive to considerably lower masses than all of those clusters except L1688, where we should be quite comparable. But, the member variability fraction in L1688 is much higher than in NGC 1333.

Table 4. Variable fractions across published YSOVAR clusters

Item	NGC 1333[a]	GGD 12-15[b]	L1688[c]	IRAS 20050+2720[d]	Mon R2[e]	Sum	
Standard Members	130	141	54	156	174	655	
Variable standard members	67	106	40	106	106	425	
Variable fraction	0.52±0.08	0.75±0.10	0.74±0.15	0.68±0.09	0.61±0.08	0.65±0.04	
Standard Members with 2-band LCs	98	122	37	109	89	455	
Stetson variable standard members with 2-band LCs	51	93	26	76	66	312	
Variable fraction	0.52±0.09	0.76±0.10	0.70±0.18	0.70±0.10	0.74±0.12	0.69±0.05	
Standard Members with 2-band LCs, Class I	13	18	11	34	20	96	
Standard Members with 2-band LCs, Class Flat	19	20	13	27	22	101	
Standard Members with 2-band LCs, Class II	46	57	10	38	35	186	
Standard Members with 2-band LCs, Class III	20	27	3	10	12	72	
Standard Members with 2-band LCs, Class III/total standard members with 2-band LCs	0.20±0.05	0.22±0.05	0.08±0.05	0.09±0.03	0.13±0.04	0.16±0.02	
Stetson Variable standard members with 2-band LCs, Class I	10	17	10	23	18	78	var frac I: 0.81±0.12
Stetson Variable standard members with 2-band LCs, Class Flat	14	19	10	23	16	82	var frac F: 0.81±0.12
Stetson Variable standard members with 2-band LCs, Class II	27	45	6	29	28	135	var frac II: 0.73±0.08
Stetson Variable standard members with 2-band LCs, Class III	0	12	0	1	4	17	var frac III: 0.24±0.06
Standard Members with 2-band LCs, disked	78	95	34	99	77	383	
Stetson Variable Members with 2-band LCs, disked	51	81	26	75	62	295	
Variable fraction	0.65±0.12	0.85±0.13	0.76±0.20	0.76±0.12	0.81±0.14	0.77±0.06	

[a]This work

[b]Wolk et al. (2015)

[c]Günther et al. (2014)

[d]Poppenhaeger et al. (2015)

[e]Hillenbrand et al. in prep.

Both NGC 1333 and L1688 contain known Class 0s, thought to be the youngest cluster members. Searches for Class 0s have only been conducted in nearby clusters, but nonetheless, given the available information, the YSOVAR campaigns in NGC 1333 and L1688 should include several of these youngest objects. Naively, then, since both of these clusters have several known Class 0s, one might expect similar variability fractions between these two clusters, but they are very different. However, when investigated in more detail, the relative number of Class 0s in these clusters is different, among other things, so perhaps differences are expected.

Some possible sources of contamination (see above and in R14 as well as Günther et al. 2014) are that it is easier to 'fool' the χ^2 variability test, and that X-ray data does not cover the whole field for which there are light curves (which affects identification of Class IIIs in the regions where there are no X-ray data). Therefore, we looked at subsamples designed to limit these influences. First, we selected variables solely using the Stetson index out of the standard set of members where there are light curves in both IRAC bands. The variability fractions for this sub-sample (see Tab. 4 and the second row of Fig. 10) are very similar to that for the overall standard set of members. With generally fewer stars involved, the errors increase, and most variability fractions increase slightly.

Secondly, Class IIIs are generally going to be the most difficult to identify reliably in these clusters. The most likely contaminant will be background/foreground stars (since galaxies are unlikely to have photosphere-like SEDs). YSOs seen through the NGC 1333 cloud though still belonging to Per OB 2 would appear as Class IIIs, though Per OB 2 members should be $\lesssim 6$ Myr (e.g., Bally et al. 2008), and therefore should also have IR excesses. Both NGC 1333 and GGD 12-15 have standard members with 2-band light curves that are composed of ∼20% Class IIIs, whereas the other clusters in Tab. 4 are closer to ∼10%. GGD 12-15 has by far the highest variability fraction among the Class IIIs. We then considered the variability fraction among just those standard members with 2-band light curves (and Stetson index to identify variables), but just for those that are Class I, flat, or II (see Tab. 4 and the third row of Fig. 10). All of the clusters are still roughly consistent with each other, but NGC 1333 is still slightly low, and now GGD 12-15 is slightly high.

Summing over all the clusters in Tab. 4, the (Stetson) variability fraction for Class I members with 2-band light curves is the same as that for Flat class members, 81±12%. The variability fraction for Class II objects is significantly lower at 73±8%, and the variability fraction for Class III, largely driven by the GGD 12-15 sources, is 24±6%. So our expectation that more embedded objects are more likely to be variable is met across all clusters, suggesting that most of the MIR variability arises from dust in the disk or from variable accretion from the disk to the star. (For the Class III sources, which should have little or no dust disk, the IR variability must be coming from the photosphere.)

To summarize, NGC 1333 may have legitimately a slightly lower fraction of variables. NGC 1333 may have some contamination in its standard set of members, although such contamination is not immediately apparent from the diagnostics above in Sec. 4.7. This could be random error, or it could be a sign of different environments in different clusters. More analysis of this is deferred until detailed analysis of each of the remaining YSOVAR clusters is complete.

6. Sizes of Brightness and Color Changes

In this section, we investigate the amplitude of brightness and color changes over the YSOVAR campaign, and identify some of the objects with the largest brightness changes in the CY variables.

6.1. Light Curve Amplitudes Over the YSOVAR Campaign

We define light curve amplitude over the YSOVAR campaign to be the difference between the 10th and 90th percentile in the distribution of points. This effectively omits flares or other few-epoch excursions, and is the same definition used in several other YSOVAR papers. Histograms of light curve amplitudes for both IRAC channels are shown in Figure 11. Distributions are shown for the entire standard set of members (variable or 'not detected as variable,' NDAV), as well as just the variable standard members. Some of the variable members have very low amplitudes, comparable in size to the NDAV objects; the distribution of amplitudes for all members likely includes some objects that are legitimately variable but not identified here. A few objects vary with amplitudes more than 0.2 mag, but a more typical amplitude for the variables is 0.1-0.15 mag.

Fig. 11 includes distribution functions for the entire standard set of members. Out of the variable members, at [3.6], 15/62 or 24($\pm$6)% vary at 0.2 mags or more, and at [4.5], 11/60 or 18($\pm$6)% vary at 0.2 mags or more. Out of the entire standard set of members, at [3.6], 17/116 or 14$\pm$3% vary at 0.2 mags or more, and at [4.5], 11/112 or 10$\pm$3% vary at 0.2 mags or more. About 65% of the variable members vary at 0.1 mags or more in either channel, $\sim$30-40% of the standard set of members vary at 0.1 mags or more in either channel, and $\sim$65% of the augmented set of members vary at 0.1 mags or more in either channel. Out of the entire set of variables (not just the standard set of members), $\sim$7% at either channel vary at amplitudes >0.4 mag.

Looking at the distributions of amplitudes for each SED class, the distribution of the amplitudes of Class I, Flat, and Class II objects are statistically indistinguishable. Figure 12 plots the amplitudes of the variables in [3.6] against [4.5], with color coding by class. There may be a very slight tendency for the Class I objects to have larger amplitudes on average. However, the mean amplitude in [3.6] or [4.5] (for all variables) for Class I, flat, and II are all $\sim$0.16 mag. So any tendency towards larger amplitudes in the more embedded SEDs must be subtle, or lost in low-number statistics. Class III objects are significantly different (in either IRAC channel); the mean for Class III variables is $\sim$0.03 mag, distinctly different from the rest of the distribution.

There are no discernible trends of amplitude of variation with effective temperature or spectral type, for those objects where we can look for such a correlation. Our sample is not large or long enough to determine the fraction of sources in a burst or elevated state (see, e.g., Hillenbrand & Findeisen 2015).

There are seven variables with amplitude >0.4 mag in either channel. They are listed in Table 5. They are nearly all literature-identified YSOs and part of our standard set of members. One object, SSTYSV J032911.86+312155.7, merits more discussion than can easily be fit in Table 5. It is not a literature YSO or a standard member set YSO. It has an unusual SED that is quite flat from J to 4.5 μm, admittedly with large errors, and the SED rises abruptly at 24 μm to more than an order of magnitude more energy density; see Figure 13. Under our scheme, it is an SED Class I. In the images, it is in a very messy region, with high surface brightness, which precludes a WISE detection. There is definitely a source at 24 μm, but whether all the flux should be assigned to this object is an open question. The SED does not particularly look like a YSO SED, but its location amongst other sources in a high surface brightness region is circumstantial evidence that it is a YSO. Foster et al. (2015) discard it as a non-member based on NIR spectroscopy, but looking at the spectrum, the NM assessment was based on low signal-to-noise, as opposed to high-quality radial velocity (RV) measurements that were inconsistent with membership. The formal RV is 25 $\pm$75 km s^{-1}, and is within 0.3 sigma of the cluster's velocity of $\sim$8 km s^{-1}, and the spectrum is dominated by sky lines (telluric and nebular). Thus, we conclude that the APOGEE spectrum is not of sufficient quality to

rule out this object as an NGC 1333 member. There is no X-ray detection from any instrument. Its light curve exists only at [4.5] and consists of a flat continuum with two large ($\sim$1 mag) flares (see Figure 13), where the flares are defined by several points (not just one per flare, which might suggest, e.g., cosmic rays). This is different from the other light curves in NGC 1333; this object is either an unusual young star, or a contaminant object.
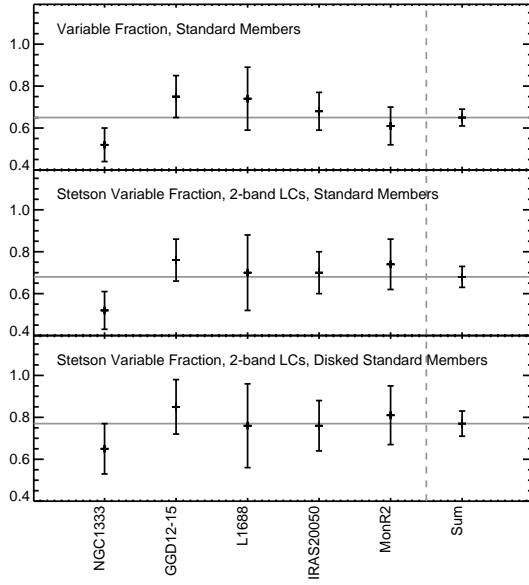
Fig. 10.— Variability fractions for several clusters (listed across the x-axis) for the standard set of members (first row), just those that have light curves in 2 bands and are identified as variable from the Stetson index (middle row), those that are Stetson-variable among the 2-band light curves for standard members with disks (Class I, Flat, and II). The last column sums up all of the corresponding data across these five clusters. The horizonal grey line corresponds to the value from this sum across clusters. Error bars are calculated assuming Poisson statistics. NGC 1333 has a slightly lower variability fraction than most of the other clusters, but GGD 12-15 has a slightly higher variability fraction than most of the other clusters.
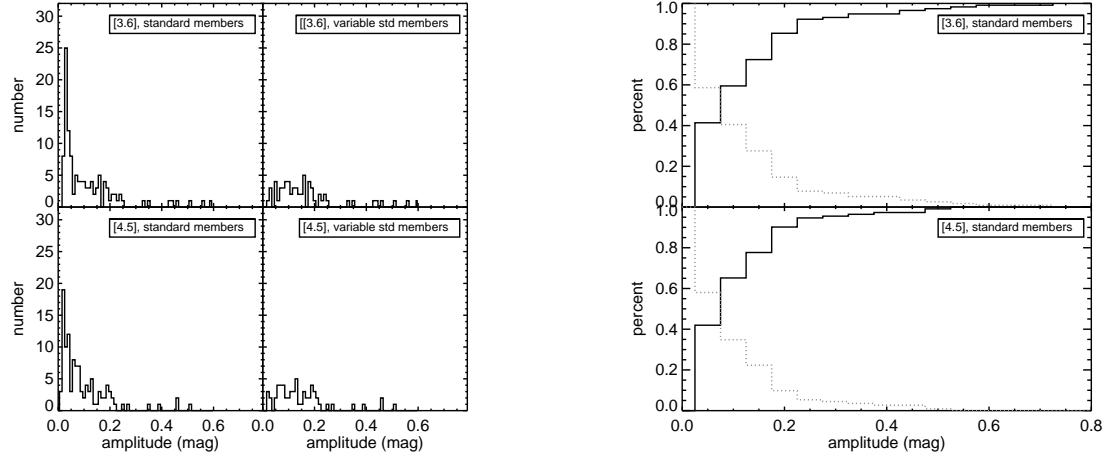
Fig. 11.— LEFT SIDE: Histogram of the amplitudes of the light curves. Upper left: [3.6] light curves, for standard set of members; upper right: [3.6] light curves, for all variable (standard) members; lower left: [4.5] light curves, for standard set of members; lower right, [4.5] light curves, for all variable (standard) members. RIGHT SIDE: Cumulative distributions (in both directions of increasing and decreasing magnitudes – black solid and grey dotted lines) for [3.6] (top) and [4.5] (bottom), standard set of members (variable and non-variable). About 20% of the variable members vary at 0.2 mags or more; about 10% of the standard set of members vary at 0.2 mags or more.

Table 5.   Large-amplitude variables

SSTYSV	sample	Notes
032847.63+312406.1	YSOVAR 1-band	Identified in literature as YSO, std member. SED Class II. [3.6] only, but light curve much like other YSOs. Deep dip.
032851.01+311818.5	YSOVAR 2-band	>0.4 mag in both channels. Identified in literature as YSO, std member. SED Class II. Light curve shaped as almost a step up.
032859.54+312146.7	YSOVAR 2-band	>0.4 mag in both channels. Identified in literature as YSO, std member. SED Class II. Large-amplitude color variability (nearly 0.1 mags) entirely consistent with reddening.
032903.13+312238.1	YSOVAR 2-band	>0.35 mag in both channels. Identified in literature as YSO, std member. SED Class II. Periodic with an overall trend down.
032908.97+312624.0	YSOVAR 1-band	Identified in literature as YSO, std member. SED class Flat. [3.6] only, but light curve much like other YSOs. Deep dip.
032909.32+312104.1	YSOVAR 2-band	>0.4 mag in both channels. Identified in literature as YSO, std member. SED Class Flat. Broad, sharply peaked 'burst'.
032911.86+312155.7	YSOVAR 1-band	Not lit YSO or std member. [4.5] only. See text.
032904.31+311906.3	YSOVAR color	>0.2 mag color change as part of large dip in light curve. Identified in literature as YSO, not std member. SED Class Flat.
032910.70+311820.9	CY var	~2 mag change between cryo and YSOVAR. SED class I (but identified in literature as an SED class 0). Reddened SED. YSOVAR campaign itself relatively unremarkable.
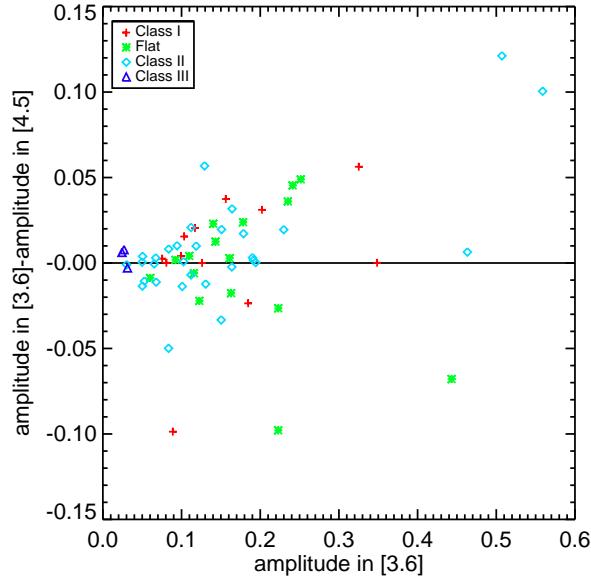
Fig. 12.— Amplitude in [3.6] against the difference of amplitude in [3.6] − that in [4.5] for the all of the variables that have data in both channels. Colored symbols correspond to SED classes: red plus = Class I, green asterisk = Flat, cyan diamond = Class II, dark blue triangle = Class III. The amplitudes found for the Class III objects are smaller than most of the rest of the amplitudes. The distributions of amplitudes for the rest of the classes are statistically indistinguishable, though there may be a slight tendency for the Class I objects to have larger amplitudes on average. The solid line is the line along which the points would fall if the amplitudes in both bands were identical. The points are symmetrically distributed about that line.
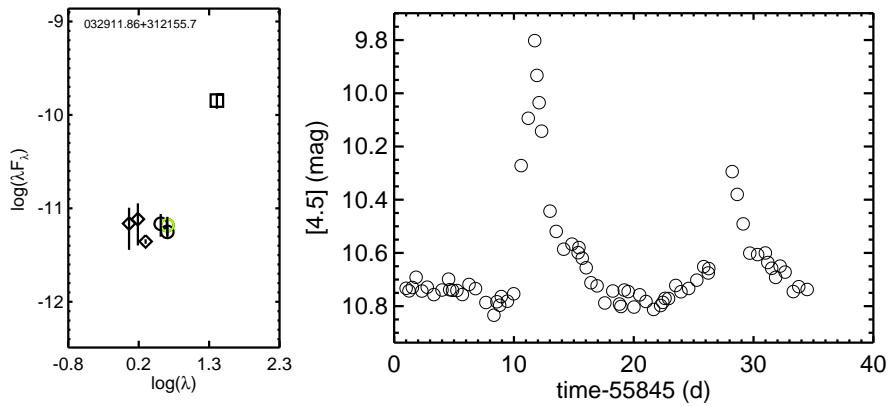
Fig. 13.— SED and light curve for source SSTYSV J032911.86+312155.7 (=LAL244=MBO81=Foster 140). In the SED, $\log \lambda F_\lambda$ is plotted with λF_λ in cgs units (erg s^{-1} cm^{-2}) and $\log \lambda$ is plotted with λ in microns. Diamonds are 2MASS, circles are IRAC (with the green being from the YSOVAR campaign), and square is MIPS. Vertical black lines are error bars (or amplitude of YSOVAR campaign in the case of the green IRAC point, where amplitude is defined as in the text). This source may not be a YSO; see discussion in text.

6.2. Color Amplitudes Over the YSOVAR Campaign

Figure 14 shows the distribution of the amplitude (10th to the 90th percentile of the distribution) for $[3.6]-[4.5]$ for the variables with light curves in both channels. The distribution of color changes peaks at ~ 0.05 mag. Figure 14 also shows the amplitude of $[3.6]-[4.5]$ against the amplitude in $[3.6]$. Larger color changes generally (although not always) also translate to larger single-band changes. There are no discernible trends of amplitude of color change with effective temperature.

The most extreme color change is >0.2 mag change; see Figure 15. It is SSTYSV J032904.31+311906.3 and is not part of the standard set of members. Few papers in the literature identify it as a member, but Aspin et al. (1994) does (it is ASR 61). The G09 identification process classifies it as a broad-line AGN. Its SED looks stellar (see Fig. 15); spectroscopy is needed. Early in the YSOVAR campaign, the trend in the CMD is along an overall slope consistent with that expected from reddening; this can be seen in the CMD as the black through blue points. Then, as the lightcurve takes an overall dip (which is at its lowest at ~ 28 d), the object becomes, on the whole, bluer and fainter. No obvious image artifacts are responsible for this dip. The smaller amplitude and timescale variations, on their own, move in a direction in the CMD very roughly consistent with a reddening slope. But the larger amplitude and larger timescale motions are different. The shorter timescale variations would require A_V variations of $\sim$10-15 mag (in the optical), whereas the longer timescale variation would require ~ 30 mag (in the optical). This is not physically impossible, just somewhat unexpected. The disk around this object does not dominate the SED, though it is clearly a substantial disk; large amounts of obscuring dust might be expected if the dust dominated the SED. If variations in the inner disk, close to the star, account for the structure changes on shorter timescales (moving in the general direction consistent with reddening), and if the star is viewed close to edge on, such that structures in the outer disk occult the line of sight by different amounts on timescales of weeks to months, then this object may be seen mostly in scattered light as it becomes fainter, which could cause the overall bluer-when-fainter behavior.
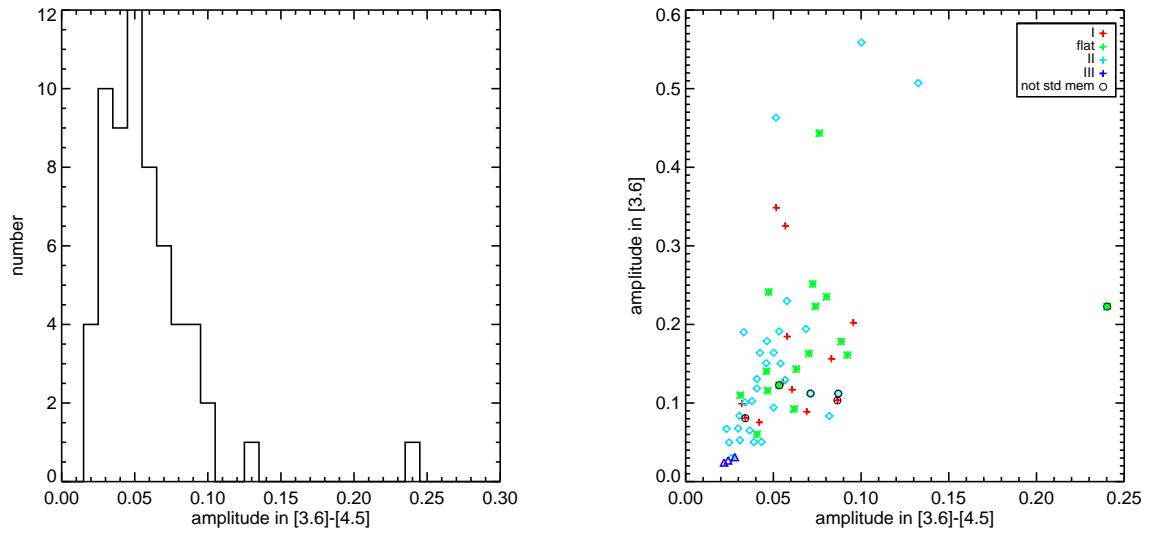
Fig. 14.— These plots include all variables with light curves in both channels. LEFT: distribution of the amplitude of [3.6]−[4.5], which peaks at ∼0.05 mag. There are some extreme color variables, but most have small changes in color. RIGHT: amplitude of [3.6]−[4.5] against the amplitude in [3.6], both in magnitudes. Colored symbols correspond to SED classes: red plus is Class I, green asterisk is Flat, cyan diamond is Class II, dark blue triangle is Class III. An additional circle means that the variable is NOT in the standard set of members – most of the variables are in the standard set of members. Typically, the largest single-band amplitudes are accompanied by the largest color amplitudes, but there is a lot of scatter.
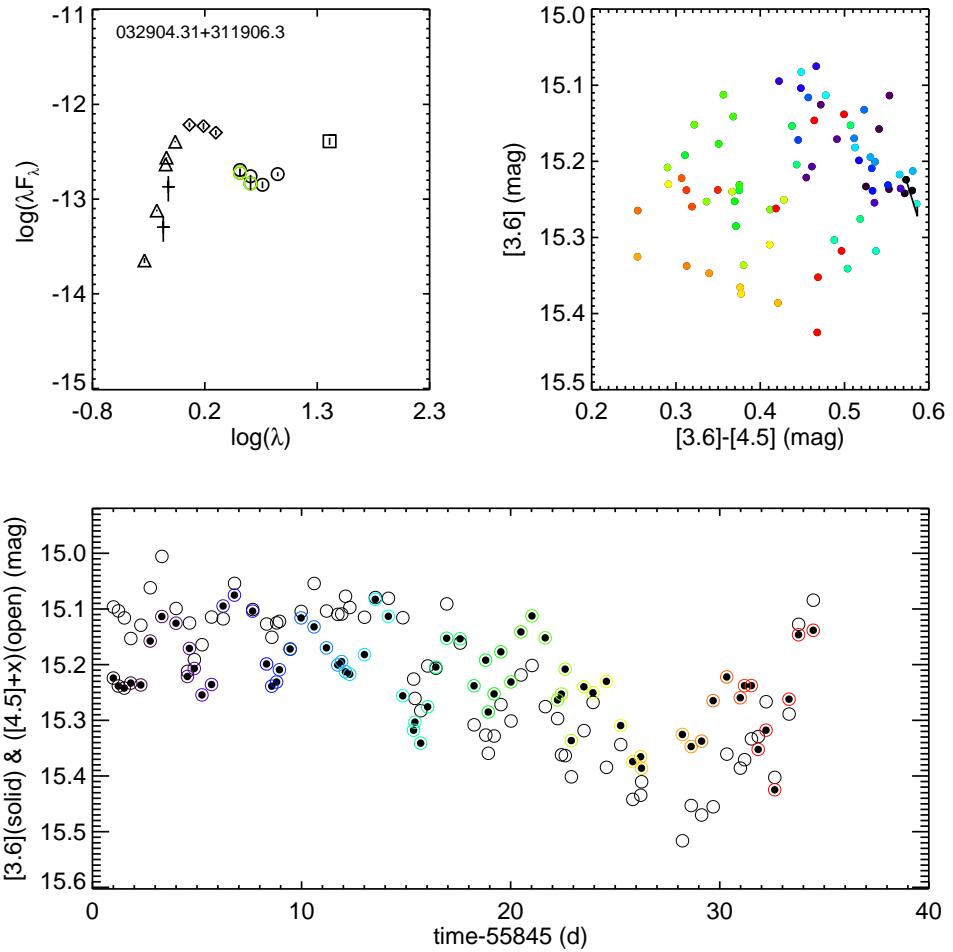
Fig. 15.— SED, CMD, and light curve for source SSTYSV 032904.31+311906.3 (=ASR61=MBO156=Foster 100, an M0-3 spectral type). In the SED, $\log \lambda F_\lambda$ is plotted with λF_λ in cgs units (erg s^{-1} cm^{-2}) and $\log \lambda$ is plotted with λ in microns. Triangles and crosses are optical data, diamonds are 2MASS, circles are IRAC (with the green being from the YSOVAR campaign), and square is MIPS. Vertical black lines are error bars (or amplitude of YSOVAR campaign in the case of the green IRAC points, where amplitude is defined as in the text). The CMD is in the upper right, with colored points corresponding to the circled epochs in the bottom light curve (that is, black/purple points are from early in the campaign, and orange/red points are from late in the campaign). There is an A_V=1 vector shown from the first point in the campaign. In the light curve on the bottom, solid points are [3.6], and open black circles are [4.5], shifted (represented by '+x') such that the mean [4.5] matches the mean [3.6]. The additional colored circles correspond to the colors used in the CMD. This source exhibits the largest color change in the entire YSOVAR dataset; see discussion in text.

6.3. The Largest CY Variables

R14 looked for objects whose color appeared to change significantly, specifically looking for objects that appeared to have transient IR excesses (e.g., color appearing or vanishing between the cryo epoch and the YSOVAR epochs; see, e.g., Meng et al. 2012, Melis et al. 2012, Rice, Wolk, & Aspin 2012) One object from NGC 1333 was so identified: SSTYSV 032910.70+311820.9, shown in Figure 16.
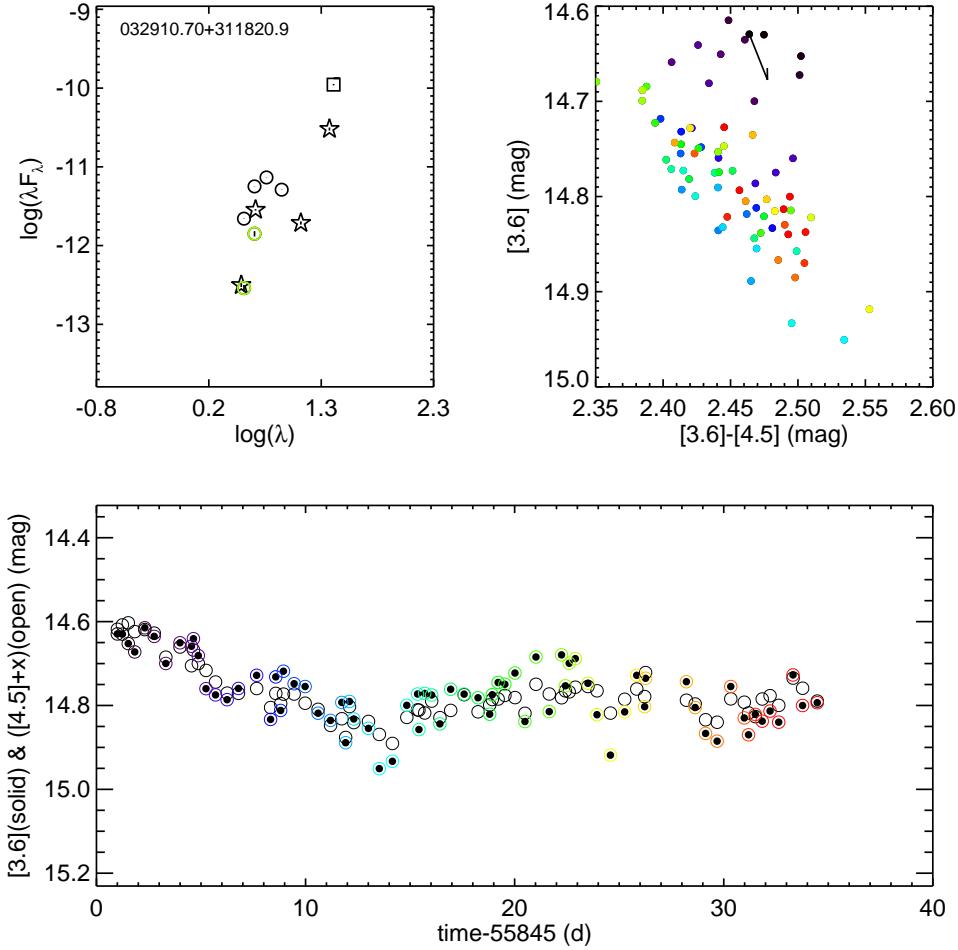
Fig. 16.— SED, CMD, and light curve for source SSTYSV 032910.70+311820.9 (=J07-23=Gutermuth 35). Notation is as in prior figure, except stars in the SED are WISE data. This source exhibits the largest CY change in the entire YSOVAR dataset; see discussion in text. It is also thought to be a jet driver; see Sec. 10.1.

SSTYSV J032910.70+311820.9 has an ususual SED in comparison to other objects with light curves here - it appears to be heavily reddened, with the peak of the SED shorter than 15 μm appearing at 5.8 μm (most other sources peak in the near-IR). The 24 μm point rises very abruptly to have an order of magnitude more energy than the 5.8 μm point. The WISE data are further confusing; by inspection of the images, the AllSky (rather than AllWISE) catalog seems to do a better job of characterizing the flux

from this object (R15). The flux density at 22 μm is lower than that measured at 24 μm; the 12 μm point appears to be falling roughly on a Rayleigh-Jeans line from the 8 μm point, resulting in a very abrupt rise from 12 to $\sim$20 μm. It may be that 100% of the flux density at 22 and 24 μm should not be associated with this point source, though the source is bright ([24]=2.27, [22]=3.9) and point-like at these bands, and sufficiently separated from another comparably bright source $\gtrsim$10$''$ away (SSTYSV J032911.24+311831.8, which appears in Fig. 29 below). The IRAC images suggest that there may be some nearby nebulosity. It is a SED Class I. The mean 3.6 and 4.5 μm points from our campaign are very different than the cryo-era measurements – in the cryo era, $[3.6] - [4.5] = 12.57 - 10.82 = 1.75$, while the YSOVAR means are $< [3.6] > - < [4.5] >= 14.77 - 12.32 = 2.45$. The two WISE measurements at 3.4 and 4.6 μm were obtained at a mean epoch in time between the cryo and YSOVAR epochs, and they fall between these points in the SED ([3.4]=14.84, [4.6]=11.49), lending credence to this variation despite its unusual amplitude of $\sim$2 mag in each IRAC channel between the cryo and YSOVAR epochs ($\Delta[3.6] = 2.2$, $\Delta[4.5] = 1.5$). However, the light curve over the YSOVAR campaign itself is relatively unremarkable; see Fig. 16. It is, at least, identified as variable from the Stetson index and both χ^2 values. The total peak-to-peak variation is $\sim$0.3 mag, and the amplitude as defined above is $\sim$0.2 mag; it has a standard deviation σ of 0.075 mag and a median absolute deviation (MAD) of 0.060 mag in [3.6] and, for [4.5], σ=0.063 mag and MAD=0.044 mag. Over the YSOVAR campaign, the MAD $[3.6]-[4.5]$ color is 0.03 mag, so it is not a large color change, as can be seen in Fig. 16. Given the observed variability in the YSOVAR campaign, one would not necessarily have selected this object as a likely large amplitude variable on timescales of years, but it nonetheless appears to have a very significant variation on those timescales. This source is identified in the literature as a jet driver (see Sec. 10.1), which is consistent with it being very embedded.

Three other objects were identified as potential large-amplitude CY variables in NGC 1333, but none of them were also identified as variable over the YSOVAR campaign. For all three of them, we have reason to question the size of the change between the cryo era and the YSOVAR campaign.

SSTYSV J032855.72+311442.1 is clearly detected in the YSOVAR epochs, but is close to (possibly technically part of) IRAS 2A, which is a very bright source. It has been matched, perhaps incorrectly, to sources with a measured flux density at 8 and 24 μm that result in a very steep SED (nearly monotonically increasing, slope of $\sim$3). The YSOVAR light curve is not detected as variable, though viable data really only exist at 4.5 μm (there are a few epochs at 3.6 μm near the end of the campaign). There are indeed large differences between the cryo-era measurements ([3.6]=16.09, [4.5]=14.51) and the mean YSOVAR value ($< [3.6] >$=15.69, $< [4.5] >$=13.4). However, the measured brightness is likely affected by the nearby nebulosity and point sources, and moreover is near the faint limit at [3.6], beyond which light curves become very noisy. We suspect that the apparent changes between the cryo and YSOVAR eras are spurious.

SSTYSV J032858.78+312044.9 has a reasonably well-defined SED over the IRAC bands, despite having image morphology suggestive of a nebulous clump. However, while the 3.6 μm point between cryo and the YSOVAR campaign is a fairly good match, the 4.5 μm cryo-era point is inconsistent (by about half a dex) with the rest of the SED; the measurement in our database was obtained from the c2d catalog and has a large error bar. This object is also not identified as variable over the YSOVAR campaign. Since the cryo-era measurement at 4.5 μm is evidently unphysical, we remove this object from the list of objects with large changes on timescales of years.

SSTYSV J032918.88+312313.0 has a strange SED, which is not monotonically increasing but includes a 24 μm point at $\sim$0.5 dex more energy in the SED than the peak at 4.5 μm. The mean [4.5] from the YSOVAR campaign is well-matched to the cryo-era measurement; however, the mean [3.6] from the YSOVAR campaign (15.02) is significantly different than the cryo-era [3.6] (15.85). It is in a region of very high surface

brightness, so as a result of the high background, 15th magnitude is probably close to the detection limit, and may be a nebulous clump. We strongly suspect that either the cryo-era [3.6] or the mean from the YSOVAR campaign is incorrect, and thus we also remove this object from the list of objects with large changes on timescales of years.

Out of all 242 objects (not just members) with light curves in both bands, then, we have at most 1 object that has legitimate very large changes at 3.6 and 4.5 μm over timescales of mulitple years, or at most a $\sim$0.4% rate of occurrence. (By collecting objects over all YSOVAR clusters, R14 estimated a rate of at most $\sim$0.02%.)

7. Timescales of Variability

7.1. Overview

Characterizing the timescales of the YSOs in our sample is important for tying the variations we see to physical properties in the star-disk system. For example, we expect very short timescale variability to be related to events on or near the surface of the star, and longer timescale variability to be related to changes further out in the disk. However, characterizing the diversity of YSOVAR lightcurves with a single timescale has proven challenging.

There are several different ways in which we could define timescales of the variability seen in our light curves. Each of the methods we considered has advantages and disadvantages, and in all cases we considered, we could find light curves (often many of them) for which the timescale by eye did not match the numbers resulting from a given approach. Determining the 'best' timescale to use is beyond the scope of this paper (see, e.g., Findeisen et al. 2015).

In other YSOVAR papers, timescales related to the autocorrelation function (ACF) have been used. Using the ACF requires evenly spaced times. We linearly interpolated the light curve onto evenly spaced times, and then calculated the ACF using the following expression where L is a lag in days, and x is the light curve (with elements x_k):

$$ACF_x(L) = ACF_x(-L) = \frac{\sum\limits_{k=0}^{N-L-1} (x_k - \overline{x})(x_{k+L} - \overline{x})}{\sum\limits_{k=0}^{N-1} (x_k - \overline{x})^2} \tag{3}$$

McQuillan et al. (2013) and Cody et al. (2014) used an approach where they selected the larger of the first two local maxima in the ACF to determine the period of the light curve. For those objects with signficant periods, this timescale is well-matched to the period. For objects without significant periods, this value seems to give an indication of the timescale found in the light curve; it is often well-matched to the variations we see by eye. This calculation can fail, however, if the ACF is not well-behaved. Where the ACF is well-behaved, we use this timescale here. Sec. 7.2 characterizes the timescale distribution, and Sec. 7.3 discusses relationships between timescales, amplitudes, and SED classes.

For periodic objects, the timescale is perhaps the best defined in theory. In practice, though, for the objects that we determine to be periodic, sometimes there are variations in addition to the period (on shorter and/or longer timescales) that call into question whether the period is actually the dominant timescale. The period, however, is well-matched in most cases to the timescale derived from the ACF above. The periodic

objects in NGC 1333 are discussed in Sec. 7.4.

7.2. Characterizing Overall Timescales

Figure 17 has histograms and distributions of the timescales for the variable standard members in NGC 1333. There are 55 variable members with measured timescales in either (or both) of the bands. The timescales are typically reasonably short, with medians near 6.5 days, but a mode (most frequent value) near 4.5 days. Note that this is just the standard members – there are 7 more mid-IR variable objects that are not part of the standard set of members, so addition of those objects does not appreciably change Figure 17. We cannot characterize the distributions of timescales for objects not considered to be members (as distinct from members) because there are just too few of them.
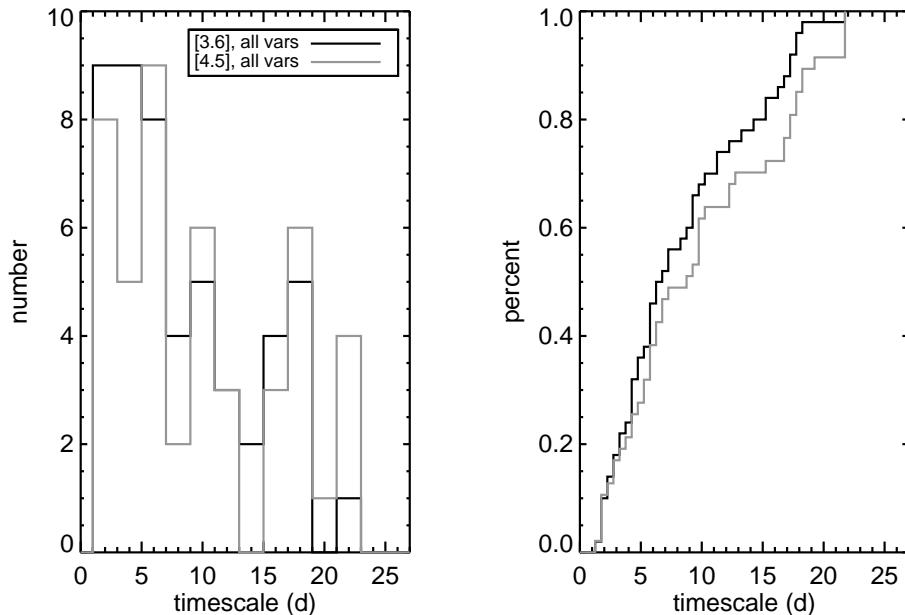
Fig. 17.— Timescales for variable standard member objects. Black line is [3.6], and grey line is [4.5]. Left is histograms of values, right is the distribution functions. The timescales are typically short, on the order of a few days.

For those cases where light curves exist in both channels, we can compare the timescales obtained from both channels. We expect that the two IRAC channels should be well-correlated, so we expect that the timescales so derived will be similar. Figure 18 compares the timescales derived for the two channels. They are, indeed, well-matched for most objects. The lightcurves where they do not match are typically very complex.
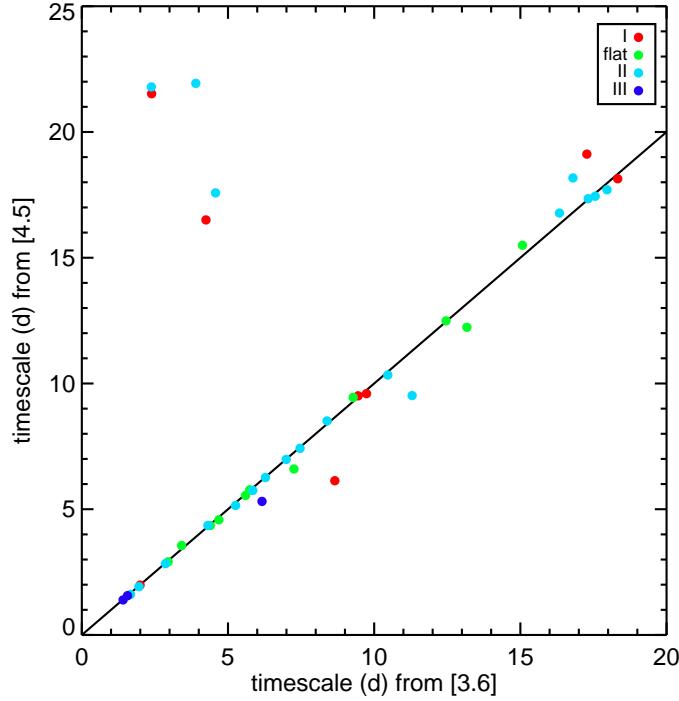
Fig. 18.— Comparison of the timescales derived from the two channels for all variable standard member objects. The colors of the points correspond to the SED class as shown. The timescales derived from the two channels are generally well-matched to each other.

7.3.   Timescales, Amplitudes, and SED Class

Günther et al. (2014), Poppenhaeger et al. (2015), and Wolk et al. (2015) all found longer timescales for steeper (positive) SED slopes, that is, that Class I objects had on average longer timescales than Flat class objects, which was longer than Class II, which was longer than Class III. For NGC 1333, among the standard set of members, just the variables for which we can calculate a timescale, and then dividing them by class, there are very few objects left per class to analyze. Since we have shown that the timescales for [3.6] and [4.5] are generally well-matched, we can combine timescales derived via the channels, but even then, there are still very few objects per class. The medians of these combined timescale distributions show a weak trend; the median of the 10 class I objects is 9.5 d, the 14 flat class members have a median of 7.3 d, the 26 Class II members have a median of 7.5 f, and the median of the 5 class III members is 2.4 d. Since there are literature-identified Class 0 objects in this cluster, we had hoped we could pull out these objects separately, but only one has a timescale in either IRAC channel, and it is 2.4 d in [3.6] and 21 d in [4.5]. Due to small number statistics, an analysis of this sort will need to be repeated once all the YSOVAR clusters are analyzed, so that we have larger numbers of objects in each class.

The low-number statistics similarly make it difficult to look for correlations between timescale and amplitude, especially as a function of class. There is very little correlation between timescale and amplitude for the distribution as a whole. On average, the Class III objects not only have smaller timescales but also smaller amplitudes. Similarly, the Class Is tend to have larger timescales and larger amplitudes, but there

is rather a lot of scatter. In terms of color amplitude, the Class IIIs tend to have a smaller color change on average, but the rest of the classes cover similar, large color changes; the largest color changes are not the Class Is. Some of the largest color changes are in objects that have small timescales.

7.4. Periods
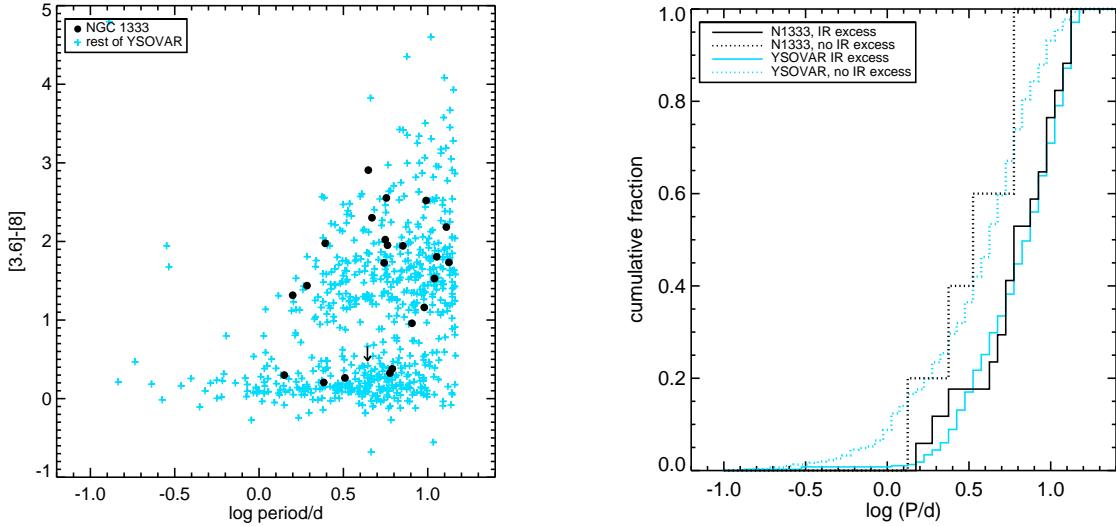
Fig. 19.— LEFT: Plot of log period (in days) against [3.6]−[8] as an indicator of IR excess. Solid circles (and one arrow) are points (and upper limits) for stars in NGC 1333; blue + are the rest of the points from the rest of the YSOVAR clusters (R14). There are no very fast rotators here in NGC 1333, and there is a range of IR excesses for the slower rotators. There is one [8] limit seen here, which does not appear in R14 (because it was limited to detections). RIGHT: cumulative distribution of period (in days) for NGC 1333, for [3.6]−[8]>0.8 (solid) and <0.8 (dotted), black lines. The blue lines are the equivalent for the entire YSOVAR sample (solid line is [3.6]−[8]>0.8 and dotted line is [3.6]−[8]<0.8).

In NGC 1333, we find 23 objects with periodic light curves, 19 of which are in the standard set of members. R14 discussed the relationship between period and IR excess for all the periodic objects over all 12 YSOVAR clusters; the NGC 1333 points are highlighted in Figure 19. There are no very short periods in this cluster; all of them are >1 d. These objects may not have had enough time yet to spin up. Figure 19 also has the cumulative distribution of periods. Half the periods are between 1.4 and 5.6 days; the other half are between 5.6 and 15 d.

Out of the objects with periods, there is a surprising fraction of objects that have relatively embedded SEDs. One object (SSTYSV 032901.87+311653.3) has a slope between 2 and 24 μm consistent with a Class I, but it has that slope (and therefore class) only because of a very bright but not obviously spurious 24 μm point. However, the 2-8 μm SED classification is Class III. This is clearly a case where a simple fit to all points between 2 and 24 μm does not adequately capture the nature of this source. This source would therefore be considered a transition object. Of the remaining periodic objects, 9 are flat class, 8 are Class II, and 5 are Class III. This is unusual compared to the other clusters as yet examined in detail, where the periodic sources

are predominantly Class IIIs. This could mean that the periodic signal is coming from the inner disk (e.g., Artemenko et al. 2013), not the photosphere. As a representative from these embedded periodic sources, Figure 20 shows the SED, phased light curve, and original light curve for SSTYSV J032857.11+311911.9. It has a flat SED class, but is still clearly periodic. The light curve morphology best matches expectations for an AA Tau analog, or 'dipper' – variable extinction from structure in the inner disk (e.g., Bouvier et al. 1999, McGinnis et al. 2015). (Dippers will be discussed more in the next subsection.)

One of the periodic objects (SSTYSV J032916.81+312325.2) has a strong 5.6 d period found independently in $[3.6]$, $[4.5]$, and $[3.6]-[4.5]$. Two of the other periodic objects are found from the $[3.6]-[4.5]$ color, not the $[3.6]$ or $[4.5]$ light curves alone; they are SSTYSV J032910.82+311642.7 and SSTYSV 032918.72+312325.4, the latter of which is shown in Figure 21. In both cases, there is a long term trend with texture on top, which may be why we see the signature in color but not the individual channels – subtracting the channels removes the long-term trend, leaving the color signature of a repeated pattern. SSTYSV J032918.72+312325.4 has a larger amplitude fluctuation than SSTYSV J032910.82+311642.7. For the former, while the Lomb-Scargle approach finds a significant period only in the color, the ACF analysis finds this timescale in $[4.5]$ and $[3.6]-[4.5]$. The net amplitude is $\Delta[3.6]-[4.5]\sim0.25$ mag, and the mean $[3.6]-[4.5]=0.48$ mag. In the other case of SSTYSV J032910.82+311642.7, the phased light curve is messy, but multiple approaches retrieve the same period. There is a net amplitude $\Delta[3.6]-[4.5]$ of ~0.1 mag, and a mean $[3.6]-[4.5]$ of 0.85 mag.

None of the periodic objects are particularly suggestive of eclipsing binaries. Several are very clear, repeatable signals suggestive of cold spots on the photosphere. Some have large-scale downward or upward trends, and/or the periodic signal is changing slightly with every repetition; in these cases, it may be that we are seeing signatures of accretion streams or hot spots on the photosphere. In a few cases, we see 'dippers' and 'bursters'; see next section.

We can investigate correlations between period and spectral type. Just four of the objects with periods are missing spectral types. If the object is unobscured enough that we can derive a period, then it is also unobscured enough that it has a measured spectral type. Figure 22 shows the period against the spectral type (K0=5.0, K2=5.2, M0=6.0, etc). There is a weak tendency for the later types to have a shorter period, suggesting that they are rotating (or have inner disks rotating) more quickly. There is no evidence for a similar trend in Orion or NGC 2264, though the sample sizes in those clusters are 15-20 times larger than that for NGC 1333.
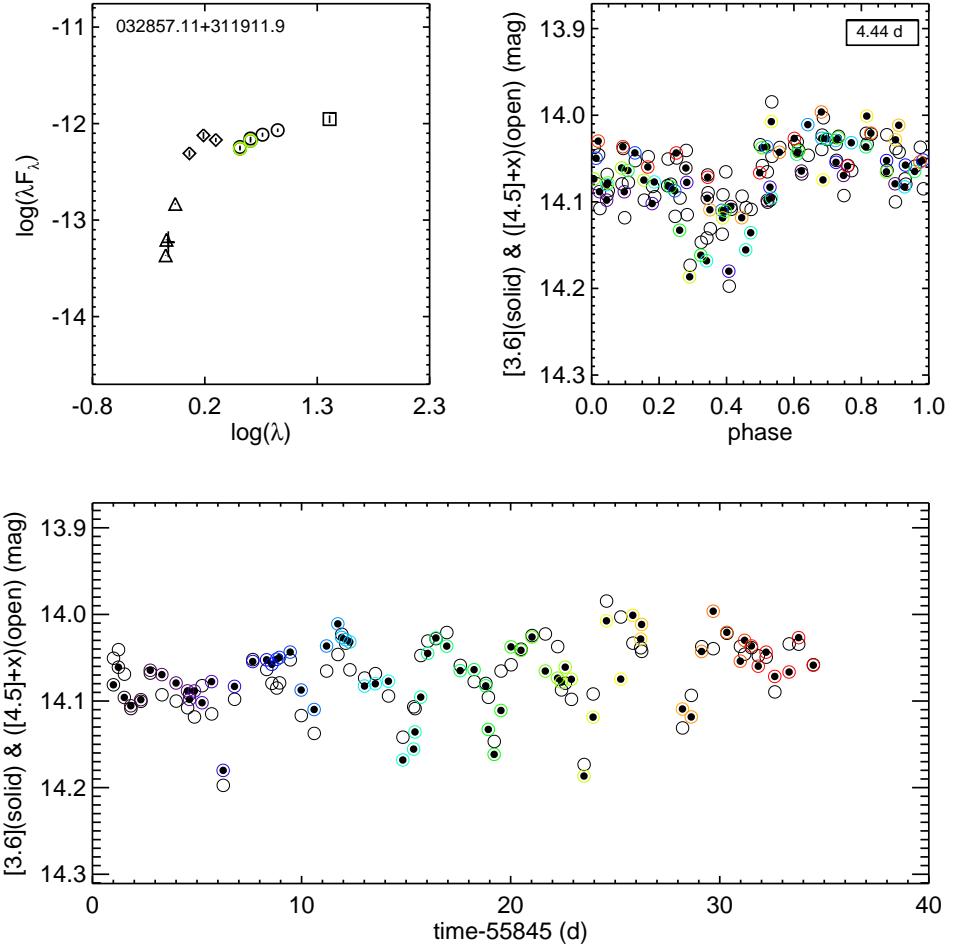
Fig. 20.— Plots for the periodic source SSTYSV J032857.11+311911.9 (=ASR64=MBO148=S-6). The SED in the upper left has the same notation as prior SEDs. The upper right is a phased light curve, where the period is 4.44 d, and the dot colors correspond to the circle colors shown on the full light curve on the bottom. In both the phased light curve and the full light curve on the bottom, solid circles are [3.6], open circles are [4.5], and the [4.5] light curve has been shifted such that the mean [4.5] matches the mean [3.6]. This periodic object is also a dipper – see Sec. 8 – and a brown dwarf at M7.3 – see Sec. 10.2.
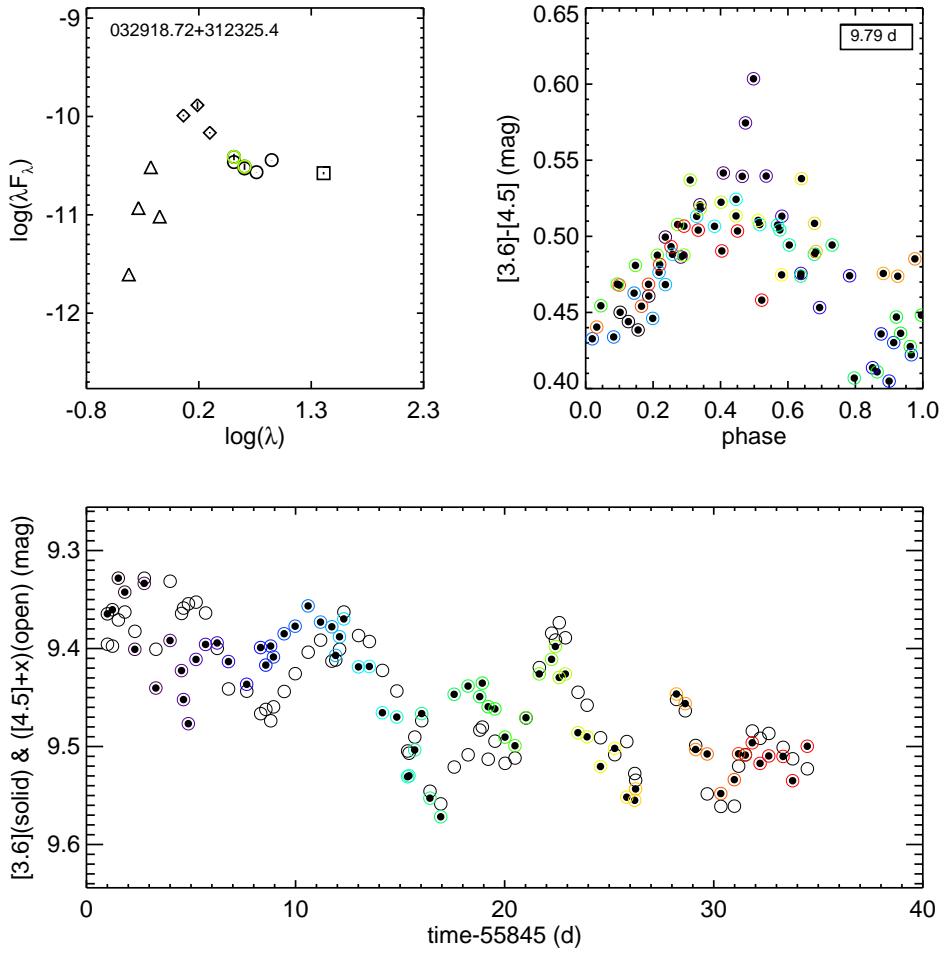
Fig. 21.— Plots for the periodic source SSTYSV J032918.72+312325.4 (=J070-29=LAL293=Getman 81=Preibisch 18=MBO16=Winston 106=Foster 167, an M0 spectral type). The SED in the upper left has the same notation as prior SEDs. The upper right is a phased *color* light curve, where the period is 9.79d. (Notation for this and the light curve is otherwise the same as Fig. 20.) This source was determined to be periodic from the change of [3.6]−[4.5] vs. time; there was no significant period determined from [3.6] or [4.5] alone.
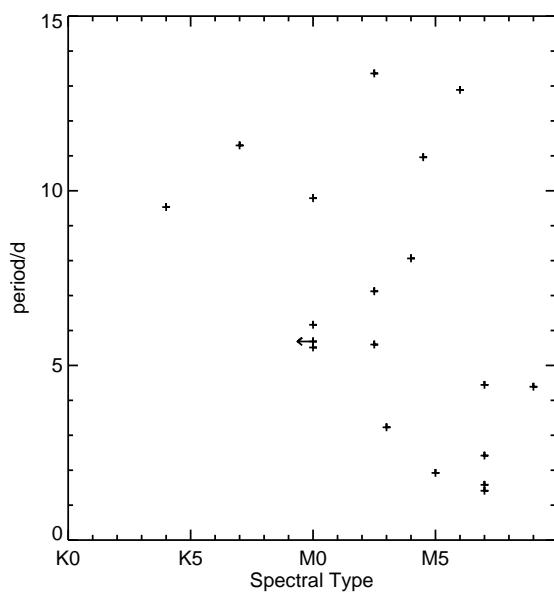
Fig. 22.— Period (in days) against the spectral type. There is a weak tendency for the later types to be rotating (or otherwise creating repeated texture in their light curves) more quickly.

8. Dippers and Bursters

Morales-Calderón et al. (2011), Cody et al. (2014), Stauffer et al. (2014, 2015), and McGinnis et al. (2015) identified and discussed objects from Orion and NGC 2264 that they categorized as 'dippers' (or AA Tau analogs) and 'bursters.' Dippers have light curves where there is a 'continuum' from which one can measure intermittent decreases in the observed flux, of typically a few hours to days. Bursters have light curves that are almost inverted dippers in that there is a 'continuum' from which one can measure intermittent increases in the observed flux. In both Orion and NGC 2264, there was copious additional contemporaneous data taken at a variety of wavelengths, which allowed an interpretation of dippers being largely due to stellar occultations by "texture" in the circumstellar dust disk (e.g., disk warps or overdensities), and that of bursters to be accretion instabilities (see, e.g., Kulkarni & Romanova 2009 or Romanova et al. 2011). We have far less ancillary data available here, but we can use the same metrics presented in Cody et al. (2014) to help identify the bursters and dippers, namely Q and M. The Q parameter is a measure of pattern repetition, and M is a measure of up/down symmetry. (Values for Q and M appear in Table 1.)

To calculate M, Cody et al. (2014) compare the mean and median of the light curves (having removed the highest and lowest 10% of points), and divide by the standard deviation of the light curve. Following the limits set in Cody et al. (2014), values of $M < -0.25$ suggests bursters, and $M > 0.25$ suggests dippers. The 'continuum' is thus defined as the mean of the light curve, and asymmetries are measured with respect to that mean.

Dippers and bursters as identified in earlier work are often but not always periodic. The NGC 1333 periodic sources listed in Sec. 7.4 above include 3 periodic bursters, and 1 periodic dipper, the latter of which is shown in Fig. 20. There are 8 aperiodic dippers. Two more bursters may be periodic, but on longer timescales than we can measure. The remaining 6 bursters (11 bursters - 3 periodic - 2 candidate periodic) are aperiodic.

Figure 23 (SSTYSV J032858.25+312202.0) is an example of an aperiodic burster. The light curve shows the characteristic behavior of having an apparent lower 'continuum' level with brighter flux excursions (bursts) of varying length superposed on top of the continuum level. However, it does not have a significant trend in the CMD; see next section.

9. Color Trends

For those objects with well-populated light curves at both bands, we can investigate the color trends over the YSOVAR campaign. Günther et al. (2014), Poppenhaeger et al. (2015), and Wolk et al. (2015) all find that many objects become bluer when brighter (as would be expected for variations in extinction), but that a few objects become redder when brighter. We look for these color trends in a slightly different way than the prior three studies. We describe our approach, followed by the results of this analysis in NGC 1333.

9.1. Finding Significant Color Trends

For most objects in the YSOVAR fields that have light curves at both bands, the [3.6] and the [4.5] observation at a given epoch were obtained within 12 minutes of each other. While this is not strictly simultaneous, for the timescales in which we are interested, we regard them as simultaneous. For each object that has light curves at both bands, we can construct both the [3.6] vs. [3.6]−[4.5] CMD and the [4.5] vs.
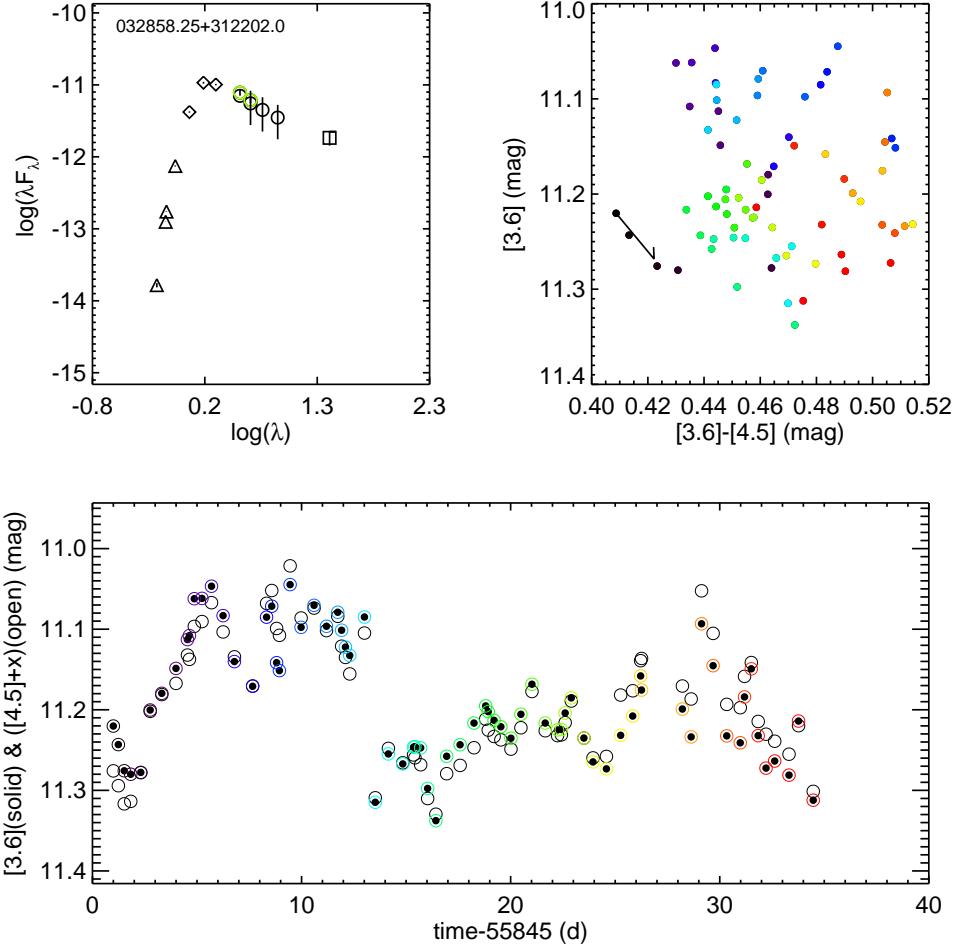
Fig. 23.— Plots for the aperiodic burster source SSTYSV 032858.25+312202.0 (=LAL163=MBO47=Foster 65). Notation is as in prior similar figures. This object is also a brown dwarf at M6 – see Sec. 10.2.

[3.6]−[4.5] CMD. We calculate a linear Pearson correlation coefficient for the distribution of points. However, this calculation does not take into account the intrinsic errors on each point. We used a 'safe correlation' routine by P. Lloyd found in the IDL Astronomy Library[5] to calculate 10^4 realizations of the data, where each point can vary its location corresponding to the error on the point (in both dimensions). It then recalculates the Spearman rank correlation coefficient for each realization of the data. From the distribution of the correlation coefficients, the routine determines the probability that the original distribution could be uncorrelated. We calculated these values for both CMDs, for all objects that had light curves in both bands. By inspection of several hundred CMDs, we determined that a significant correlation could be found in the CMD if the absolute value of the correlation coefficient was >0.45 and at the same time the probability calculated by the safe correlation routine was <15%. Based on empirical tests, between 1-5 outlying points can affect these statistics, but the influence of these outliers is limited. Usually if there is a strong correlation,

---

[5]http://idlastro.gsfc.nasa.gov/homepage.html and http://parkeloyd.com/output/code/safe_correlate/

it stays strong even if outliers are removed.

Following the reddening law of Cardelli, Clayton, & Mathis (1989), in the [3.6] vs. [3.6]−[4.5] CMD, the slope of the reddening vector should be ∼3.5, and in the second [4.5] vs. [3.6]−[4.5], it should be ∼2.5. Using the much more recent Indebetouw et al. (2008) values for IRAC bands and the interstellar medium, the slope of the reddening vector should be ∼4.5 and ∼3.5, respectively. For either one, the slope expected from reddening is larger in a [3.6] vs. [3.6]−[4.5] diagram than in a [4.5] vs. [3.6]−[4.5] diagram. Thus, variations consistent with reddening are slightly more easy to find (given our approach) in the [3.6] vs. [3.6]−[4.5] diagram than in the other one.

9.2.   Color Trends in NGC 1333

For NGC 1333, there are 17 objects that have a significant correlation in the [3.6] vs. [3.6]−[4.5] CMD in the direction of bluer when brighter and redder when fainter (consistent with extinction variations), but no significant correlation in [4.5] vs. [3.6]−[4.5]. There are 6 objects that have a significant correlation in both CMDs for redder when fainter (bluer when brighter). There are 15 objects that have a significant correlation in [4.5] vs. [3.6]−[4.5] in the very roughly orthogonal direction of bluer when fainter, but no significant correlation in [3.6] vs. [3.6]−[4.5]. There is only one object that has a significant correlation in both CMDs (for bluer when fainter). Objects that become redder when fainter have been referred to as 'reddeners', and objects that become bluer when fainter have been referred to as 'bluers' or 'blueners' (Günther et al. 2014, Poppenhaeger et al. 2015, & Wolk et al. 2015). Figures 24 – 27 show examples of these four cases – significant positive correlation in [3.6] vs. [3.6]−[4.5], significant positive correlation in both, significant negative correlation in [4.5] vs. [3.6]−[4.5], and significant negative correlation in both.

SSTYSV J032851.24+311739.3 (Fig. 24) is an example of an object that has a significant 'red' trend (redder when fainter) in [3.6] vs. [3.6]−[4.5] but not in [4.5] vs. [3.6]−[4.5]. We note here that this is an edge-on disk (Hodapp et al. 2004), which is the right geometry to create a dipper object, but the light curve for this object is symmetric above and below its mean, so is not characterized as a dipper.

SSTYSV J032851.19+311954.8 (Fig. 25) is one of 6 light curves that have a significant redder-when-fainter trend, but also one of the ∼25% of variable objects that have a significant overall trend in the original light curve. This long, slow trend (sometimes with a concurrent trend in the CMD, sometimes not) over the entire campaign is very common in this cluster.

SSTYSV J032856.30+312227.9 (Fig. 26) is an example of a light curve that has a significant 'blue' trend (bluer when fainter) in [4.5] vs. [3.6]−[4.5] but not in [3.6] vs. [3.6]−[4.5]. This object is also identified as a dipper, since there is a flux asymmetry such that there is a continuum from which downward excursions can be identified.

SSTYSV J032909.32+312104.1 (Fig. 27, in addition to being the only source with signficant trend in the direction of bluer when fainter, has interesting 'tracks' in its CMD. When the YSOVAR campaign starts (the darkest points in the figure), it is already moving in the general direction of redder when brighter. As it climbs the brightness peak towards day ∼12 of the campaign (blue points in the figure), it becomes dramatically redder and brighter. As it falls back to its original brightness (cyan/green in the figure), it becomes bluer. Interestingly, the variations near the end of the fall, and after it (light green, yellow, red), are all back to moving in the direction of bluer when brighter, more consistent with the slope of the reddening vector. This is a fascinating source. While this source is in a region of high surface brightness (∼2 MJy

sr^{-1} at 3.6 μm), it is relatively isolated, so these variations are unlikely to be the result of an instrumental artifact. We have 9 epochs of J, H, or K_s data over this 40 d window, but the JHK_s variations seem to be independent of the IRAC variations. It is not at all clear what is happening in/near this source.

There are 39 sources in NGC 1333 that have one of these four color trends. Sources of all SED classes are found with either of the 'red' trends (that is, redder when fainter in one or both CMDs). Sources of all classes except for Class I are found with the 'blue' (bluer when fainter) trends. There are fewer of these 'blue' sources (16 vs. 23), and only one of the sources has a 'blue' trend in both CMDs (it is a Flat class). So, the observation that none of the most embedded sources have a 'blue' trend may be a result of small number statistics, but is nonetheless interesting. Only one of the 'blue' sources is a class III, and two of the 'red' sources are Class III. More detailed analysis of trends of color with SED class will require combination of data from this cluster with other YSOVAR clusters.
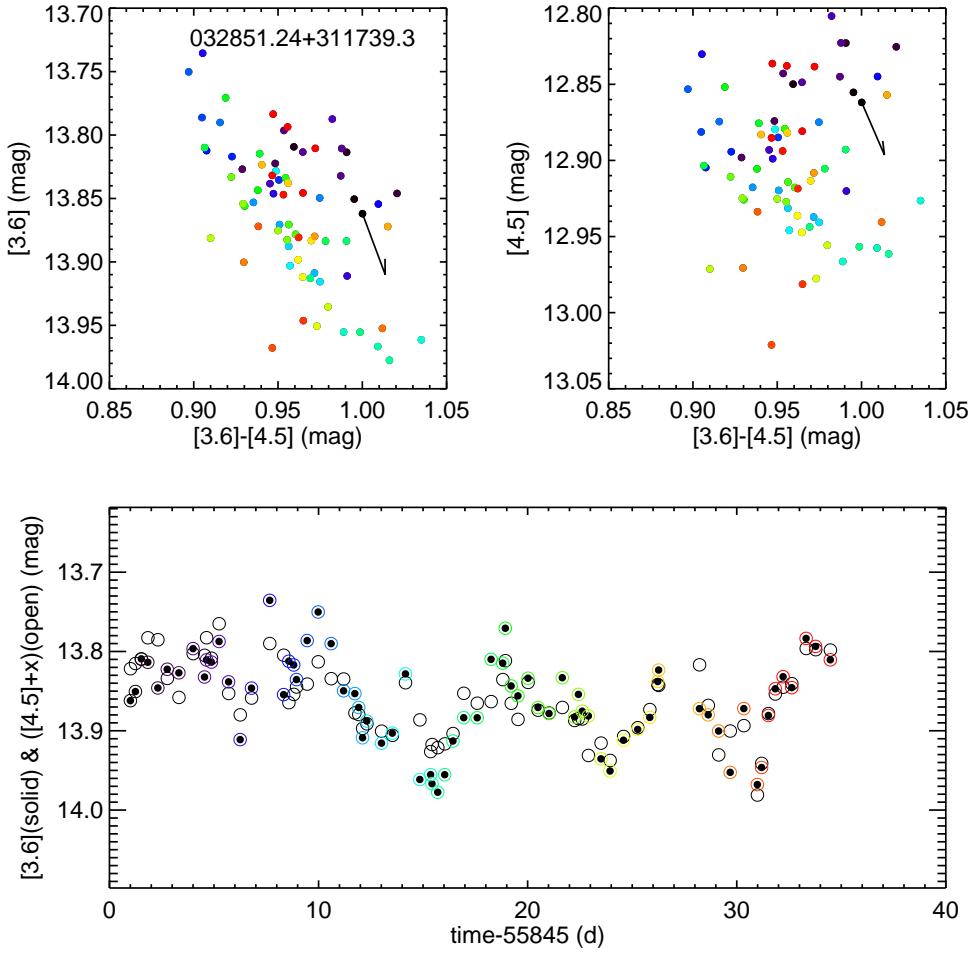
Fig. 24.— Color-magnitude diagrams and light curve for SSTYSV 032851.24+311739.3 (=ASR41=LAL111, and a known edge-on disk – Hodapp et al. 2004), a source that has a significant 'red' trend (redder when fainter) in [3.6] vs. [3.6]−[4.5] but not in [4.5] vs. [3.6]−[4.5]. Notation is as in prior CMDs and light curves. A reddening vector with $A_V=1$ is shown from the first point in each CMD. The correlation coefficients calculated as per the text is 0.56 for the first CMD and 0 for the second. The 'safe correlate' routine finds that there is a 0.6% chance that the points are not correlated in the first CMD, and a 64% chance that the points are not correlated in the second CMD..
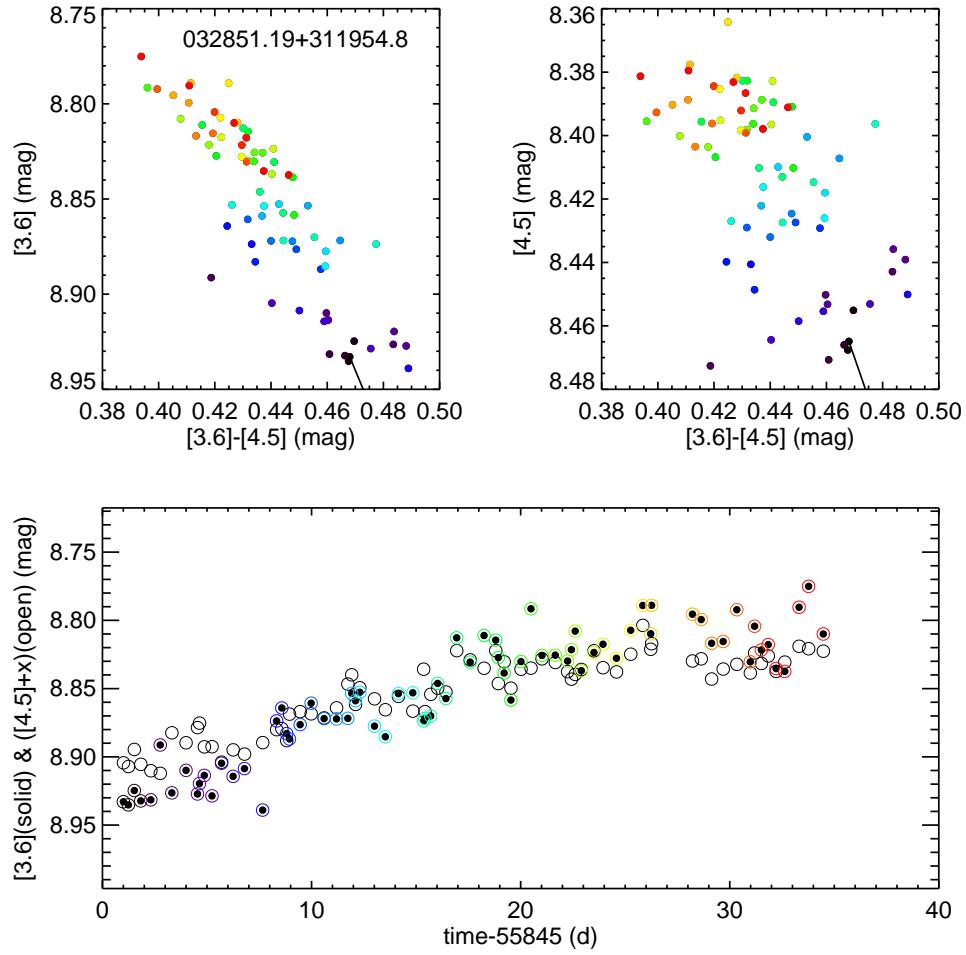
Fig. 25.— Color-magnitude diagrams and light curve for SSTYSV 032851.19+311954.8 (=ASR125=LAL110=Getman 21=Preibisch 7=MBO14=Winston 53=Foster 37, a K7 spectral type), a source that has a significant 'red' trend (redder when fainter) in both CMDs. Notation is as in prior CMDs and light curves. The correlation coefficients calculated as per the text is 0.86 for the first CMD and 0.60 for the second. The 'safe correlate' routine finds in both cases that there is a <0.05% chance that the points are not correlated.
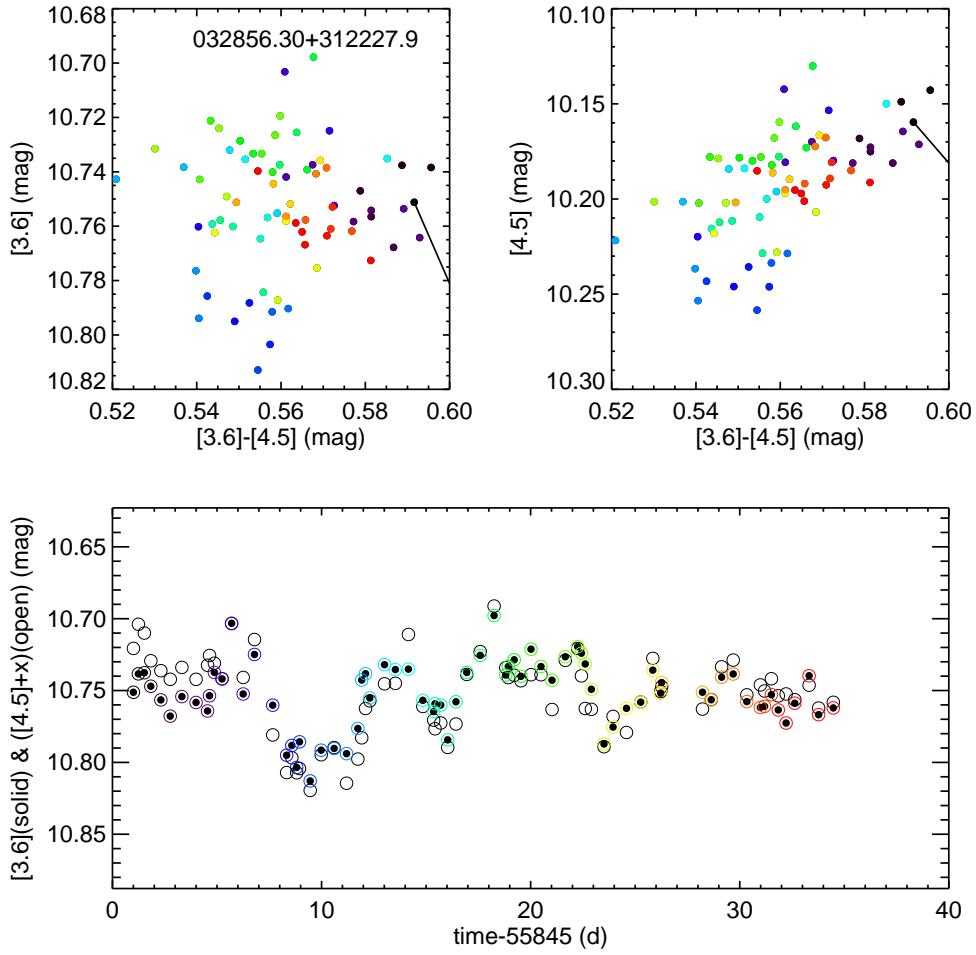
Fig. 26.— Color-magnitude diagrams and light curve for SSTYSV 032856.30+312227.9 (=LAL147=MBO37=Winston92=Foster 51, an M2 spectral type), a source that has a significant 'blue' trend (bluer when fainter) in [4.5] vs. [3.6]−[4.5] but not in [3.6] vs. [3.6]−[4.5]. Notation is as in prior CMDs and light curves. The correlation coefficients calculated as per the text is 0.−0.05 for the first CMD and −0.59 for the second. The 'safe correlate' routine finds for the first CMD that there is a 58% chance that the points are not correlated, but a <0.05% chance that the points are not correlated in the second.
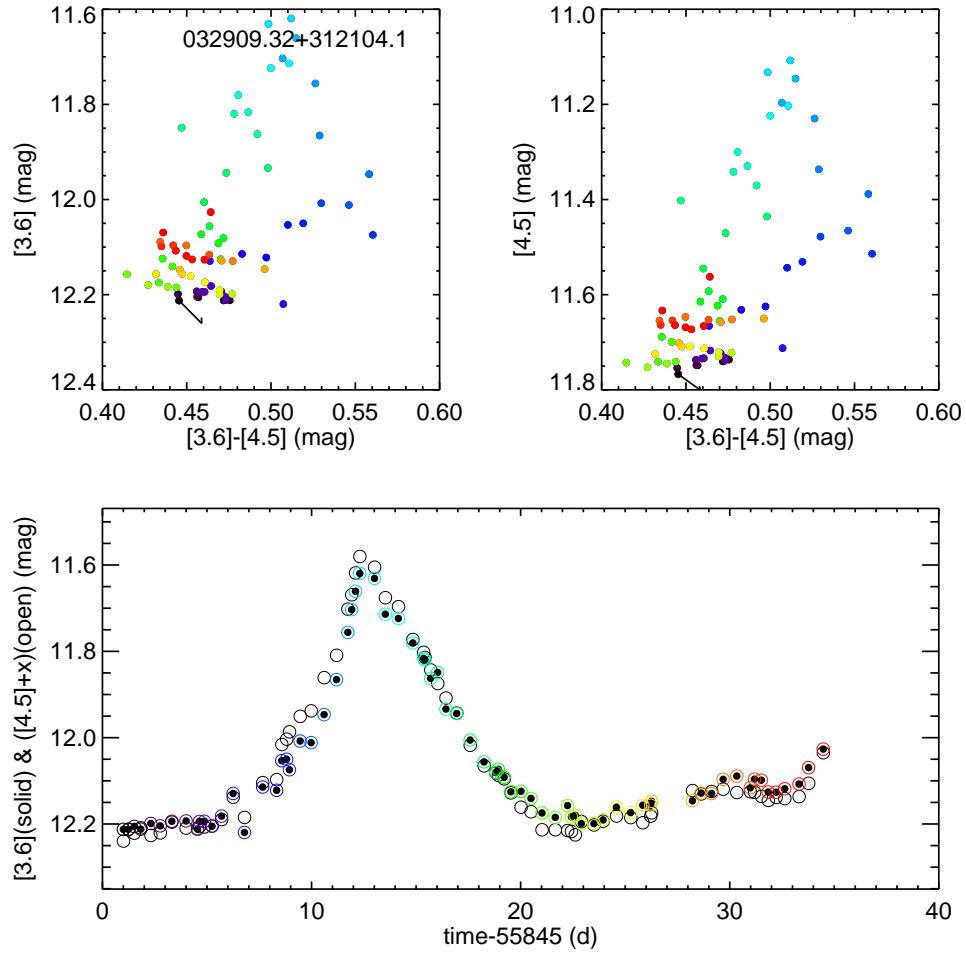
Fig. 27.— Color-magnitude diagrams and light curve for SSTYSV 032909.32+312104.1 (=LAL225=MBO70=Foster 126=S-12), a source that has a significant 'blue' trend (bluer when fainter) in both CMDs. Notation is as in prior CMDs and light curves. The correlation coefficients calculated as per the text is −0.52 for the first CMD and −0.64 for the second. The 'safe correlate' routine finds in both cases that there is a <0.05% chance that the points are not correlated.

10.   Special Sources

10.1.   Class 0 and Jet Drivers

NGC 1333 is unusual in that it has several very embedded, very young sources, and sources thought to be driving jets. Unlike most of the other cluster members with YSOVAR light curves, the flux density in the IRAC bands for these most embedded sources may very well be dominated by outflow-driven molecular hydrogen emission, which can be close to the source (e.g., Arnold et al. 2012). Thus, the origin of the variability in these objects may be very different, and it is worth looking just at the characteristics of the Class 0s and jet drivers.

In R15, we identified Class 0 and jet-driving objects from the literature. Of those sources, 17 have light curves in one or both bands; they are listed in Table 6. These objects are relatively faint at [3.6], as seen in Table 6; the mean [3.6] from the cryo era is ∼14, whereas the mean [4.5] is ∼12.5. Only 6 of the 17 (a third) are variable in either channel over the YSOVAR campaign; 9 of them (half) are CY variable. This is perhaps not surprising; maybe the most embedded sources may only vary on very long timescales because the envelope takes time to change in response to things going on near the YSO. Very large variations on long timescales could occur as the YSO accretes at an unsteady rate, with the reprocessed radiation creating large amplitude variations on relatively long timescales. Of the 7 that are specifically identified as jet drivers, 4 (∼ 60%) are variable over the YSOVAR campaign, and 5 (∼ 70%) are CY variable. Of the 15 that are specifically identified as Class 0s, 4 (∼ 25%) are variable over the YSOVAR campaign, and 7 (∼ 50%) are CY variable. Since the jet driving mechanism is thought to be accretion-driven, and accretion is highly unlikely to be a smooth, isotropic process, it makes sense that there is a higher fraction of variables among the jet-driving sources. Or, we could be seeing variation in the molecular hydrogen emission close to the source.

Unfortunately, only 6 of the Class 0 or jet driving sources have reasonable two-band coverage. Of those 6 sources, half of them are variable over the YSOVAR campaign, and all three of those variables have significant color variability consistent with reddening variations in the [3.6] vs. [3.6]−[4.5] CMD. One of these objects, SSTYSV J032910.70+311820.9, was called out above for having a very large CY variation; it appears in Fig. 16. The other two sources are SSTYSV J032856.11+311908.5 (Fig. 28) and SSTYSV J032911.24+311831.8 (Fig. 29).

10.2.   Brown Dwarfs

In NGC 1333, there are 55 objects with light curves and spectral types of M4 or later, and 33 of those are type M6 or later (where M6 is often taken as the stellar/sub-stellar boundary at ∼1 Myr). These are among the youngest and most embedded brown dwarfs to ever be monitored in the MIR. About a quarter of the brown dwarfs (8/33) are variable. These variable objects include some that are relatively faint, but they are not the majority; the mean [3.6] from the cryo era is ∼12.6, and that for [4.5] is ∼12.1; the mean magnitudes for the ensemble of type M6 or later are ∼13 in both bands. These objects have widely ranging timescales and amplitudes, and do not stand out from the rest of the population via those metrics. Of the 8 variables, there are 1 Flat class, 5 Class IIs, and 2 Class IIIs.

Five of the eight variable BDs are periodic, so the BDs stand out as having a high fraction of periodic sources. At M7.3, SSTYSV 032857.11+311911.9 in Fig. 20 above is one of the periodic BDs. Fig. 23 above is a burster, but is also a BD with a type of M6. Of the eight variable brown dwarfs, three of them

have significant color variabilty, and all of those have significant redder-when-brighter (perpendicular to the reddening vector) behavior, though admittedly just in the [4.5] vs. [3.6]−[4.5] CMD. This is significantly more common than in the general population of variables.
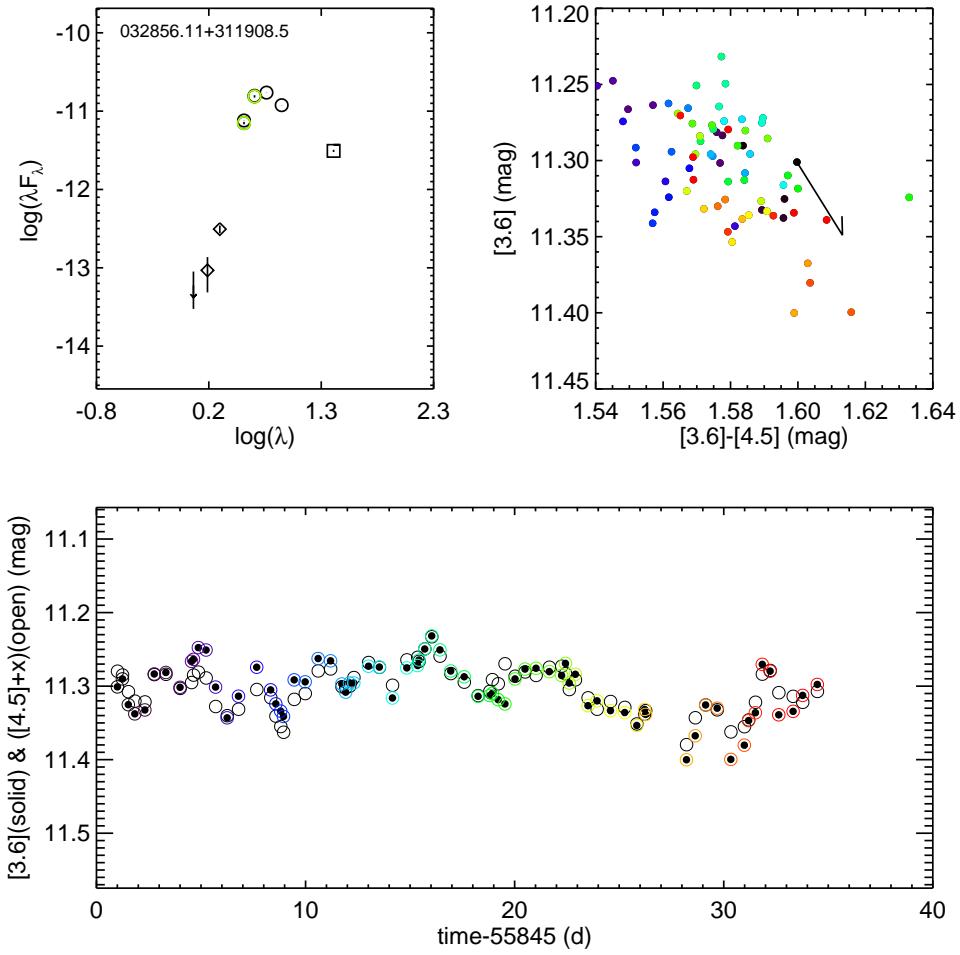
Fig. 28.— Plots for the literature-identified Class 0 source SSTYSV 032856.11+311908.5 (=MBO146=Winston43). The SED in the upper left has the same notation as prior SEDs. The upper right is a CMD, and the light curve is at the bottom.
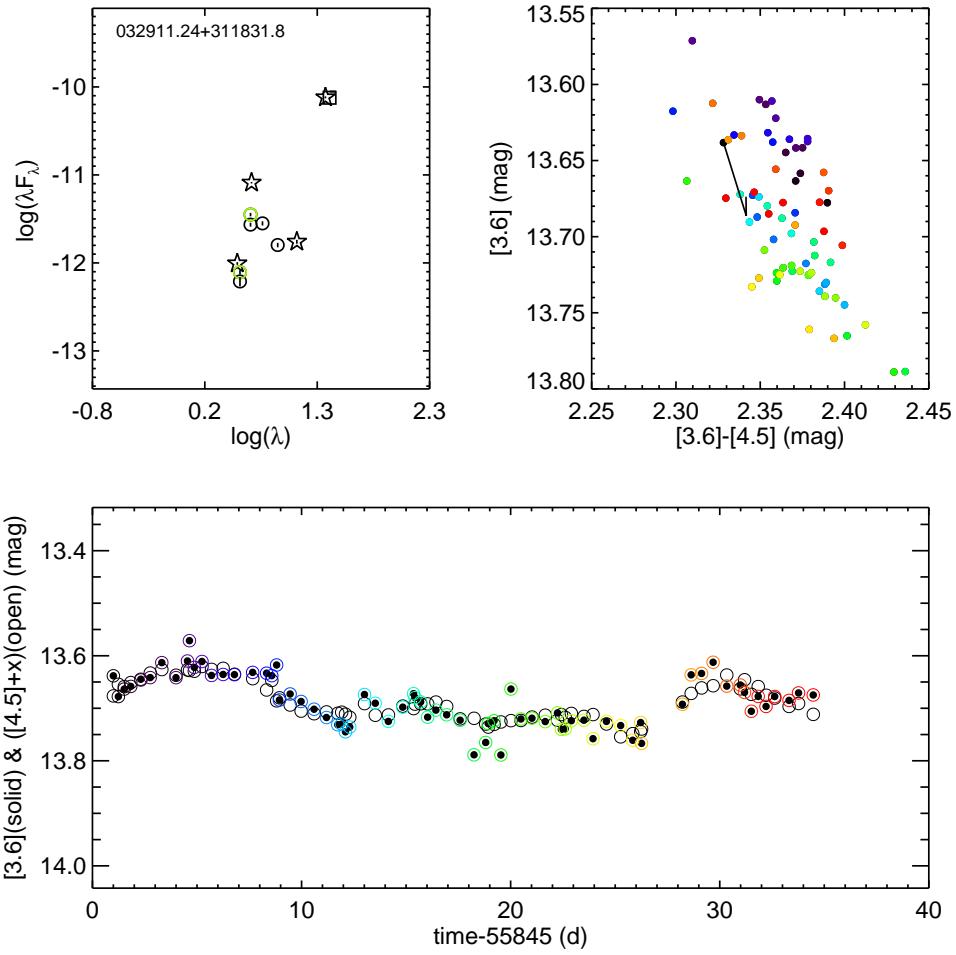
Fig. 29.— Plots for the literature-identified Class 0 and jet-driving source SSTYSV J032911.24+311831.8 (=IRAS7=West14=J07-24=VLA 27=Gutermuth 7, but *not* ASR 32; see R15). The SED in the upper left has the same notation as prior SEDs. The upper right is a CMD, and the light curve is at the bottom.

Table 6.   Class 0 and Jet Drivers

SSTYSV	Class 0	Jet driver	Our class	CY var	Var	$[3.6]_{\rm cryo}$	$[4.5]_{\rm cryo}$	Notes
032855.53+311436.3	yes	yes	I	yes	yes	12.66	10.18	mostly [4.5] only
032856.11+311908.5	yes	no	I	no	yes	11.22	9.71	significant variability consistent with reddening variations in the [3.6] vs. [3.6]−[4.5] CMD
032857.37+311415.7	no	yes	I	yes	yes	9.87	7.81	[4.5] only
032900.50+311200.7	yes	yes	I	yes	no	$\cdots$	15.73	[4.5] only
032901.91+311541.4	yes	no	I	no	no	16.07	14.36	[4.5] only, only 8 points
032904.07+311446.5	yes	yes	I	no	no	14.21	12.81	[4.5] only, but may be non-variable because of large errors; texture is in LC
032906.45+311534.4	yes	no	II	no	no	14.38	13.38	
032910.70+311820.9	no	yes	I	yes	yes	12.57	10.82	significant variability consistent with reddening variations in the [3.6] vs. [3.6]−[4.5] CMD; large CY variation
032910.96+311825.6	yes	no	I	yes	no	13.82	12.87	relatively few points
032911.24+311831.8	yes	yes	I	yes	yes	13.95	11.61	significant variability consistent with reddening variations in the [3.6] vs. [3.6]−[4.5] CMD; potentially large variations on multi-year timescales
032912.05+311301.4	yes	yes	I	no	no	13.95	10.47	[4.5] only
032912.05+311305.8	yes	no	I	yes	yes	17.44	13.16	[4.5] only
032913.60+311358.0	yes	no	I	yes	no	15.69	13.53	[4.5] only
032914.96+312031.7	yes	no	II	no	no	14.81	14.13	
032917.11+312745.5	yes	no	I	no	no	14.28	12.78	[3.6] only
032917.47+312748.2	yes	no	I	yes	no	15.88	14.62	[3.6] only
032918.88+312313.0	yes	no	I	no	no	15.85	14.07	

11. Summary

We have presented YSOVAR data for NGC 1333. There are 701 objects with mid-IR light curves in one or both warm Spitzer bands. We find 92 objects that are mid-IR variable between the cryo-era observations and the YSOVAR campaign, but only one (SSTYSV J032910.70+311820.9) with a large color change between the cryo era and the YSOVAR campaign. There are 78 objects that are variable over the YSOVAR campaign, nearly all of which were identified as NGC 1333 members prior to this work. However, the fraction of NGC 1333 members that are mid-IR variable, at $\sim$50%, may be low compared to similar fractions from other clusters (typically closer to 75%-80%). We found evidence for a larger variability fraction among more embedded sources.

With amplitude defined as the difference between the 10th and 90th percentile in the brightness distribution of points, typical amplitudes are $\sim$0.1-0.15 and 20% vary at 0.2 mags or more. Amplitudes for disked sources are indistinguishable by class, but Class III objects have lower amplitudes.

In terms of color changes, the distribution of [3.6]−[4.5] amplitudes is typically $\sim$0.05 mag. Larger color changes generally (although not always) also translate to larger single-band changes. There are no discernible trends of amplitude of color change with effective temperature. The most extreme color change is >0.2 mag change (SSTYSV J032904.31+311906.3), implying $\Delta A_V \sim$15-30 mag. For those variable objects with light curves in both IRAC bands, there are 6 objects that have a significant redder-when-fainter ('red') trend in CMDs, roughly consistent with the direction expected for reddening variations. One object, SSTYSV J032909.32+312104.1, has a significant bluer-when-fainter ('blue') trend in both CMDs, roughly perpendicular to that expected for reddening. There are 17 objects that have a significant red trend in [3.6] vs. [3.6]−[4.5] but not the other CMD, and 15 objects that have a significant blue trend in [4.5] vs. [3.6]−[4.5]. Sources with all SEDs are found with the red trends, but no Class I sources are found with blue trends.

Timescales for the variability seem to be $\lesssim$5d. We found only weak evidence for longer timescales among more embedded sources. Some of the largest color changes are in objects that have small timescales.

Finally, NGC 1333 provides a higher fraction of known or suspected Class 0 sources, jet drivers, and brown dwarfs than the rest of the YSOVAR clusters. Class 0s and/or jet drivers are often faint in [3.6], but the light curves we have for these objects span a wide range of timescales and amplitudes, and they are more likely to be variable on the 6-7 year timescale of the cryo-to-YSOVAR campaigns. The brown dwarfs tend to be periodic, and more often found to have significant color variability (and more often have 'blue' color variability) compared to stellar sources.

REFERENCES

Arnold, L., A., Watson, D., Kim, K., et al., 2012, ApJS, 201, 12

Artemenko, S., Grankin, K., Petrov, P., 2012, AstL, 38, 783

Aspin, C., Sandell, G., Russell, A., A&AS, 106, 165 (ASR)

Baba, H., Yasuda, N., Ichikawa, S.-I., Yagi, M., Iwamoto, N., Takata, T., Horaguchi, T., Taga, M., Watanabe, M., Ozawa, T., & Hamabe, M. 2002, ASPC, 281, 298

Bally, J., Walawender, J., Johnstone, D., Kirk, H., Goodman, A., 2008, in Handbook of Star Forming Regions Vol. 1, ed B. Reipurth, ASP Publications, p. 308

Barsony, M., Ressler, M., & Marsh, K., 2005, ApJ, 630, 381

Bertin, E., & Arnouts, S., 1996, A&AS, 117, 393

Bertin, E., Mellier, Y., Radovich, M., et al., 2002, Astronomical Data Analysis Software and Systems XI, ASP Conference Proceedings, Vol. 281, 228

Bertin, E., 2006, Astronomical Data Analysis Software and Systems XV, ASP Conference Series, 351, 112

Bertin, E., 2011, ASPC, 442, 435

Bloom, J. S., Starr, D. L., Blake, C. H., Skrutskie, M. F., & Falco, E. E. 2006, Astronomical Data Analysis Software and Systems XV, 351, 751

Boulade, O., Charlot, X., Abbon, P., Aune, S., Borgeaud, P., Carton, P.-H., Carty, M., Da Costa, J., Deschamps, H., Desforge, D., Eppellé, D., Gallais, P., Gosset, L., Granelli, R., Gros, M., de Kat, J., Loiseau, D., Ritou, J.-., Roussé, J. Y., Starzynski, P., Vignal, N., & Vigroux, L. G., 2003, SPIE, 4841, 72

Bouvier, J., Chelli, A., Allain, S., et al., 1999, A&A, 349, 619

Bouy, H., Bertin, W., Moraux, E., et al., 2013, 554, 101

Bouy, H., Bertin, E., Sarro, L., et al., 2015, A&A, 575, 120

Burgasser, A. J., Kirkpatrick, J. D., Reid, I. N., Brown, M. E., Miskey, C. L., & Gizis, J. E. 2003, ApJ, 586, 512

Choi, P. I. & Herbst, W. 1996, AJ, 111, 283

Cardelli, J., Clayton, G., & Mathis, J., 1989, ApJ, 345, 245

Cody, A.M.,, Stauffer, J., Baglin, A., et al., 2014, AJ, 147, 82

Davis, C. J., Scholz, P., Lucas,P., Smith, M. D., Adamson, A., 2008, MNRAS, 387, 954

Drew, J., Greimel, R., Irwin, M., et al., 2005, MNRAS, 362, 753

Evans, N. J., Allen, L. E., Blake, G., et al. 2003, PASP, 115, 965

Evans, N. J., Dunham, M. M., Jørgensen, J., et al. 2009, ApJS, 181, 321

Fazio, G. G., Hora, J. L., Allen, L. E., et al., 2004, ApJS, 154, 10

Findeisen, K., Cody, A. M., Hillenbrand, L. A., 2015, ApJ, 798, 89

Flaherty, K. M., Muzerolle, J., Wolk, S., et al. 2014, ApJ, 793, 2

Forbrich, J., Osten, R., Wolk, S., 2011, ApJ, 736, 25

Foster, J., Cotaar, M., Covey, K., et al. 2015, ApJ, 799, 136

Getman, K., Feigelson, E., Townsley, L., Bally, J., Lada, C., Reipurth, B., 2002, ApJ, 575, 354

Greissl, J., Meyer, M., Wilking, B., et al. 2007, AJ, 133, 1321

Gutermuth, R. A., Myers, P. C., Megeath, S. T., et al. 2008, ApJ, 674, 336

Gutermuth, R. A., Megeath, S. T., Myers, P., et al. 2009, ApJ, 184, 18 (G09)

Gutermuth, R. A., Megeath, S. T., Myers, P., et al. 2010, ApJS, 189, 352

Harvey, P., Smith, B., di Francesco, J., Colome, C., 1998, ApJ, 499, 294

Herbst, W.,Dhital, S., Francis, A., Lin, L., Tresser, N., Williams, E., 2006, PASP, 118, 828

Hillenbrand, L., Findeisen, K., 2015, ApJ, in press (astroph 1506.011256)

Hodapp, K., Walker, C., Reipurth, B., et al. 2004, ApJ, 601, 79

Hodapp, K., in The Star Formation Newsletter, #268, 12 April 2015, p 5 (http://www.ifa.hawaii.edu/users/reipurth/newsletter/newsletter268.pdf)

Indebetouw, R. et al., 2005, ApJ, 619, 931

Jørgensen, J., Harvey, P., Evans, N. J., et al. 2006, ApJ, 645, 1246

hanzadyan, T., Smith, M., Davis, C., Gredel, R., Stanke, T., Chrysostomou, A., 2003, MNRAS, 338, 57

Kulkarni, A., & Romanova, M., 2009, MNRAS, 398, 701

Landolt, A., 1992, AJ, 104, 340

Liseau, R., Lorenzetti, D., Molinari, S., 1992, A&A, 253, 119

Magnier, E. A., & Cuillandre, J.-C., 2004, PASP, 116, 449

McGinnis, P., Alencar, S., Guimarães, M., et al., 2015, A&A, 577, 11

McQuillan, A., Aigrain, S., & Mazeh, T. 2013, MNRAS, 432, 1203

Melis, C.,Zuckerman, B., Rhee, J., Song, I., Murphy, S., Bessell, M., 2012, Nature, 487, 74

Meng, H., Rieke, G., Su, K., Ivanov, V., Vanzi, L., Rujopakarn, W., 2012, ApJ, 751, 17

Meyer, M., Calvet, N., Hillenbrand, L., 1997, AJ, 114, 288

Miyazaki, S., Komiyama, Y., Sekiguchi, M., et al., 2002, PASJ, 54, 833

Morales-Calderón, M., Stauffer, J., Hillenbrand, L., et al. 2011, ApJ, 733, 50 (MC11)

Plunkett, A., Arce, H., Corder, S., Mardones, D., Sargent, A., Schnee, S., 2013, ApJ, 774, 22

Raga, A., Noriega-Crespo, A., Carey, S., Arce, H., 2013, AJ, 145, 28

Rebull, L., Cody, A. M., Covey, K., et al., 2014, AJ, 148, 92 (R14)

Rebull, L., 2015, AJ, in press (R15)

Ridge, N., Di Francesco, J., Kirk, H., et al., 2006, AJ, 131, 2921

Rieke, G., Young, E., Engelbracht, C., et al. 2004, ApJS, 154, 25

Romanova, M., Ustyugova, G., Koldoba, A., Lovelace, R., 2011, MNRAS, 416, 416

Sadavoy, S., DiFrancesco, J., André, Ph. et al., 2014, ApJ, 787, 18

Sandell, G., & Knee, L., ApJ, 2001, 546, 49

Scargle, J. D., 1982, ApJ, 263, 835

Scholz, A., Geers, V., Jayawardhana, R., et al., 2009, ApJ, 702, 805

Scholz, A., 2012, MNRAS, 420, 1495

Scholz, A., Muzic, K., Geers, V., et al., 2012a, ApJ, 744, 6

Scholz, A., Jayawardhana, R., Muzic, K., et al., 2012b, ApJ, 756, 24

Skrutskie, M., Cutri, R. M., Stiening, R., et al., 2006, AJ, 131, 1163

Smith, J. A., Tucker, D., Kent, S., et al., 2002, AJ, 123, 2121

Stauffer, J., Hartmann, L., Fazio, G., et al., 2007, ApJS, 172, 663

Stauffer, J., Cody, A. M., Baglin, A., et al., 2014, AJ, 147, 83

Stauffer, J., Cody, A. M., McGinnis, P., et al., 2015, AJ, 149, 130

Stetson, P., 1996, PASP, 108, 851

Strom, S., Grasdalen, G., Strom, K., 1974, ApJ, 191, 111

Strom, S., Vrba, F., Strom, K., 1976, AJ, 81, 314

Taylor, M. B., 2005, ASPC, 347, 29

Taylor, M. B., 2006, ASPC, 351, 666

Vandame, B., 2002, SPIE, 4847, 123 (astro-ph/0208230)

Walawender, J., Bally, J., Francesco, J., Joergensen, J., Getman, K., 2008, in Handbook of Star Forming Regions, Volume I: The Northern Sky ASP Monograph Publications, Vol. 4. Edited by Bo Reipurth, p.346

Werner, M., Roellig, T., Low, F., et al., 2004, ApJS, 154, 1

Wilking, B. A., Bontemps, S., Schuler, R. E., et al., 2001,ApJ, 551, 357

Winston, E., Megeath, S., Wolk, S., et al., 2009, AJ, 137, 4777

Winston, E., Megeath, S., Wolk, S., et al., 2010, AJ, 140, 266

Wright, E., Eisenhardt, P. R. M., Mainzer, A. K., et al., 2010, AJ, 140, 1868

Zasowski, G., Johnson, J. A., Frinchaboy, P. M., et al. 2013, AJ, 146, 81

A. Appendix: Famous YSOs

This section collects a list of the most famous YSOs in NGC 1333, and adds figures for those objects not already presented above.
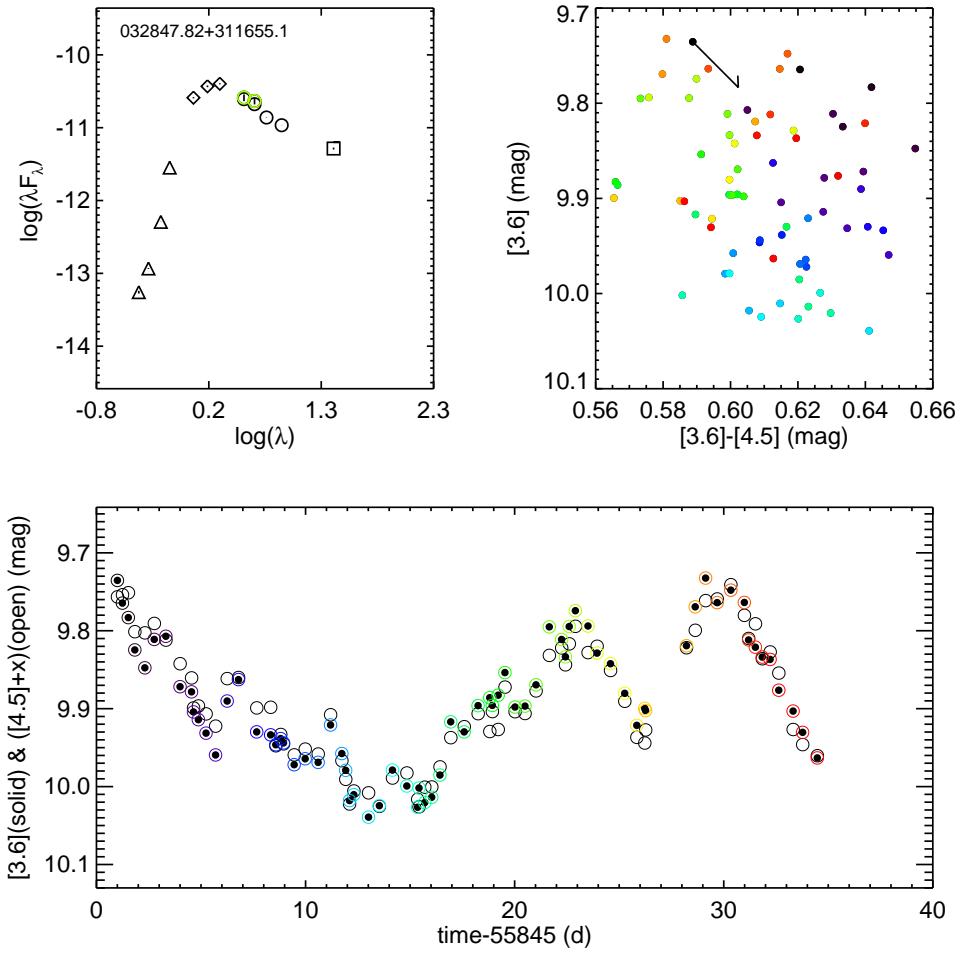
Fig. 30.— Light curve for famous YSO SSTYSV J032847.82+311655.1 (SSV17); see Table 7.

Table 7.   Famous YSOs

| SSTYSV name	Synonyms	Figure	Notes
Variables over the YSOVAR campaign			
032847.82+311655.1	SSV17	Fig. 30	Long-term trends plus dip-like structure.
032851.01+311818.5	SSV10, LkHa 352a	Fig. 31	Large ampl variable. CY var. 'Step' up in light curve. Varies like reddening vector at start, then becomes brighter, from which it moves fairly steadily bluer when brighter, with smaller variations on top consistent with reddening variations.
032851.24+311739.3	ASR41, LAL111	Fig. 24	Known edge-on disk (EOD). Significant bluer-when-brighter trend in [3.6] vs. [3.6]−[4.5].
032854.62+311651.2	SSV18b	Fig. 32	Possible significant redder-when-brighter trend in [4.5] vs. [3.6]−[4.5]. CY var. Long-term trend.
032855.53+311436.3	IRAS 2A, SK8, J07-15	Fig. 33	Jet driver/class 0. Very little [3.6]; light curve is almost all [4.5]. CY var. Long-term trend.
032856.63+311835.6	SSV11	Fig. 34	Burster light curve. Long-term trend.
032856.95+311622.3	SSV15	Fig. 35	Periodic source though not called out in text. Significant redder-when-brighter trend in [4.5] vs. [3.6]−[4.5]. CY var.
032857.37+311415.7	IRAS 2b, J07-16	Fig. 36	Jet driver/class 0. All [4.5]. CY var. Long-term trends.
032859.32+311548.5	SSV16, SVS16, SVS16ew	Fig. 37	Significant redder-when-brighter trend in [4.5] vs. [3.6]−[4.5]. Long-term trend.
032901.53+312020.6	SSV12, IRAS6	Fig. 38	All [3.6]. Long-term trend.
032905.75+311639.7	SSV14, ASR7	Fig. 39	Significant redder-when-brighter trend in [4.5] vs. [3.6]−[4.5]. Long-term trend.
032911.24+311831.8	IRAS7, Sadavoy2014-West14, J07-24	Fig. 29	Jet driver/class 0. CY var.
032917.66+312245.1	SVS2	Fig. 40	Periodic source though not called out in text.
032920.42+311834.3	SSV5, HH17	Fig. 41	Possible significant bluer-when-brighter trend in both CMDs. CY var. Long-term trend.
032921.87+311536.2	SSV20, LkHalpha271	Fig. 42	Periodic source though not called out in text. All [4.5]. CY var.
032903.75+311603.9	SVS13	Fig. 43	Data very close to saturation in [3.6] and saturated in [4.5]; the photometry shown here is extracted separately from the pipeline, assuming it is not quite saturated, and thus is not included in the rest of the analysis.
Objects not detected as variables over the YSOVAR campaign			
032912.91+311845.5	HH6, IRAS7	· · ·	CY var (see §4.3).
032910.37+312159.1	SVS3, IRAS8, X15	· · ·	
032854.06+311654.3	SSV18a	· · ·	
032846.18+311638.5	SSV21, LkHalpha351	· · ·	[3.6] only.
032857.20+311419.1	SSV19, BD+30547	· · ·	[4.5] only.
032909.64+312256.4	SVS7	· · ·	
032910.96+311825.6	ASR 32?/33?, IRAS7 SM1/2, SK20/21, VLA2	· · ·	Very few [3.6] points, mostly [4.5]. CY var.
032901.91+311541.4	MMS3, Sadavoy2014-West19?, SVS13c	· · ·	Very few points, and only [4.5].
032912.05+311301.4	IRAS4B, SK3, Sadavoy2014-West13, J07-25	· · ·	Jet driver/class 0. [4.5] only.
032913.60+311358.0	IRAS 4C, SK5, VLA29, Sadavoy2014-West30, J07-26	· · ·	[4.5] only. CY var.
032900.50+311200.7	IRAS 4B1, SK1, Sadavoy2014-West33, J07-18	· · ·	[4.5] only. CY var.
032904.07+311446.5	IRAS5, Sadavoy2014-West40, SK14, J07-21	· · ·	[4.5] only.
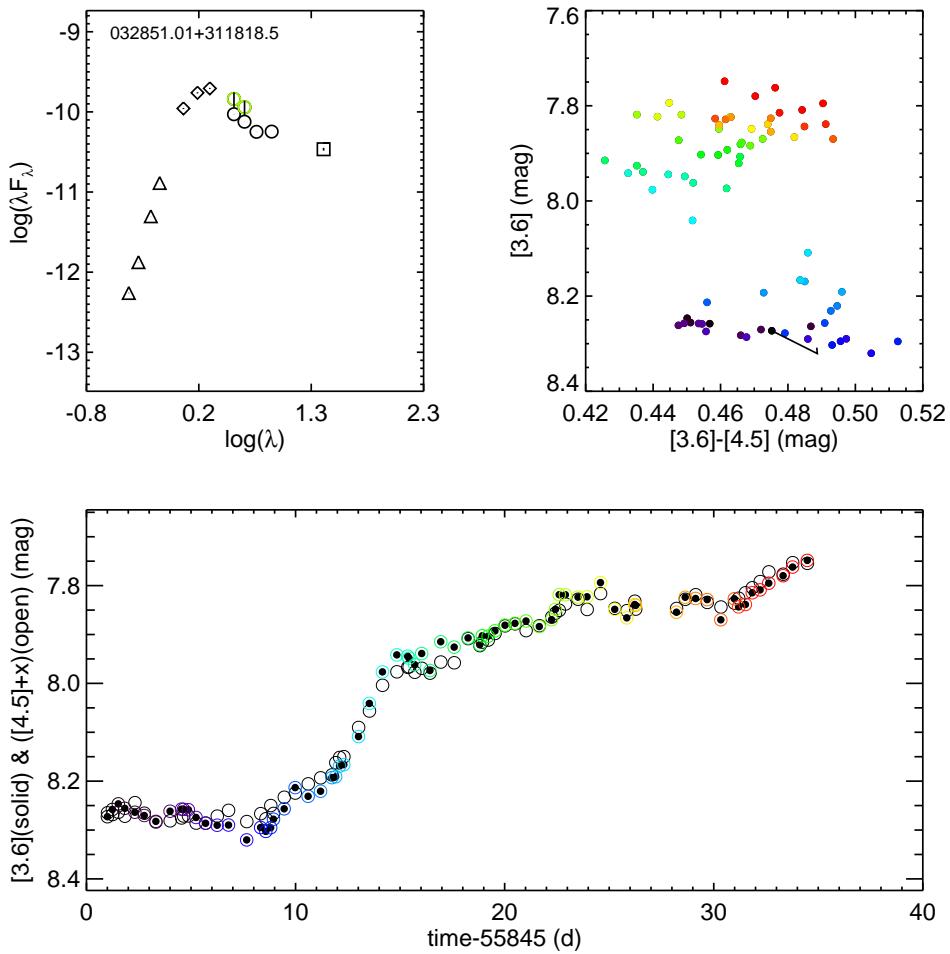
Fig. 31.— Light curve for famous YSO SSTYSV J032851.01+311818.5 (SSV10, LkHa 352a); see Table 7.
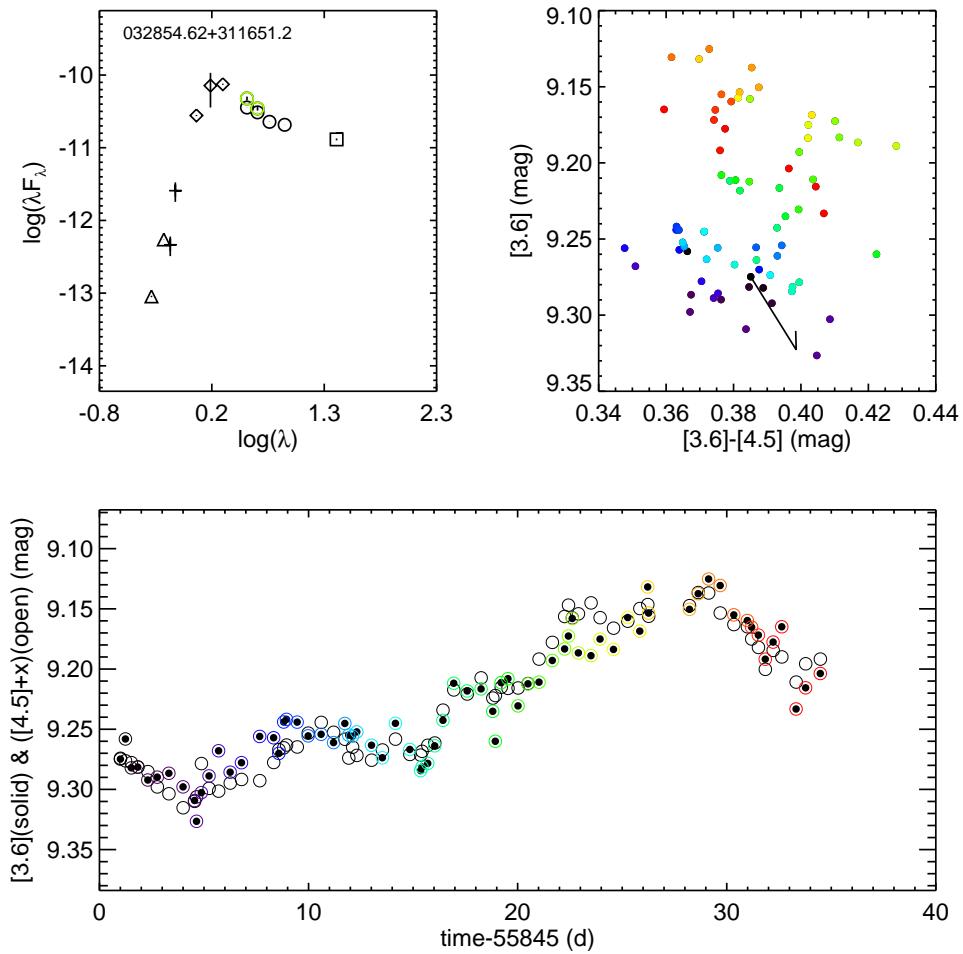
Fig. 32.— Light curve for famous YSO SSTYSV J032854.62+311651.2 (SSV18b); see Table 7.
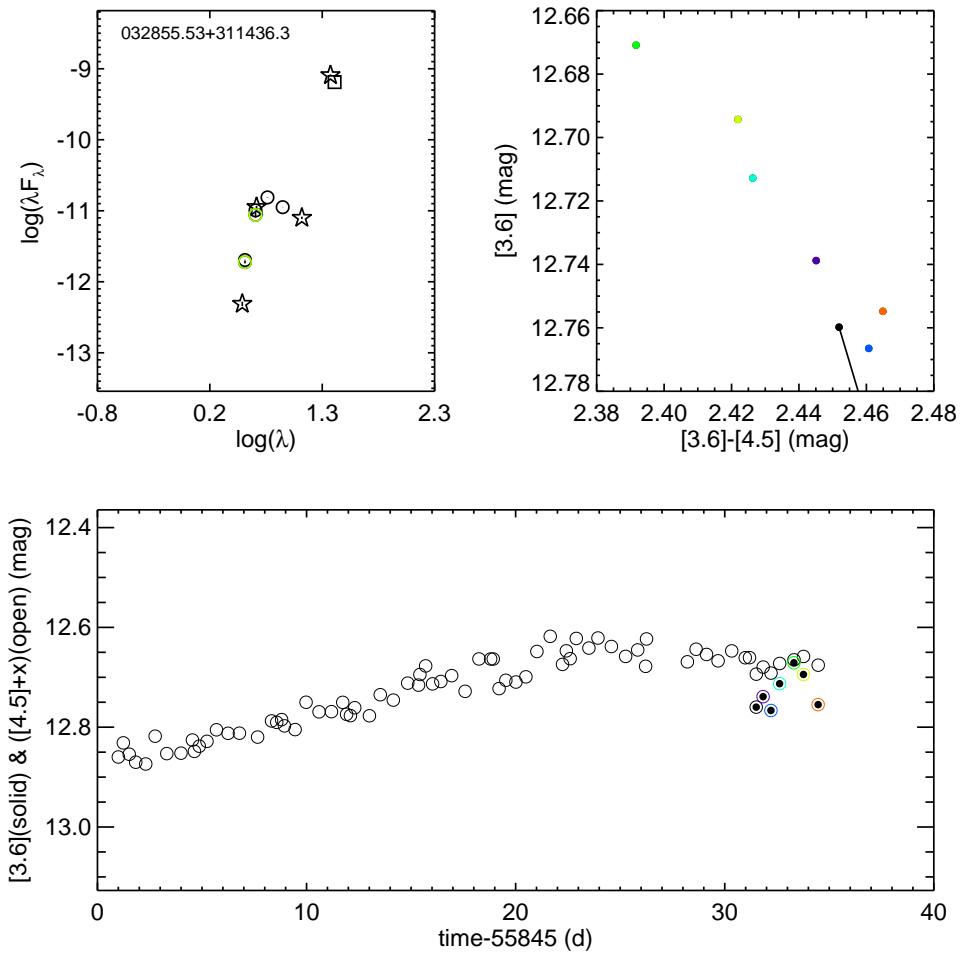
032855.53+311436.3

Fig. 33.— Light curve for famous YSO SSTYSV J032855.53+311436.3 (IRAS 2A, SK8, J07-15); see Table 7.
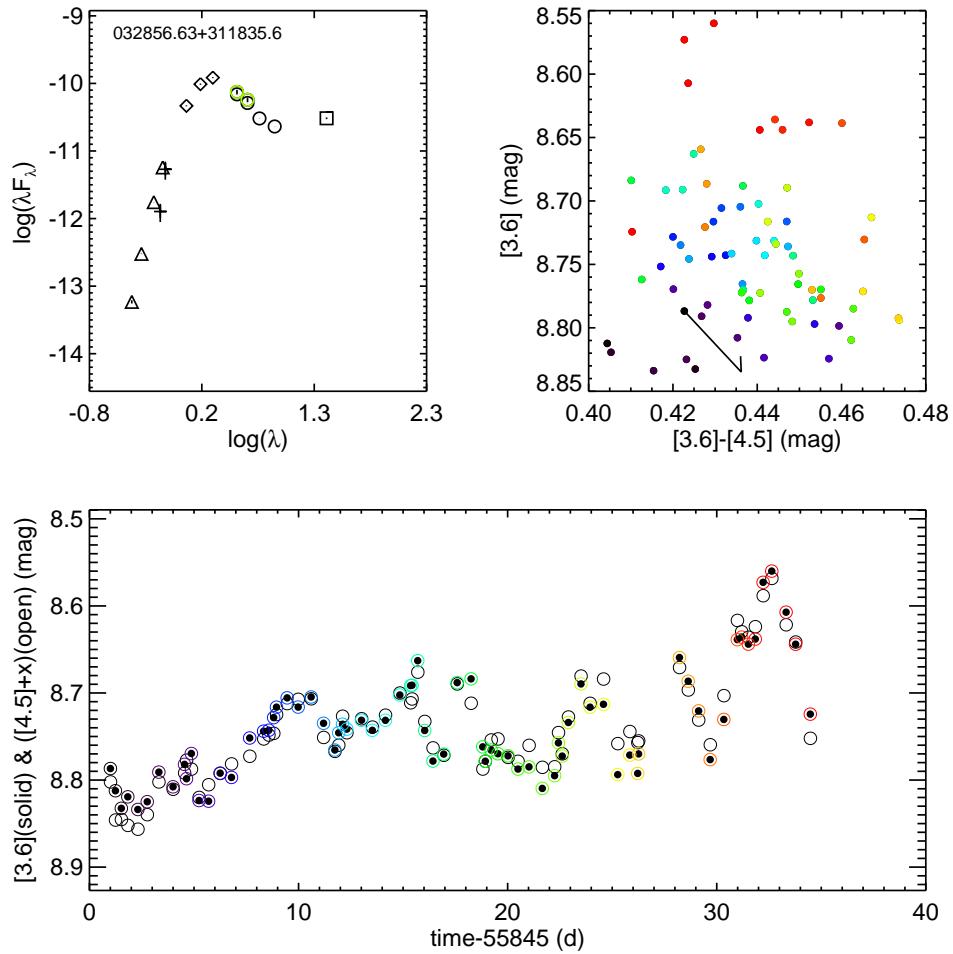
Fig. 34.— Light curve for famous YSO SSTYSV J032856.63+311835.6 (SSV11); see Table 7.
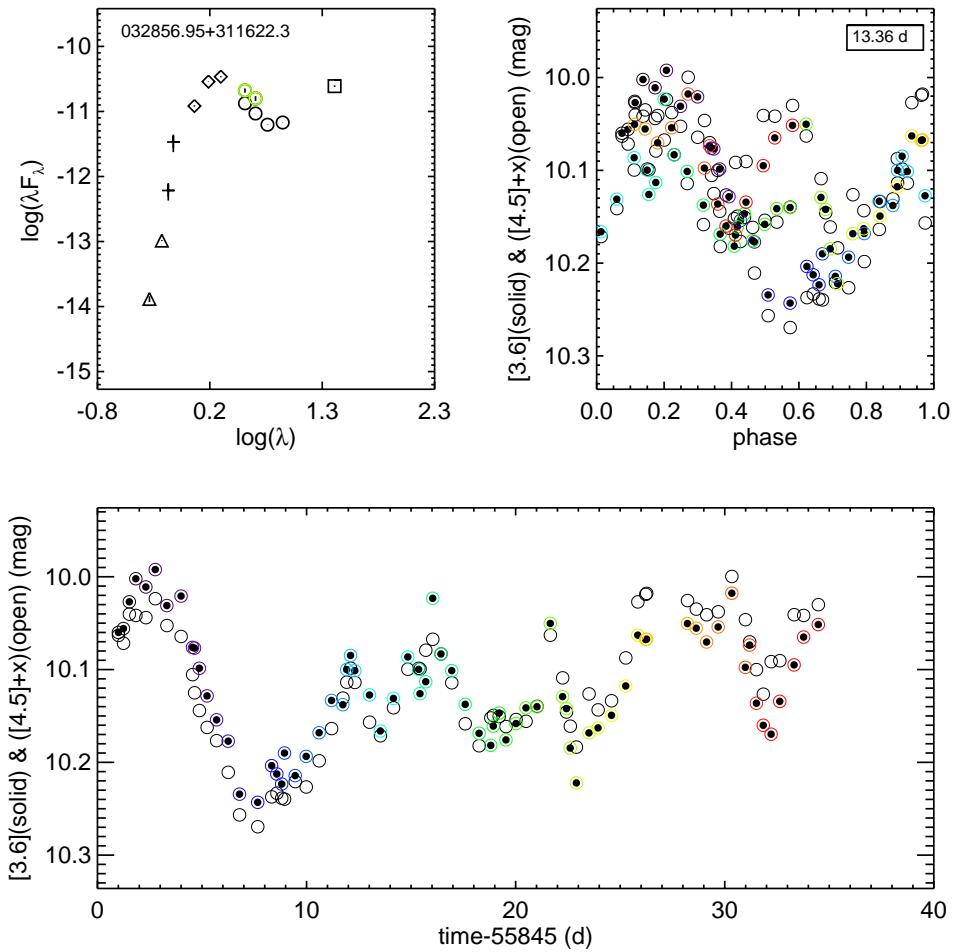
Fig. 35.— Light curve for famous YSO SSTYSV J032856.95+311622.3 (SSV15); see Table 7.
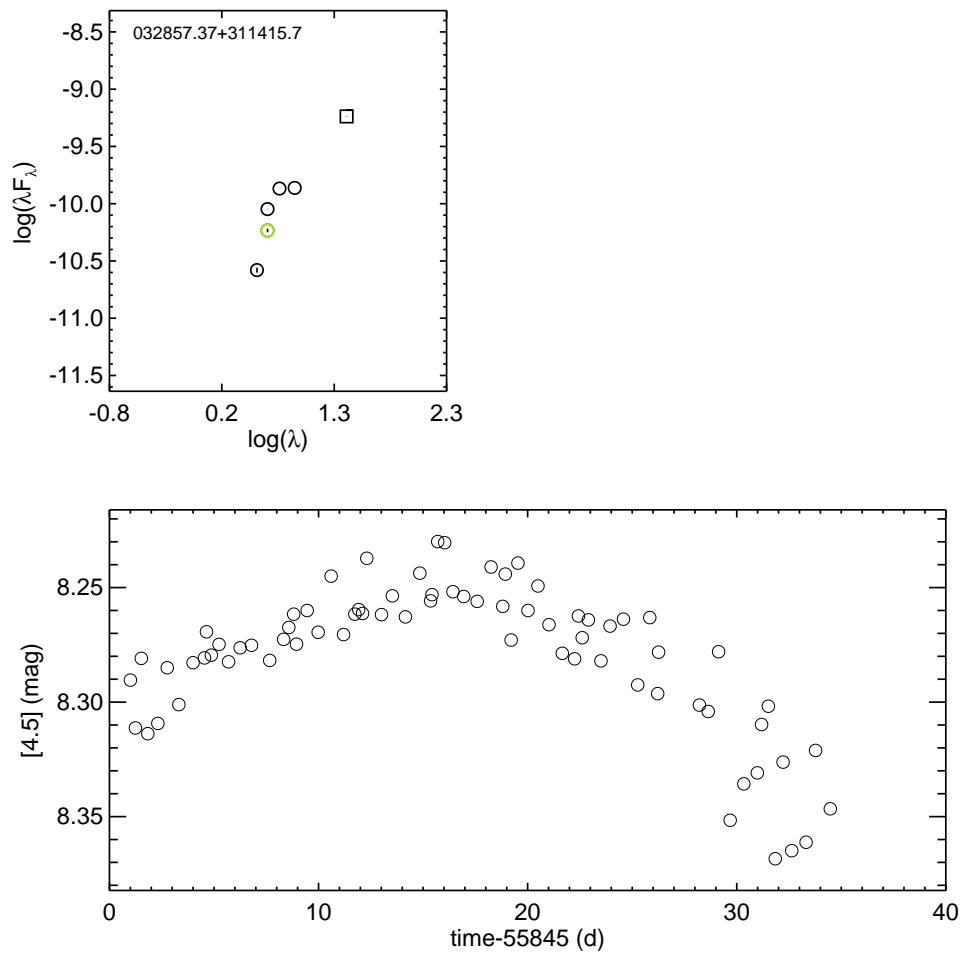
Fig. 36.— Light curve for famous YSO SSTYSV J032857.37+311415.7 (IRAS 2b, J07-16); see Table 7.
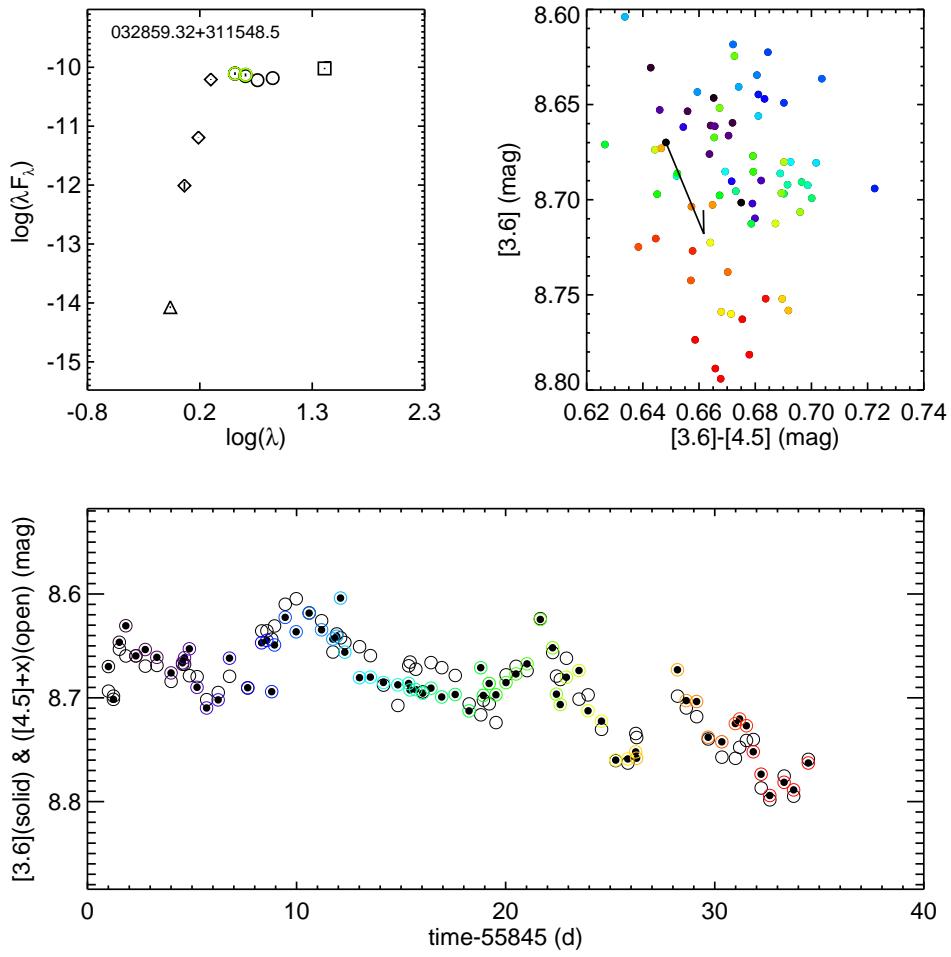
032859.32+311548.5

Fig. 37.— Light curve for famous YSO SSTYSV J032859.32+311548.5 (SSV16, SVS16, SVS16ew); see Table 7.
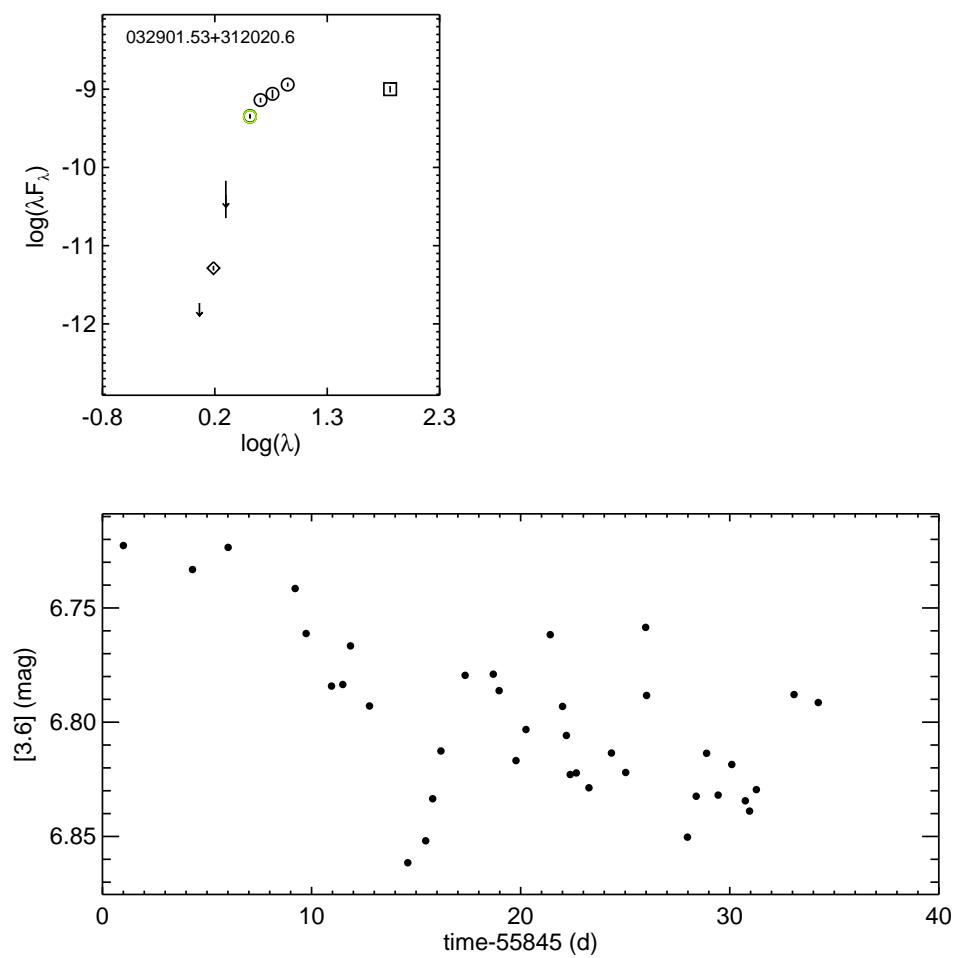
Fig. 38.— Light curve for famous YSO SSTYSV J032901.53+312020.6 (SSV12, IRAS6); see Table 7.
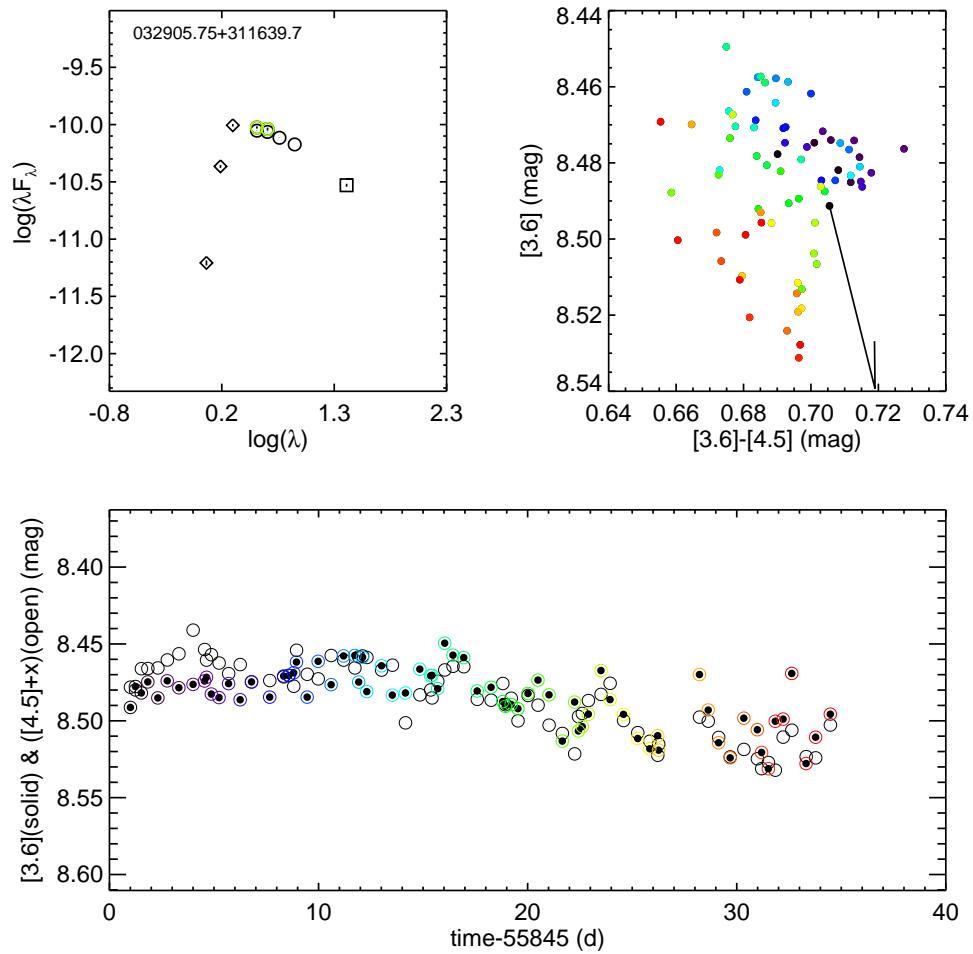
Fig. 39.— Light curve for famous YSO SSTYSV J032905.75+311639.7 (SSV14, ASR7); see Table 7.
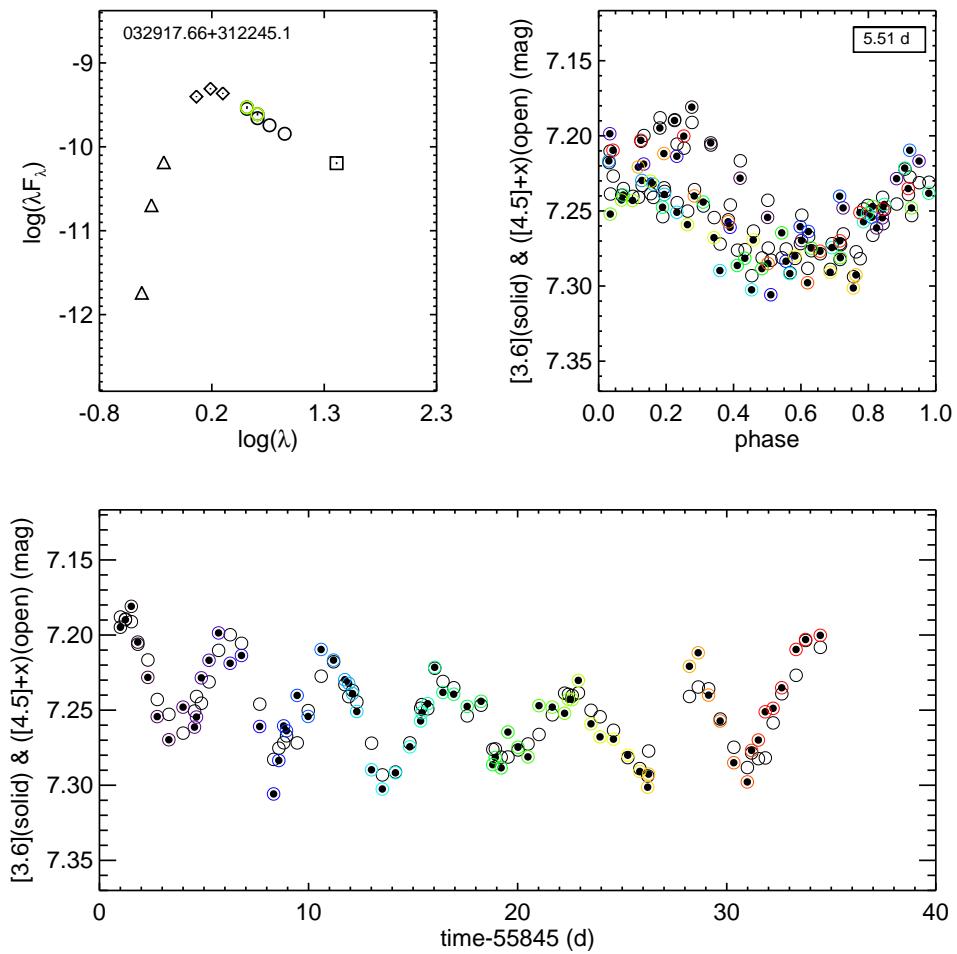
Fig. 40.— Light curve for famous YSO SSTYSV J032917.66+312245.1 (SVS2); see Table 7.
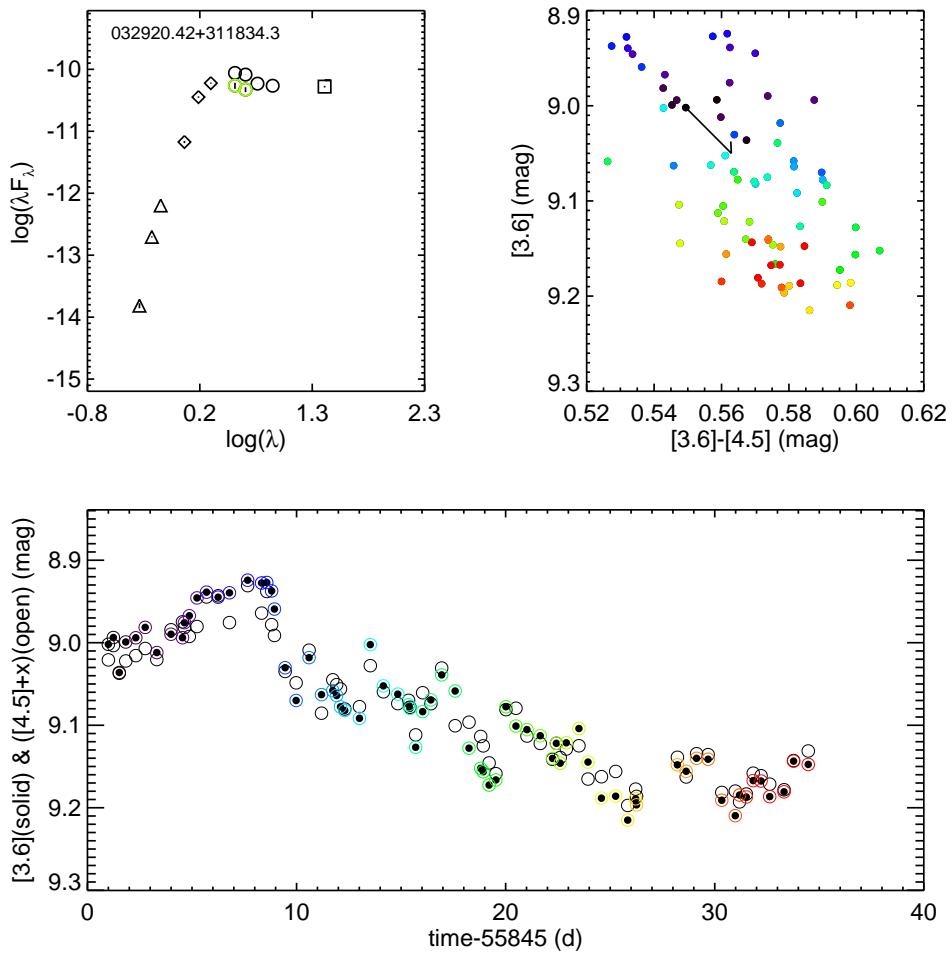
Fig. 41.— Light curve for famous YSO SSTYSV J032920.42+311834.3 (SSV5, HH17); see Table 7.
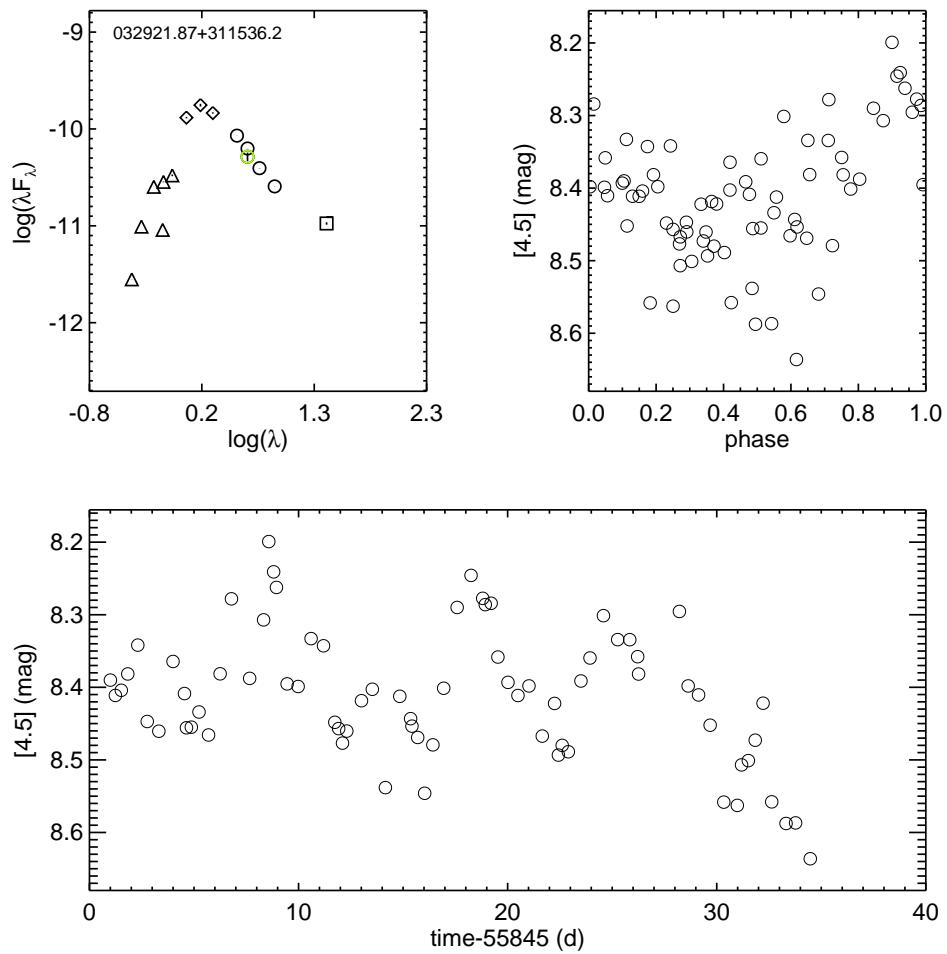
Fig. 42.— Light curve for famous YSO SSTYSV J032921.87+311536.2 (SSV20, LkHalpha271); see Table 7.
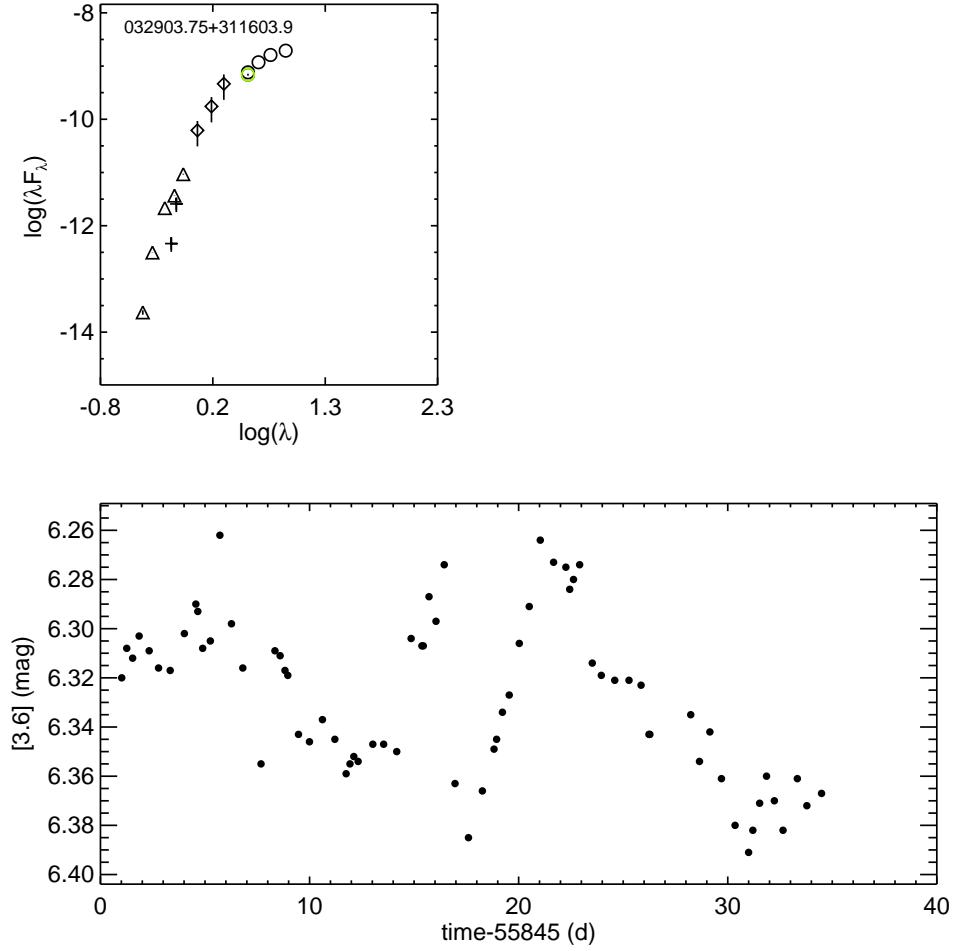
Fig. 43.— Light curve for famous YSO SSTYSV J032903.75+311603.9, or SVS 13; see Table 7. This light curve is extracted separately from the pipeline, assuming that the [3.6] data are not saturated, and thus is not included in the rest of the analysis.